

DOCUMENTATION PAGE		READ INSTRUCTIONS BEFORE COMPLETING FORM
1. REPORT NUMBER AFIT/CI/NR 88-193	2. GOVT ACCESSION NO.	3. RECIPIENT'S CATALOG NUMBER
4. TITLE (and Subtitle) A UTD <b>DTIC FILE COPY</b> JOURNALISTS OF PYRAMIDAL ABSORBER FOR DESIGN OF COMPACT RANGE CHAMBERS	5. TYPE OF REPORT & PERIOD COVERED MS THESIS	
	6. PERFORMING ORG. REPORT NUMBER	
7. AUTHOR(s) PHILIP J. JOSEPH	8. CONTRACT OR GRANT NUMBER(s)	
9. PERFORMING ORGANIZATION NAME AND ADDRESS AFIT STUDENT AT: OHIO STATE UNIVERSITY	10. PROGRAM ELEMENT, PROJECT, TASK AREA & WORK UNIT NUMBERS	
11. CONTROLLING OFFICE NAME AND ADDRESS	12. REPORT DATE 1988	13. NUMBER OF PAGES 149
	14. MONITORING AGENCY NAME & ADDRESS (if different from Controlling Office) AFIT/NR Wright-Patterson AFB OH 45433-6583	
15. SECURITY CLASS. (of this report) UNCLASSIFIED		15a. DECLASSIFICATION/DOWNGRADING SCHEDULE
16. DISTRIBUTION STATEMENT (of this Report) DISTRIBUTED UNLIMITED: APPROVED FOR PUBLIC RELEASE		
17. DISTRIBUTION STATEMENT (of the abstract entered in Block 20, if different from Report) SAME AS REPORT		
18. SUPPLEMENTARY NOTES	Approved for Public Release: IAW AFR 190-1 LYNN E. WOLAVER <i>Lynn Wolaver</i> 29 AUG 88 Dean for Research and Professional Development Air Force Institute of Technology Wright-Patterson AFB OH 45433-6583	
19. KEY WORDS (Continue on reverse side if necessary and identify by block number)		
20. ABSTRACT (Continue on reverse side if necessary and identify by block number) ATTACHED		

**DTIC**  
**ELECTE**  
SEP 09 1988  
**S** **D**  
**E**



**A UTD SCATTERING ANALYSIS OF PYRAMIDAL ABSORBER FOR  
DESIGN OF COMPACT RANGE CHAMBERS**

By

Philip J. Joseph, B.S.E.E., M.S.E.E.

Captain, USAF

Degree Awarded: Ph.D.

The Ohio State University, 1988

Dissertation Length: 149 pages

Accession For	
NTIS GRA&I	<input checked="" type="checkbox"/>
DTIC TAB	<input type="checkbox"/>
Unannounced	<input type="checkbox"/>
Justification	
By _____	
Distribution/	
Availability Codes	
Dist	Avail and/or Special
A-1	

**Abstract**

→ The compact range allows for the measurement of radar cross section and antenna patterns in a relatively small room. An offset-feed parabolic reflector is normally used to approximate a plane wave in the target zone; however, some of the energy transmitted by the feed will strike the ceiling, walls, and floor of the room. These stray signals then scatter in all directions. To reduce the level of scattered energy, the room is typically lined with pyramidal-shaped radar absorbing material. However, the behavior of this material is not well understood.

A diffraction formulation, based on the Uniform Geometrical Theory of Diffraction [1,2], is developed for a lossy dielectric corner. Using this formulation, a computer code is written that calculates the bistatic scattering from a pyramidal absorber tip. Sample results display some features of scattering from a single pyramid. Calculations are then compared with backscatter measurements of a single pyramid, and with bistatic measurements [3] of an absorber wall. Next, a

general purpose computer code is written which calculates the scattering into the target zone of a compact range from the pyramidal absorber which lines the room. (A focus-fed semi-circular parabolic reflector with rolled edge and a skirt [4] illuminates the room.) Sample calculations show the total power scattered into the target zone, and how strongly various locations in the room contribute to this total scattered power. Finally, calculations are compared with experimental data [5] in which a 6' x 6' aluminum plate (Theses; jhd) (mounted in the Ohio State University compact range target zone) was used to measure bistatic scattering from the pyramidal absorber on the ceiling.

## Bibliography

- [1] R.G. Kouyoumjian and P.H. Pathak, "A Uniform Geometrical Theory of Diffraction for an Edge in a Perfectly-Conducting Surface," *Proc. IEEE*, vol. 62, November 1974, pp. 1448-1461.
- [2] W.D. Burnside, N. Wang and E.L. Pelton, "Near-Field Pattern Analysis of Airborne Antennas," *IEEE Trans. on Antennas and Propagation*, vol. AP-28, No.3, pp. 318-327, 1980.
- [3] B.T. DeWitt, "Analysis and Measurement of Electromagnetic Scattering by Pyramidal and Wedge Absorbers," Dissertation, The Ohio State University Electroscience Lab., Department of Electrical Engineering, 1986.
- [4] I.J. Gupta and W.D. Burnside, "User Manual for Semi-Circular Compact Range Reflector Code - Version II," Technical Report 716148-18, January 1987, The Ohio State University Electroscience Lab., Department of Electrical Engineering, prepared under Grant No. NSG-1613 for NASA.
- [5] G. Clerici and J. D. Young, "Analysis of Anechoic Room Scattering for Compact Range Performance Prediction," Tech. Report 719267-11, The Ohio State University Electroscience Laboratory, January 1988.

**A UTD SCATTERING ANALYSIS OF PYRAMIDAL  
ABSORBER FOR DESIGN OF COMPACT RANGE CHAMBERS**

**A Dissertation**

**Presented in Partial Fulfillment of the Requirements for  
the Degree Doctor of Philosophy in the  
Graduate School of the Ohio State University**

**by**

**Philip J. Joseph, B.S.E.E., M.S.E.E.**

**\* \* \* \* \***

**The Ohio State University**

**1988**

**Dissertation Committee:**

**Professor Walter D. Burnside**

**Professor Leon Peters, Jr.**

**Professor Roger C. Rudduck**

**Approved by:**

*Walter D. Burnside*

**Advisor  
Department of Electrical  
Engineering**

## DEDICATION

To my wife Joye; my children Jessica, Melanie, and Michael;  
and my parents Jessie and Lucia.

## ACKNOWLEDGEMENTS

I would like to thank my advisor, Prof. W. D. Burnside, for his guidance throughout this research effort. I would also like to thank the members of my reading committee, Prof. L. Peters, Jr. and Prof. R. C. Rudduck, for their suggestions and comments.

I am indebted to many others for their support. In particular, I express my thanks to Dr. R. J. Marheska for his insights in corner diffraction, to Dr. I. J. Gupta for assistance in using his reflector analysis code, to Mr. N. F. Chamberlain for his suggestions in signal processing, and to Mr. B. J. E. Taute for his help in graphics programming. I also thank Dr. G. Clerici for our many technical discussions, and Mr. J. R. Jameson for aid in computer programming.

To my wife and children, I express my heartfelt thanks for your patience, love, and understanding. And to my parents, I thank you for conveying to me the importance of an education.

I express my appreciation to the United States Air Force for providing me the opportunity to pursue this degree.

## VITA

- August 23, 1959 ..... Born in Woonsocket, Rhode Island
- May 1981 ..... B.S.E.E. (Summa cum Laude),  
The University of Lowell,  
Lowell, Massachusetts
- May 1981 - Present ..... USAF Officer
- Dec 1982 ..... M.S.E.E. (Distinguished Graduate),  
The Air Force Institute of Technology,  
Wright-Patterson AFB, Ohio
- Jan 1983 - May 1985 ..... Electromagnetic Research Engineer,  
Rome Air Development Center,  
Hanscom AFB, Massachusetts
- Jun 1985 - present ..... Special assignment at  
the Ohio State University,  
Electroscience Laboratory

## Publications

- "An Evaluation of Chemical Storage Batteries as the Primary Power Supply for an Electromagnetic Launcher," Master's Thesis, The Air Force Institute of Technology, 1982.
- "An Evaluation of Battery Power Supplies for Electric Railguns," presented at the 4<sup>th</sup> IEEE Pulsed Power Conference, Albuquerque NM, June 1983.
- "Airborne Measurements of Low Frequency TE/TM Signal Strength obtained during the Miniature Receive Terminal Flight Tests," Tech. Report RADC-TR-85-113, Rome Air Development Center, AFSC, Griffiss AFB NY, June 1985.
- "A Pyramidal Absorber Scattering Analysis for Design of Compact Range Chambers," co-author W. D. Burnside, submitted for publication to the IEEE Trans. on Antennas and Propagation, July 1988.

## Fields of Study

Major Field: Electromagnetics ..... Advisor: Prof. W. D. Burnside

Communication Theory ..... Prof. R. T. Compton

Mathematics ..... Prof. J. T. Scheick

Statistics ..... Prof. J. S. Rustagi

## TABLE OF CONTENTS

<b>DEDICATION</b>	<b>ii</b>
<b>ACKNOWLEDGEMENTS</b>	<b>iii</b>
<b>VITA</b>	<b>iv</b>
<b>LIST OF FIGURES</b>	<b>ix</b>
<b>CHAPTER</b>	<b>PAGE</b>
<b>I. INTRODUCTION</b>	<b>1</b>
1.1 Statement of the Problem . . . . .	1
1.2 Motivation . . . . .	2
1.3 Approach . . . . .	3
<b>II. DIFFRACTION FROM PERFECT CONDUCTORS</b>	<b>6</b>
2.1 Introduction . . . . .	6
2.2 Two-Dimensional Wedge Diffraction . . . . .	6
2.3 Three-Dimensional Wedge Diffraction . . . . .	11
2.4 Corner Diffraction . . . . .	17
<b>III. DIFFRACTION FROM DIELECTRIC WEDGES AND COR- NERS</b>	<b>27</b>
3.1 Introduction . . . . .	27

3.2	Reflection and Transmission at a Dielectric Interface . . . . .	27
3.3	Two-Dimensional Dielectric Slab . . . . .	30
3.4	Two-Dimensional Dielectric Wedge . . . . .	36
3.5	Three-Dimensional Dielectric Wedge . . . . .	42
3.6	Dielectric Corner Diffraction . . . . .	49
<b>IV.</b>	<b>TIP DIFFRACTION FROM PYRAMIDAL ABSORBER</b>	<b>51</b>
4.1	Introduction . . . . .	51
4.2	Tip Diffraction Calculations . . . . .	51
4.3	Sample Calculations . . . . .	66
<b>V.</b>	<b>PYRAMIDAL ABSORBER SCATTERING IN A COMPACT RANGE</b>	<b>75</b>
5.1	Introduction . . . . .	75
5.2	Method of Calculation . . . . .	75
5.3	Sample Calculations . . . . .	88
<b>VI.</b>	<b>EXPERIMENTAL VERIFICATION OF PYRAMIDAL ABSORBER SCATTERING CALCULATIONS</b>	<b>102</b>
6.1	Introduction . . . . .	102
6.2	Backscatter from a Single Absorber Pyramid . . . . .	102
6.3	Comments on Addition of Pyramidal Fields and Effective RCS	108
6.4	Bistatic Scattering from a Wall of Pyramidal Absorber . . . . .	113
6.5	Ceiling Absorber Scattering in a Compact Range Chamber . . . . .	116
<b>VII.</b>	<b>SUMMARY AND CONCLUSIONS</b>	<b>124</b>

**APPENDIX**

<b>A. PROGRAM CHAMBER</b>	<b>127</b>
A.1 Introduction . . . . .	127
A.2 Software Requirements . . . . .	127
A.3 Operation of CHAMBER . . . . .	130
A.4 Error Messages . . . . .	143
<b>REFERENCES</b>	<b>148</b>

## LIST OF FIGURES

FIGURE		PAGE
1	UTD ray paths of a line source radiating in the presence of a wedge.	7
2	Transition function. . . . .	10
3	Ray-fixed coordinate system for 3D reflection. . . . .	12
4	Geometry for diffraction from 3D wedge. . . . .	14
5	Ray-fixed coordinate system for 3D diffraction. . . . .	15
6	Corner diffraction geometry. . . . .	18
7	Geometry for scattering from a square flat plate. . . . .	22
8	Flat plate scattering, $\phi^s = 0.1^\circ$ , from [11]. . . . .	24
9	Flat plate scattering (cross-polarized fields), $\phi^s = 122^\circ$ , from [11].	25
10	Flat plate scattering (co-polarized fields), $\phi^s = 122^\circ$ , from [11]. . .	26
11	Reflection and transmission at a dielectric interface, perpendicular polarization. . . . .	28
12	Reflection and transmission at a dielectric interface, parallel polarization. . . . .	29
13	Plot of $ R_\perp $ vs. $\theta^i$ for various $\epsilon_2$ . . . . .	31
14	Plot of $ R_\parallel $ vs. $\theta^i$ for various $\epsilon_2$ . . . . .	31
15	Geometry for diffraction from a 2D semi-infinite dielectric slab. . .	32
16	Multiple interactions within dielectric slab. . . . .	34

17	Finite 2D dielectric slab with line source illumination. . . . .	36
18	Bistatic scattering from a right angle dielectric wedge, modified UTD vs Rawlins' solution ( $\theta_o = 45^\circ$ ). . . . .	39
19	Bistatic scattering from a right angle dielectric wedge, modified UTD vs Rawlins' solution ( $\theta_o = 30^\circ$ ). . . . .	40
20	Bistatic scattering from a right angle dielectric wedge, modified UTD vs Rawlins' solution ( $\theta_o = 15^\circ$ ). . . . .	41
21	Reflection and diffraction at a three-dimensional dielectric wedge. .	44
22	Pertinent field polarizations for reflection near wedge edge. . . . .	45
23	Conventions used for pyramid geometry. . . . .	52
24	Determination of the pyramidal wedge angle, WA. . . . .	53
25	Edge-fixed coordinate system for pyramid edge 1. . . . .	55
26	Tip diffraction geometry. . . . .	58
27	Geometry for incident and scattered fields of a pyramid tip. . . . .	59
28	Determination of $\phi$ and $\phi'$ at an arbitrary edge. . . . .	60
29	Determination of $\beta'_o$ at an arbitrary edge. . . . .	62
30	Backscatter in the $\phi = 0^\circ$ and $45^\circ$ planes from the tip of an absorber pyramid. . . . .	67
31	Backscatter from a pyramidal absorber tip in the $\phi = 0^\circ$ plane, for two values of $\alpha$ . . . . .	70
32	Backscatter from a pyramidal absorber tip in the $\phi = 0^\circ$ plane, for two values of $\epsilon_r$ . . . . .	71
33	Bistatic scattering in the $xz$ plane from the tip of an absorber pyramid.	73
34	Bistatic scattering along the $\theta^s = 45^\circ$ cone from the tip of an ab- sorber pyramid. . . . .	74

35	Typical absorber scattering paths calculated by CHAMBER. . . . .	76
36	Anechoic room considered in absorber scatter calculations. . . . .	77
37	Imaginary grid along ceiling patch. . . . .	80
38	Typical "pyramidal coordinate systems" used by the Absorber Code. . . . .	82
39	Equivalent absorber scattering paths used by CHAMBER for the ( $y' < 0$ ) side of the room. . . . .	86
40	Timing considerations in CHAMBER. . . . .	88
41	Absorber scattered power vs. frequency. Test point at ( $x', y', z'$ ) = (6, 0, 24) ft. . . . .	90
42	Absorber scattered power vs. test point $x'$ coordinate. Frequency = 10 GHz. ( $y' = 0, z' = 24$ ft). . . . .	92
43	Absorber scattered power vs. test point $y'$ coordinate. Frequency = 10 GHz. ( $x' = 6$ ft, $z' = 24$ ft). . . . .	93
44	Absorber scattered power vs. test point $z'$ coordinate. Frequency = 10 GHz. ( $x' = 6$ ft, $y' = 0$ ). . . . .	94
45	Ceiling illumination vs. ceiling $y', z'$ coordinates. (dB rel. to inci- dent plane wave). . . . .	96
46	Wall illumination vs. wall $x', z'$ coordinates. (dB rel. to incident plane wave). . . . .	96
47	Floor illumination vs. floor $y', z'$ coordinates. (dB rel. to incident plane wave). . . . .	97
48	Ceiling scatter vs. ceiling $y', z'$ coordinates. Test point at (6,0,24). (dB rel. to incident plane wave). . . . .	98
49	Floor scatter vs. floor $y', z'$ coordinates. Test point at (6,0,24). (dB rel. to incident plane wave). . . . .	98

50	Ceiling scatter vs. ceiling $y'$ , $z'$ coordinates ( $y' > 0$ ). Test point at (6,5,24). (dB rel. to incident plane wave). . . . .	100
51	Ceiling scatter vs. ceiling $y'$ , $z'$ coordinates ( $y' < 0$ ). Test point at (6,5,24). (dB rel. to incident plane wave). . . . .	100
52	Floor scatter vs. floor $y'$ , $z'$ coordinates ( $y' > 0$ ). Test point at (6,5,24). (dB rel. to incident plane wave). . . . .	101
53	Floor scatter vs. floor $y'$ , $z'$ coordinates ( $y' < 0$ ). Test point at (6,5,24). (dB rel. to incident plane wave). . . . .	101
54	Absorber sample used for single pyramid backscatter measurements.	103
55	Bandlimited impulse response of single pyramid; $\phi = 0^\circ$ , $\theta = 0^\circ$ . . . . .	104
56	Bandlimited impulse response of single pyramid; $\phi = 0^\circ$ , $\theta = 45^\circ$ . . . . .	105
57	Energy temporal density of single pyramid; $\phi = 0^\circ$ , $\theta = 0^\circ$ . . . . .	106
58	Energy temporal density of single pyramid; $\phi = 0^\circ$ , $\theta = 45^\circ$ . . . . .	107
59	Calculated vs. measured backscatter from a single pyramid; $\phi = 0^\circ$ , $\theta = 0^\circ$ . . . . .	108
60	Calculated vs. measured backscatter from a single pyramid; $\phi = 0^\circ$ , $\theta = 45^\circ$ . . . . .	109
61	Magnitude ( $S_r$ ) of sum of fields from an absorber block vs. frequency [7]. . . . .	111
62	Experimental setup of bistatic absorber wall scatter measurement [7].	115
63	Bandlimited impulse response of wall scatter measurement [7]. . . . .	116
64	Comparison of frequency domain data versus calculations, wall scatter experiment (experimental data from [7]). . . . .	117
65	Experimental setup used for Plate measurements. . . . .	118

66	Bandlimited impulse response of Plate experiment, vertical polarization. . . . .	121
67	Bandlimited impulse response of Plate experiment, horizontal polarization. . . . .	122
68	Calculations vs. measurements of ceiling absorber scatter ( $\sigma_{ceil}$ ). .	123
69	Range reflector cross-section ( $y' = 0$ ), skirt not shown. . . . .	129
70	Views provided by gray-scale plots of Chapter V. . . . .	144

# CHAPTER I

## INTRODUCTION

### 1.1 Statement of the Problem

The measurement of radar cross section (RCS) or of an antenna pattern requires that the target or antenna being tested be illuminated by a uniform plane wave. This plane wave is approximated in a far-field test range simply by placing the test object in the far zone of the transmitter, where the spherical wavefront of the transmitted field can be considered approximately planar. Depending on the size of the test object and the wavelength being used, this far zone requirement typically leads to an outdoor facility. The compact range offers an alternative to the far-field test range for the measurement of RCS or antenna patterns. A compact range normally uses an offset-feed parabolic reflector to approximate a plane wave in a relatively small chamber. The small size of a compact range makes it practical as an indoor facility, thus free from adverse weather, interference, or external monitoring. Of course, not all of the energy transmitted by the feed will be directed into the desired plane wave. Rather, some will strike the ceiling, walls, and floor of the room. These stray signals then scatter in all directions. They degrade the nature of the incident plane wave in the target region, and they also return directly to the receiver, corrupting the desired return from the target. Thus, they affect the accuracy of the range and the size of its "sweet spot" (the region where the illumination satisfactorily approximates a plane wave). One method to

eliminate these stray signals might be to make the room large enough so that they could all be time-gated out; however, this would be prohibitively expensive. In a room of practical size, some of these unwanted signals can be time-gated out, others cannot. To reduce the level of scattered energy, the room is typically lined with pyramidal-shaped radar absorbing material. However, the behavior of this pyramidal absorber is not well understood, especially for compact range applications.

In this study, a scattering formulation based on the uniform geometrical theory of diffraction (UTD) is developed to describe the fields diffracted by a pyramidal absorber tip. This is then used to generate a computer code for the calculation of bistatic scattering from the tip of an absorber pyramid. With this code, and a reflector analysis code that computes the fields incident on the pyramidal absorber in the chamber, a general purpose computer code is developed which calculates the energy scattered by the pyramidal absorber to the target region of the compact range chamber. Finally, various scattering measurements are made to verify the calculated results. These range from the backscatter of a single pyramid to the absorber scatter directed into the compact range target zone from the ceiling.

## 1.2 Motivation

Pyramidal absorber material has been widely used for many years to reduce the clutter level in anechoic chambers. However, as stated above, the behavior of pyramidal absorber material is not well understood. The actual levels of stray signals scattered from the absorber in a compact range chamber have not previously been calculated. Such information would prove useful in the design of a compact range chamber, and thus motivates this research effort.

### 1.3 Approach

The first goal in this study is the development of a scattering formulation for a (lossy) dielectric pyramidal tip. The pyramidal tip is analyzed as a corner in a three-dimensional wedge, which has four planar faces and four edges intersecting at a common point. Thus, a dielectric corner diffraction formulation is needed.

In Chapter II, the expressions for diffraction from perfect conductors are reviewed. These include two and three-dimensional wedge diffraction [1,2,3,4], along with corner diffraction [5]. An understanding of these is necessary for one to extend the perfectly-conducting corner diffraction solution to the case of a dielectric corner.

Chapter III begins by investigating dielectric modifications that have been made to the UTD for simpler geometries. The first was developed by Burnside and Burgener [6], who studied the problem of edge diffraction from a two-dimensional dielectric slab. This was based on the effect of the dielectric on the discontinuities at the shadow boundaries, and accounted for the multiple interactions occurring within the dielectric slab. Next, DeWitt [7] considered a similar modification for the more general problem of a two-dimensional dielectric wedge. Owing to the added complexity of the wedge problem, the method of solution was found through a heuristic argument. However, comparisons with a Neumann series solution by Rawlins [8] show good agreement.

Chapter III then proceeds to further these efforts. Sections 3.5 and 3.6 extend the dielectric modification of [7] to the problems of three-dimensional dielectric wedge and corner diffraction, respectively. The most significant complication here involves the matter of field polarization inherent in the three-dimensional problem. An interesting result is that the dielectric material causes a cross-coupling in the

polarizations of the incident and diffracted fields.

Chapter IV applies the UTD dielectric corner diffraction solution to the problem of the absorber pyramid. The interpretation and calculation of the variables in the dielectric corner diffraction solution represents a significant task, and is thus described in detail. The resulting code, referred to as the Absorber code, computes the bistatic scattering from a pyramidal absorber tip. Sample calculations for various monostatic and bistatic geometries are then presented.

Chapter V considers the absorber scattering that takes place in a compact range chamber. The fields from the range reflector which illuminate the absorber are calculated through a modified version of the Semi-Circular Compact Range Reflector Code [9], while the fields subsequently scattered by the absorber to the target region are calculated by means of the Absorber code. (This is done in a general purpose computer code, program CHAMBER, which calls the reflector and absorber codes as subroutines. CHAMBER allows many parameters to be varied, and provides several output options.) The method of calculation is first described in some detail. Sample calculations of absorber scattering in a compact range are then presented.

Chapter VI provides experimental verification of absorber scatter calculations. First, the backscatter of a single pyramidal tip is measured, and is seen to compare well with calculations. The topic of addition of the scattered fields from several pyramids is then discussed, since this is relevant to the remaining experiments. Next, calculations are compared with measurements of bistatic scattering from a wall of pyramidal absorber. The results are very encouraging, since the calculations predict both the magnitude and the frequency behavior of the measured absorber scatter. Finally, an experiment is described in which the reflected fields from a large plate are directed toward the ceiling absorber (of the Ohio State University

compact range chamber) and are then bistatically scattered by the absorber to the reflector and received by the compact range. Again, calculations agree well with measurements.

Chapter VII presents a summary and conclusions. In appendix A, the operation of program CHAMBER is discussed.

## CHAPTER II

### DIFFRACTION FROM PERFECT CONDUCTORS

#### 2.1 Introduction

This chapter begins by describing the UTD solution for scattering from a perfectly-conducting two-dimensional wedge. Two ray-fixed coordinate systems are then introduced and used to put the UTD solution for a perfectly-conducting three-dimensional wedge into a compact form. Lastly, diffraction coefficients for a corner in a conducting flat plate and a three-dimensional wedge are presented.

#### 2.2 Two-Dimensional Wedge Diffraction

Consider an electric or magnetic line source illuminating an infinite, perfectly-conducting wedge formed by two plane surfaces, as shown in Figure 1. The total UTD solution for this problem consists of an incident, reflected, and diffracted field. The incident field is the source field in the absence of the wedge (although one must take into account the shadowing of the wedge). The reflected field is that field reflected from the surface of the wedge with the edge ignored. Region I contains incident, reflected, and diffracted rays; region II contains incident and diffracted rays; and region III contains only diffracted rays. The incident and reflected fields constitute the classical geometrical optics (GO) solution. Alone, this solution predicts zero fields in region III (the shadow region), and discontinuities exist at both the incident and reflected field shadow boundaries. It is the

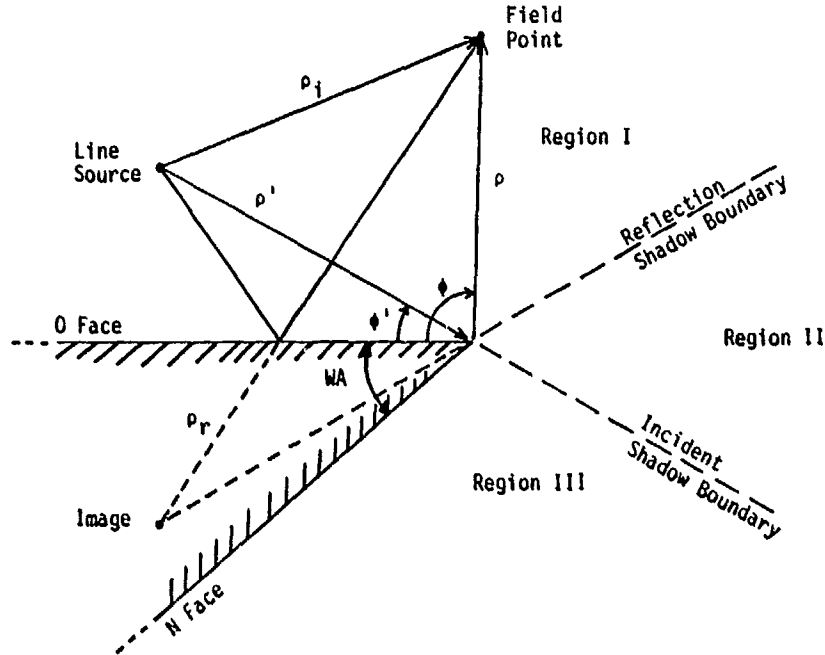


Figure 1: UTD ray paths of a line source radiating in the presence of a wedge.

diffracted field that exists in the shadow region, and it is the diffracted field that combines with the geometrical optics field to produce a total field which is continuous across both shadow boundaries. Keller [1,2,3] first introduced the diffracted field in his geometrical theory of diffraction (GTD), yielding a simple geometric interpretation of the fields associated with the currents excited at the edge of the wedge. However, one limitation of his solution was that it was singular at the shadow boundaries, where the diffracted field is most significant. Kouyoumjian and Pathak [4], using asymptotic methods and the exact eigenfunction solution for the wedge, developed a uniform geometrical theory of diffraction ansatz within the context of Keller's solution. Their solution eliminates Keller's singularity by introducing a multiplicative factor that approaches zero at the shadow boundaries.

The total UTD solution for the wedge is given by

$$u^{total} = u^{inc} + u^{ref} + u^{dif} \quad (2.1)$$

where  $u$  represents an electric (magnetic) scalar field for illumination by an electric (magnetic) line source. The line source is located at  $(\rho', \phi')$  with respect to the edge, while the receiver is located at  $(\rho, \phi)$ . The incident field is given by

$$u^{inc} = \begin{cases} K \frac{e^{-jk\rho_i}}{\sqrt{\rho_i}} & \text{in regions I and II, and} \\ 0 & \text{in region III} \end{cases} \quad (2.2)$$

where  $\rho_i$  is the distance from the source to the receiver,  $k$  is the wavenumber of the medium surrounding the wedge, and  $K$  is a complex constant. The reflected field is given by

$$u^{ref} = \begin{cases} \pm K \frac{e^{-jk\rho_r}}{\sqrt{\rho_r}} & \text{in region I, and} \\ 0 & \text{in regions II and III} \end{cases} \quad (2.3)$$

where  $\rho_r$  is the distance from the image of the line source to the receiver, and the  $+(-)$  sign is used for the case of a magnetic (electric) line source. The diffracted field is given by [4]

$$u^{dif} \sim u^{inc}(Q_e) D_h \frac{e^{-jk\rho}}{\sqrt{\rho}} \quad (2.4)$$

where  $u^{inc}(Q_e)$  is the field incident on the edge, and the diffraction coefficient,  $D_h$ , is written as

$$D_h = \frac{-e^{-j\pi/4}}{2n\sqrt{2\pi k}} \left[ \begin{aligned} & \left\{ \cot \left[ \frac{\pi + (\phi - \phi')}{2n} \right] F[kL^i a^+(\phi - \phi')] + \right. \\ & \left. \cot \left[ \frac{\pi - (\phi - \phi')}{2n} \right] F[kL^i a^-(\phi - \phi')] \right\} \\ & \mp \left\{ \cot \left[ \frac{\pi + (\phi + \phi')}{2n} \right] F[kL^{rn} a^+(\phi + \phi')] + \right. \\ & \left. \cot \left[ \frac{\pi - (\phi + \phi')}{2n} \right] F[kL^{rn} a^-(\phi + \phi')] \right\} \end{aligned} \right] \quad (2.5)$$

The transition function is defined by [4]

$$F(x) = 2j\sqrt{x} e^{jx} \int_{\sqrt{x}}^{\infty} e^{-j\tau^2} d\tau \quad (2.6)$$

where one takes the principal branch of the square root,

$$a^{\pm}(\beta) = 2 \cos^2 \left[ \frac{2n\pi N^{\pm} - \beta}{2} \right] \quad (2.7)$$

where  $N^{\pm}$  are the integers which most nearly satisfy the equations

$$2\pi n N^{\pm} - \beta = \pm\pi \quad (2.8)$$

and

$$n = 2 - \text{WA}/\pi \quad (2.9)$$

where WA is the wedge angle. Note that the  $e^{j\omega t}$  time convention is assumed and suppressed throughout this study.

The subscripts  $s$  and  $h$  on the diffraction coefficient,  $D_{\lambda}$ , correspond to the cases of the electric and magnetic line sources, respectively (these are the soft and hard boundary conditions). The four terms in the diffraction coefficient correspond to the "n face" incident shadow boundary (ISB), the "o face" ISB, the "n face" reflection shadow boundary (RSB), and the "o face" RSB; respectively. (The  $o$  and  $n$  faces may be chosen arbitrarily, whereas the angles  $\phi$  and  $\phi'$  must be measured from the  $o$  face.) The transition function, as introduced by Kouyoumjian and Pathak [4], contains a Fresnel integral which is easily evaluated using a computer algorithm. The magnitude and phase of the transition function are shown in Figure 2. Note that when  $x > 10$ ,  $F(x) \cong 1$ . The region near a shadow boundary, where  $F(x)$  is not close to one, is called a transition region. In a transition region, the high-frequency diffracted field can not be considered ray-optical.

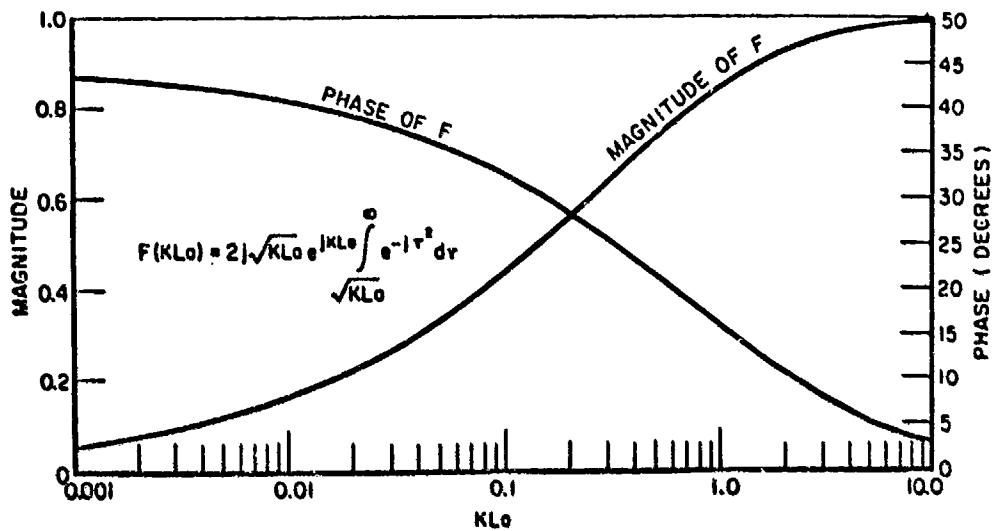


Figure 2: Transition function.

The L parameters are known as the distance parameters, and are given by

$$L^i = \frac{\rho' \rho}{\rho' + \rho} \quad (2.10)$$

$$L^{rn} = \frac{\rho_c^n \rho}{\rho_c^n + \rho}, \text{ and} \quad (2.11)$$

$$L^{ro} = \frac{\rho_c^o \rho}{\rho_c^o + \rho} \quad (2.12)$$

where  $\rho_c^n$  and  $\rho_c^o$  are the caustic distances for the reflected wavefronts emanating from the edge for the  $n$  and  $o$  faces, respectively. (For a wedge composed of two flat faces,  $\rho_c^n = \rho_c^o = \rho'$ .) The functions  $a^\pm(\cdot)$  are a measure of the angular separation between the field point and the shadow boundaries. Finally, note that the following rules must be observed:

1.  $L^i \geq \lambda/10$  (necessary for asymptotic solution)

2.  $0 \leq \phi, \phi' \leq n\pi$ , and

3. If  $\phi' = 0$  or  $\phi' = n\pi$ , one has grazing incidence and must multiply the diffraction coefficient by  $1/2$ .

### 2.3 Three-Dimensional Wedge Diffraction

In the previous section, the scalar fields associated with a cylindrical wave incident on a perfectly-conducting two-dimensional wedge were considered. The problem of the three-dimensional wedge (formed by two plane surfaces) is similar in that the total field again consists of incident, reflected, and diffracted fields. However, the three-dimensional case deals with a point source, in general, and thus illumination by an obliquely incident spherical wave. Also, the incident field may be arbitrarily polarized. To simplify the expressions for the reflected and diffracted fields, two ray-fixed coordinate systems will be introduced.

Consider an electric field  $\mathbf{E}^i$  incident on a perfectly-conducting planar surface, as shown in Figure 3. Let  $\hat{n}$  be the unit normal vector to the surface,  $\hat{I}$  be the incident unit vector from the source to a reflection point  $Q_R$  on the surface, and  $\hat{R}$  be the reflection unit vector. The vectors  $\hat{n}$  and  $\hat{I}$  define the ordinary plane of incidence. One may then define the following unit vectors:

$$\hat{u}_\perp = \frac{\hat{n} \times \hat{I}}{|\hat{n} \times \hat{I}|} \quad (2.13)$$

$$\hat{u}_\parallel^i = \hat{I} \times \hat{u}_\perp, \text{ and} \quad (2.14)$$

$$\hat{u}_\parallel^r = \hat{R} \times \hat{u}_\perp \quad (2.15)$$

where  $\perp$  and  $\parallel$  indicate vectors perpendicular and parallel, respectively, to the ordinary plane of incidence. These orthogonal unit vectors form a ray-fixed coordinate system. The field of a ray traveling in the incident or reflected directions is completely specified by its components  $E_\perp$  and  $E_\parallel$ . Thus, the reflected field  $\mathbf{E}^r(s)$

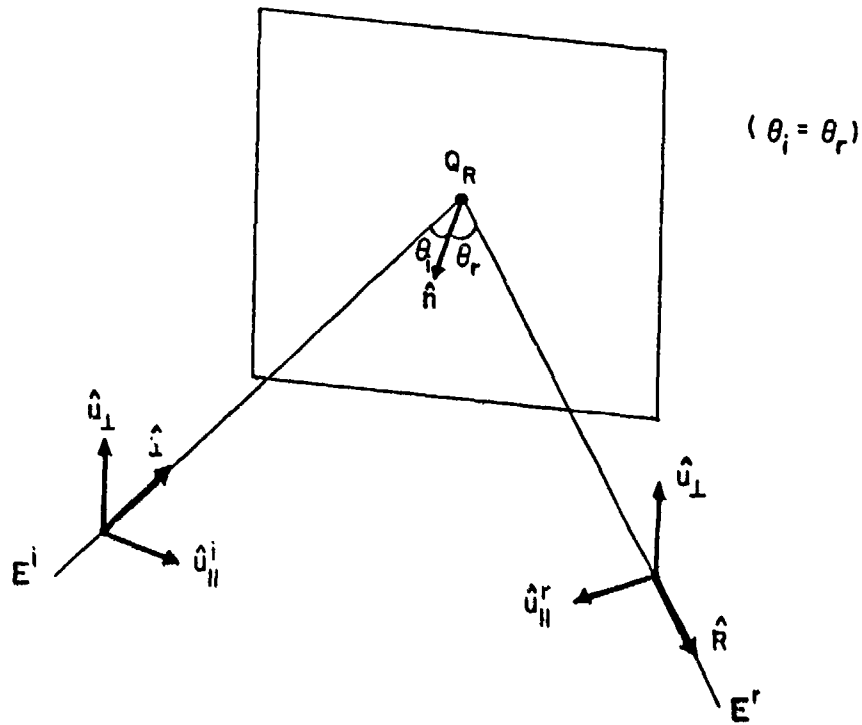


Figure 3: Ray-fixed coordinate system for 3D reflection.

at a distance  $s$  along the reflected ray from the reflection point  $Q_R$  may be written as

$$\begin{bmatrix} E_{\parallel}^r(s) \\ E_{\perp}^r(s) \end{bmatrix} = \begin{bmatrix} 1 & 0 \\ 0 & -1 \end{bmatrix} \begin{bmatrix} E_{\parallel}^i(Q_R) \\ E_{\perp}^i(Q_R) \end{bmatrix} e^{-jks} \quad (2.16)$$

where  $\mathbf{E}^i(Q_R)$  is the field incident at  $Q_R$ . The reflected field can also be written as

$$\mathbf{E}^r(s) = \mathbf{E}^i(Q_R) \cdot \mathcal{R} e^{-jks} \quad (2.17)$$

where  $\mathcal{R}$  is the dyadic reflection coefficient and is given by

$$\mathcal{R} = \hat{u}_{\parallel}^i \hat{u}_{\parallel}^r - \hat{u}_{\perp}^i \hat{u}_{\perp}^r \quad (2.18)$$

To examine the diffracted field in this problem, consider a source point and observation point as shown in Figure 4. Let the distance from the source point to

the edge diffraction point ( $Q_E$ ) be denoted by  $s'$ , and the distance from  $Q_E$  to the observation point be denoted by  $s$ . Let  $\beta'_o$  be the angle of incidence; that is, the angle formed by the incident ray and the diffracting edge. When an incident ray strikes the edge, it produces a cone of diffracted rays. The axis of the cone is the diffracting edge, while the cone half-angle (the angle of diffraction),  $\beta_o$ , is equal to the angle of incidence,  $\beta'_o$ . The equality of these two angles uniquely determines the edge diffraction point,  $Q_E$ .

Let  $\hat{e}$  be the unit vector parallel to the diffracting edge,  $\hat{I}$  be the incident unit vector from the source to the diffraction point,  $Q_E$ , and  $\hat{D}$  be the diffraction unit vector from  $Q_E$  to the observation point. The plane defined by  $\hat{e}$  and  $\hat{I}$  is the edge-fixed plane of incidence, while the plane defined by  $\hat{e}$  and  $\hat{D}$  is the edge-fixed plane of diffraction, as shown in Figure 5. One may define the following unit vectors:

$$\hat{\phi}' = \frac{-\hat{e} \times \hat{I}}{|\hat{e} \times \hat{I}|} \quad (2.19)$$

$$\hat{\beta}'_o = \hat{\phi}' \times \hat{I} \quad (2.20)$$

$$\hat{\phi} = \frac{\hat{e} \times \hat{D}}{|\hat{e} \times \hat{D}|}, \text{ and} \quad (2.21)$$

$$\hat{\beta}_o = \hat{\phi} \times \hat{D} . \quad (2.22)$$

The unit vectors  $\hat{\beta}'_o$  and  $\hat{\phi}'$  are parallel and perpendicular, respectively, to the edge-fixed plane of incidence, and form the ray-fixed coordinate system for the incident ray; the unit vectors  $\hat{\beta}_o$  and  $\hat{\phi}$  are parallel and perpendicular, respectively, to the edge-fixed plane of diffraction, and form the ray-fixed coordinate system for the diffracted ray. (Recall that in the case of 2D wedge diffraction, the specification of the  $o$  and  $n$  faces was arbitrary. In the current problem, one may arbitrarily assign the direction of  $\hat{e}$ . Once chosen, however, the  $o$  and  $n$  faces are also determined. This results from the unit vector definitions above, and the conventions shown in Figure 4.)

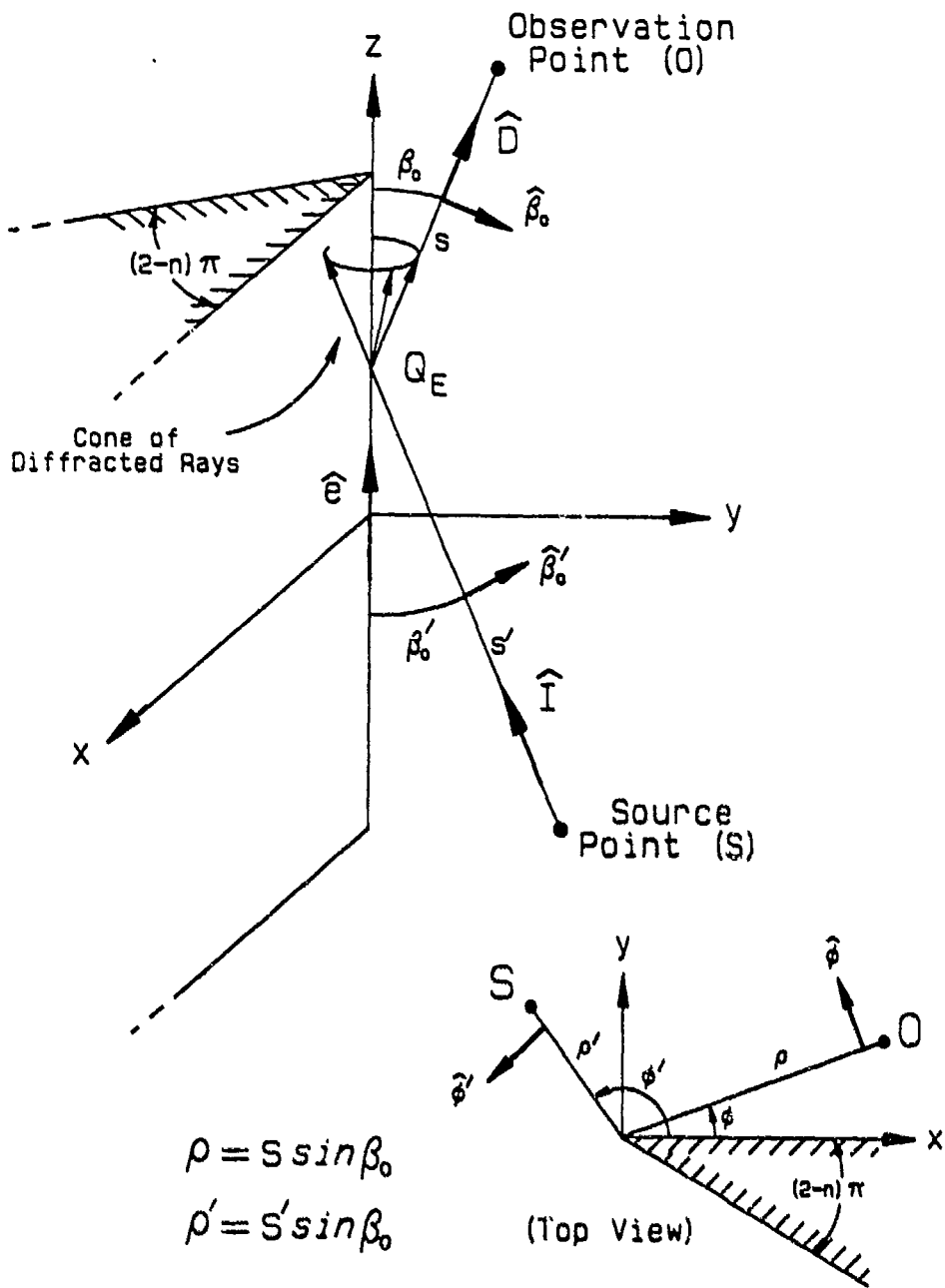


Figure 4: Geometry for diffraction from 3D wedge.

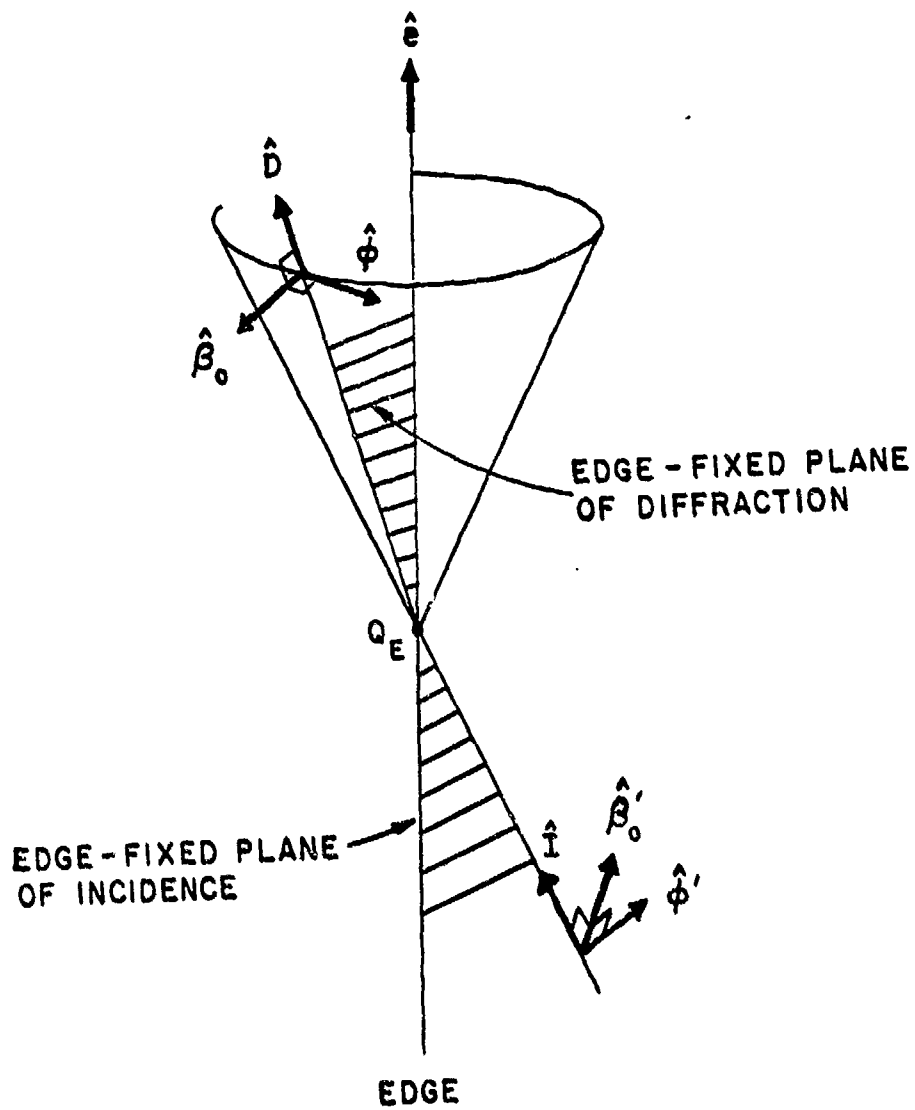


Figure 5: Ray-fixed coordinate system for 3D diffraction.

Using these vector directions, the diffracted field at the observation point is written as

$$\begin{bmatrix} E_{\beta_o}^d(s) \\ E_{\phi}^d(s) \end{bmatrix} \sim \begin{bmatrix} -D_s & 0 \\ 0 & -D_h \end{bmatrix} \begin{bmatrix} E_{\beta_o}^i(Q_E) \\ E_{\phi}^i(Q_E) \end{bmatrix} \sqrt{\frac{\rho}{s(\rho+s)}} e^{-jks} \quad (2.23)$$

where

$$D_h = \frac{-e^{-j\pi/4}}{2n\sqrt{2\pi k \sin \beta_o}} \left[ \begin{aligned} & \left\{ \cot \left[ \frac{\pi + (\phi - \phi')}{2n} \right] F[kLa^+(\phi - \phi')] + \right. \\ & \qquad \left. \cot \left[ \frac{\pi - (\phi - \phi')}{2n} \right] F[kLa^-(\phi - \phi')] \right\} \\ & \mp \left\{ \cot \left[ \frac{\pi + (\phi + \phi')}{2n} \right] F[kLa^+(\phi + \phi')] + \right. \\ & \qquad \left. \cot \left[ \frac{\pi - (\phi + \phi')}{2n} \right] F[kLa^-(\phi + \phi')] \right\} \end{aligned} \right] . \quad (2.24)$$

Since the wedge is formed by two plane surfaces, the distance parameters in all four terms of the diffraction coefficient are given simply by

$$L = \frac{ss'}{s+s'} \sin^2 \beta_o . \quad (2.25)$$

The functions  $a^\pm(\cdot)$  and  $F(\cdot)$  were defined earlier. The diffracted field may also be written as

$$E^d(s) \sim \mathbf{E}^i(Q_E) \cdot \mathcal{D} \sqrt{\frac{\rho}{s(\rho+s)}} e^{-jks} \quad (2.26)$$

where  $\mathcal{D}$  is the dyadic diffraction coefficient and is given by

$$\mathcal{D} = -\hat{\beta}'_o \hat{\beta}_o D_s - \hat{\phi}' \hat{\phi} D_h . \quad (2.27)$$

The geometrical optics and edge diffracted fields that have been presented are high-frequency asymptotic solutions to Maxwell's equations. They are not valid at or near field caustics (although one may allow the field point to cross a caustic by introducing a proper phase shift). The large parameter in the asymptotic

approximation for the edge diffracted field is  $kL$ , which means that  $\beta_0$ ,  $s$ , and  $s'$  cannot be arbitrarily small. The incident field is assumed to be slowly varying at the edge diffraction point, except for its phase variation along the incident ray. Also, one should note that this presentation has been limited to a wedge formed by two plane surfaces, with a straight edge. Curvature of an edge primarily modifies the spread factor, while surface curvature primarily modifies the distance parameters. A much more detailed and general presentation of this subject can be found in [4].

## 2.4 Corner Diffraction

The three-dimensional edge diffraction solution dealt with thus far has been for an infinitely long edge. In an actual physical problem, the scattering object must have finite length edges. Burnside, Wang and Pelton [5] have developed a corner diffraction coefficient which compensates for the termination of the edge. Their solution is based on the equivalent edge currents that would exist in the absence of the corner. They employed these currents in the radiation integral, and evaluated the integral asymptotically. This analysis was characterized by a saddle point near an endpoint. The corner diffraction term was then found by appropriately (but empirically) modifying the asymptotic result. Their solution has proven to accurately predict the scattering from many plate geometries.

The corner diffraction geometry is illustrated in Figure 6, where a corner exists in a perfectly-conducting flat plate. The corner diffracted fields are broken down into components associated with each individual edge. In Figure 6, the corner diffracted fields associated with the  $\hat{z}$  directed edge are considered. For the source and observation points indicated, there is an edge diffraction point indicated by  $Q_E$ . As the observation point moves in the  $-\hat{z}$  direction, the diffraction point,

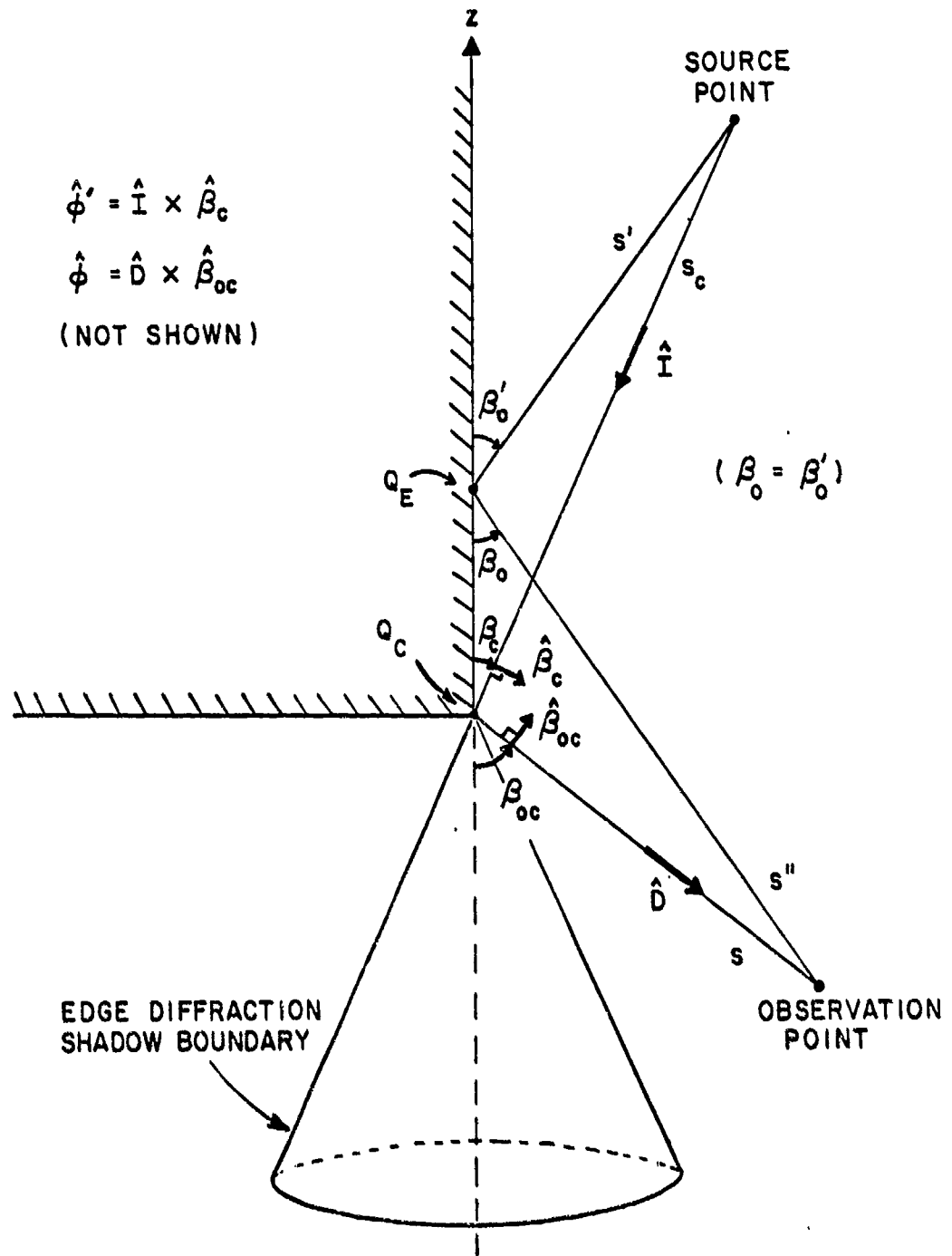


Figure 6: Corner diffraction geometry.

$Q_E$ , also moves in the  $-\hat{z}$  direction. Eventually it moves beyond the physical limits of the edge, and the edge diffracted field stops abruptly. The corner diffracted field compensates for this discontinuity, as the edge diffracted field compensated for the discontinuities in the GO field. Whether  $Q_E$  is on the edge itself, or on the imaginary extension of this edge, the corner diffracted field will exist.

The angles  $\beta_o$ ,  $\beta_c$ , and  $\beta_{oc}$ , and the distances  $s'$ ,  $s''$ ,  $s_c$ , and  $s$  are illustrated in Figure 6. The vector directions used to express the incident and diffracted fields are given by

$$\hat{\phi}' = \frac{-\hat{e} \times \hat{I}}{|\hat{e} \times \hat{I}|} \quad (2.28)$$

$$\hat{\beta}_c = \hat{\phi}' \times \hat{I} \quad (2.29)$$

$$\hat{\phi} = \frac{\hat{e} \times \hat{D}}{|\hat{e} \times \hat{D}|}, \text{ and} \quad (2.30)$$

$$\hat{\beta}_{oc} = \hat{\phi} \times \hat{D}. \quad (2.31)$$

The corner diffracted fields associated with one corner and one edge of a perfectly-conducting flat plate in the near field with spherical wave incidence are given by [5]

$$\left. \begin{array}{l} E_{\beta_{oc}}^c \\ E_{\phi}^c \end{array} \right\} \sim - \frac{E_{\beta_c}^i(Q_c) C_s(Q_E)}{E_{\phi'}^i(Q_c) C_h(Q_E)} \left\{ \frac{e^{-j\pi/4} \sqrt{\sin \beta_c \sin \beta_{oc}}}{\sqrt{2\pi k} (\cos \beta_{oc} - \cos \beta_c)} \times \right. \quad (2.32)$$

$$\left. F[kL_c a(\pi + \beta_{oc} - \beta_c)] \frac{e^{-jks}}{s} \right.$$

where

$$C_h(Q_E) = \frac{-e^{-j\pi/4}}{2\sqrt{2\pi k} \sin \beta_o} \left\{ \frac{F[kLa(\phi - \phi')]}{\cos(\frac{\phi - \phi'}{2})} \left| F \left[ \frac{La(\phi - \phi')/\lambda}{kL_c a(\pi + \beta_{oc} - \beta_c)} \right] \right| \right. \quad (2.33)$$

$$\left. \mp \frac{F[kLa(\phi + \phi')]}{\cos(\frac{\phi + \phi'}{2})} \left| F \left[ \frac{La(\phi + \phi')/\lambda}{kL_c a(\pi + \beta_{oc} - \beta_c)} \right] \right| \right\}.$$

Note that the transition function was defined earlier, while the distance parameters are expressed as follows:

$$L = \frac{s' s''}{s' + s''} \sin^2 \beta_o \quad (2.34)$$

$$L_c = \frac{s_c s}{s_c + s} \quad (2.35)$$

and

$$a(\phi \pm \phi') = 2 \cos^2 \left( \frac{\phi \pm \phi'}{2} \right) \quad (2.36)$$

The corner diffraction coefficient,  $C_h(Q_E)$ , is a modified version of the edge diffraction coefficient,  $D_h(Q_E)$ . The modification factor

$$\left| F \left[ \frac{La(\phi \pm \phi')/\lambda}{kL_c a(\pi + \beta_{oc} - \beta_c)} \right] \right|$$

is a heuristic function which helps to avoid the abrupt sign changes in  $C_h(Q_E)$  as the observer passes through the geometrical optics shadow boundaries of the edge.

The corner diffracted fields associated with the other edge are treated similarly. Thus, depending on the source and observer locations, there may be edge diffracted fields from either or both edges, but there will always be a corner diffracted field term associated with each edge. The total effect of the corner is found by superimposing the contributions associated with each individual edge. This topic is discussed further and applied to a number of plate geometries by Sikta *et al* [10].

Consider now the case of a corner formed out of a three-dimensional wedge. The corner of a cube is an example of this type of geometry. The corner diffracted fields associated with one corner and one edge of such a perfectly-conducting three-dimensional wedge in the near field with spherical wave incidence are again given by Equation (2.32), where the corner diffraction coefficient is now written as

$$C_h = \frac{-e^{-j\pi/4}}{2n\sqrt{2\pi k} \sin \beta_o} \times \quad (2.37)$$

$$\left[ \left\{ \cot \left[ \frac{\pi + (\phi - \phi')}{2n} \right] F[kLa^+(\phi - \phi')] \left| F \left[ \frac{La^+(\phi - \phi')/\lambda}{kLca(\pi + \beta_{oc} - \beta_c)} \right] \right| + \right. \right. \\ \left. \left. \cot \left[ \frac{\pi - (\phi - \phi')}{2n} \right] F[kLa^-(\phi - \phi')] \left| F \left[ \frac{La^-(\phi - \phi')/\lambda}{kLca(\pi + \beta_{oc} - \beta_c)} \right] \right| \right\} \right] \\ \mp \left\{ \cot \left[ \frac{\pi + (\phi + \phi')}{2n} \right] F[kLa^+(\phi + \phi')] \left| F \left[ \frac{La^+(\phi + \phi')/\lambda}{kLca(\pi + \beta_{oc} - \beta_c)} \right] \right| + \right. \\ \left. \cot \left[ \frac{\pi - (\phi + \phi')}{2n} \right] F[kLa^-(\phi + \phi')] \left| F \left[ \frac{La^-(\phi + \phi')/\lambda}{kLca(\pi + \beta_{oc} - \beta_c)} \right] \right| \right\} \right] .$$

The corner diffraction solution works very well for computing backscattered fields. In [10], the authors conclude that corner diffraction can be used to obtain the echo area of rather general flat plate structures. Unfortunately, since the corner diffraction solution was found heuristically, it does have its shortcomings. The diffracted fields it predicts may become discontinuous, particularly for some bistatic geometries. In some instances, the angles  $\phi$  and  $\phi'$  trigger a discontinuity that the modification factors cannot entirely eliminate. These values of  $\phi$  and  $\phi'$  correspond to shadow boundaries of the GO field. In terms of the corner diffraction solution, these are *false* shadow boundaries, since the corner diffracted field arises to smooth the edge diffraction shadow boundary. Nonetheless, the corner diffraction solution is very useful.

Figures 8 to 10 demonstrate both the validity of the corner diffraction solution for bistatic scattering cases and the occurrence of false shadow boundaries. Consider a plane wave incident at  $\theta^i = 45^\circ$ ,  $\phi^i = 0^\circ$  on a  $2\lambda$  square plate, as shown in Figure 7. Patterns are then computed for fixed  $\phi^s$  and for  $0^\circ < \theta^s < 360^\circ$ . Corner diffraction results are shown versus moment method results, both are calculated

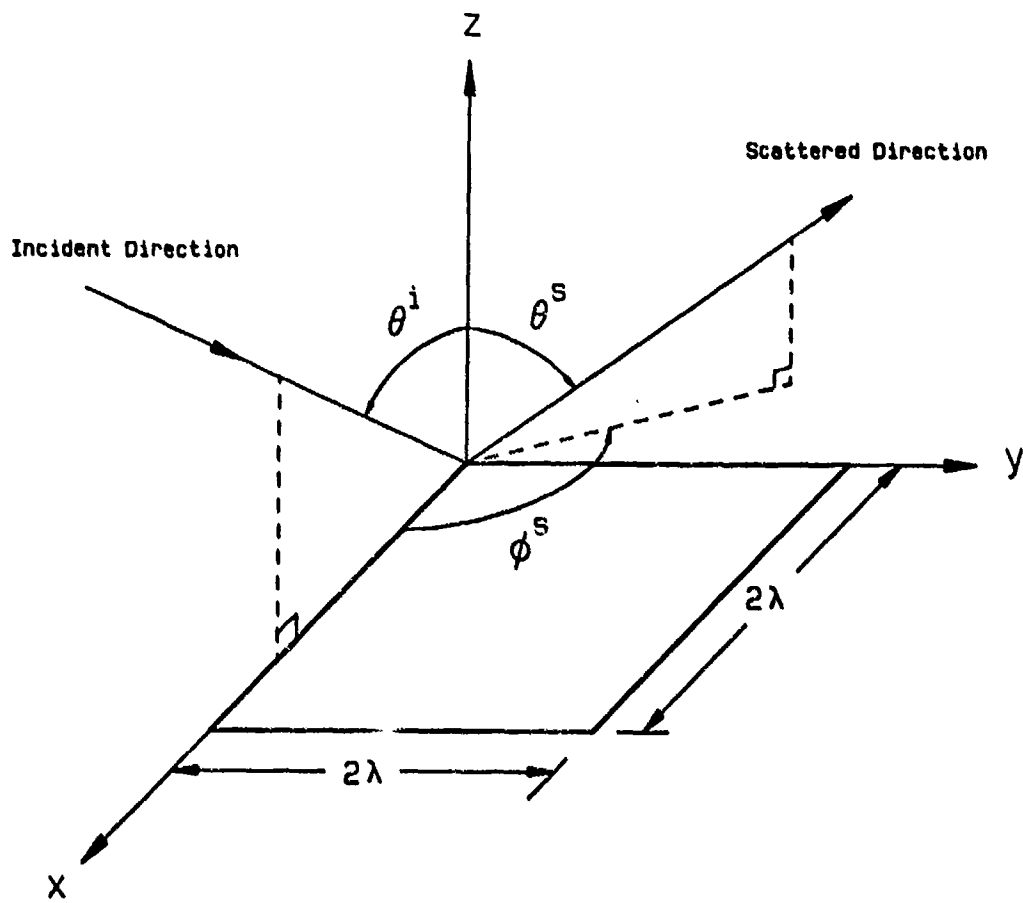


Figure 7: Geometry for scattering from a square flat plate.

in dB relative to a square wavelength. The actual computations were done by Brinkley [11]. The subscripts on  $\sigma$  refer to the source polarization and receiver polarization, in that order.

In Figure 8,  $\phi^s = 0.1^\circ$ , which places the observer near the plane of incidence. The nulls in the moment method results (for the  $\hat{\theta}\hat{\theta}$  polarization) at  $\theta^s = 90^\circ, 270^\circ$  are from higher order effects not present in the corner diffraction solution. Agreement between the two solutions is excellent. Note that there is a slight glitch in the corner diffraction results at  $\theta^s = 225^\circ, 315^\circ$  which is due to difficulties with the modification factor, in both its mathematical expression and its numerical computation. This difficulty is most pronounced in the plane of incidence ( $\phi^s = 0^\circ$ ). The value of  $0.1^\circ$  was chosen for  $\phi^s$  to lessen the dependence of the displayed results on the method of computation.

Figures 9 and 10 depict the cross-polarized and co-polarized results, respectively, for  $\phi^s = 122^\circ$ . The discontinuities seen in the corner diffraction solution are due to false shadow boundaries. Agreement with moment method results has weakened (in comparison with the case where the observer is near the plane of incidence), yet the dominant scattering behavior is predicted by the corner diffraction solution.

The diffraction mechanisms reviewed here serve as a foundation for scattering from dielectric objects, which is the subject of the next chapter.

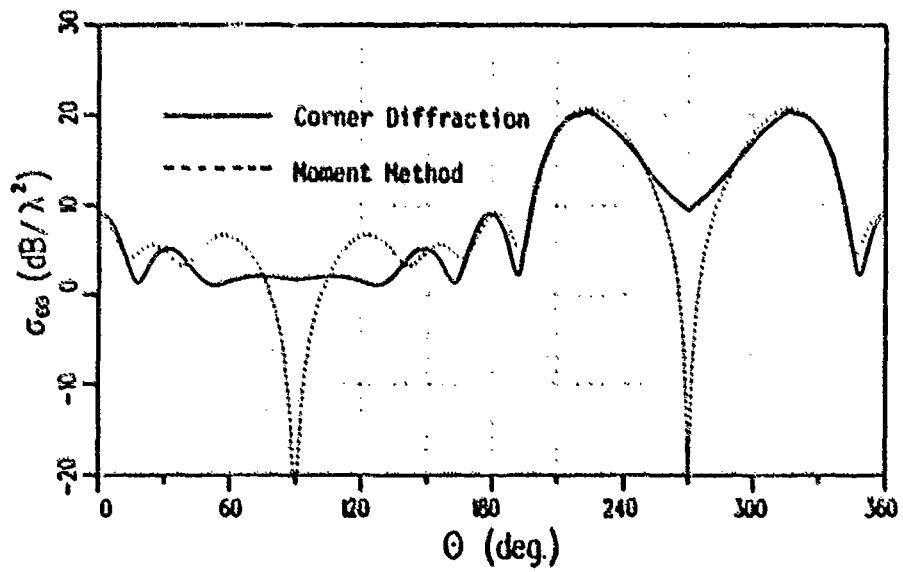
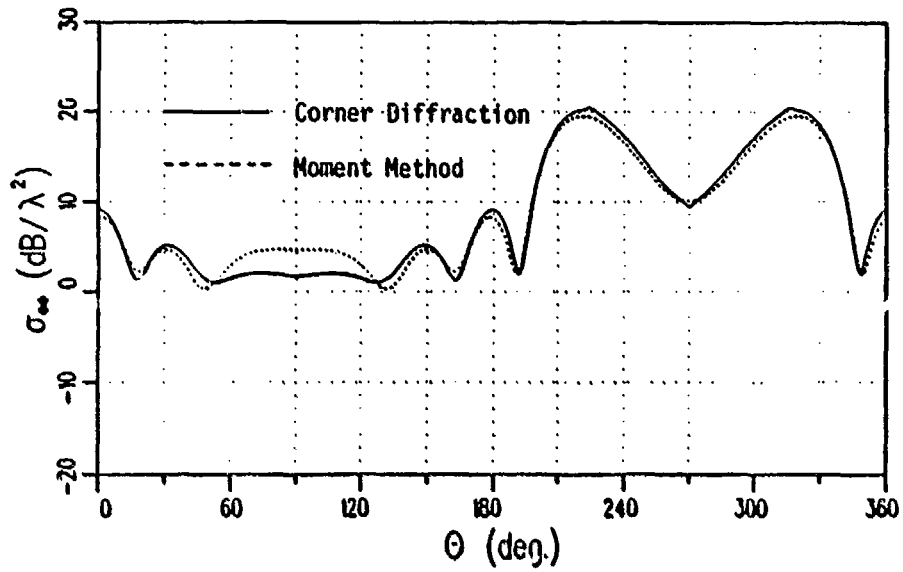


Figure 8: Flat plate scattering,  $\phi^s = 0.1^\circ$ , from [11].

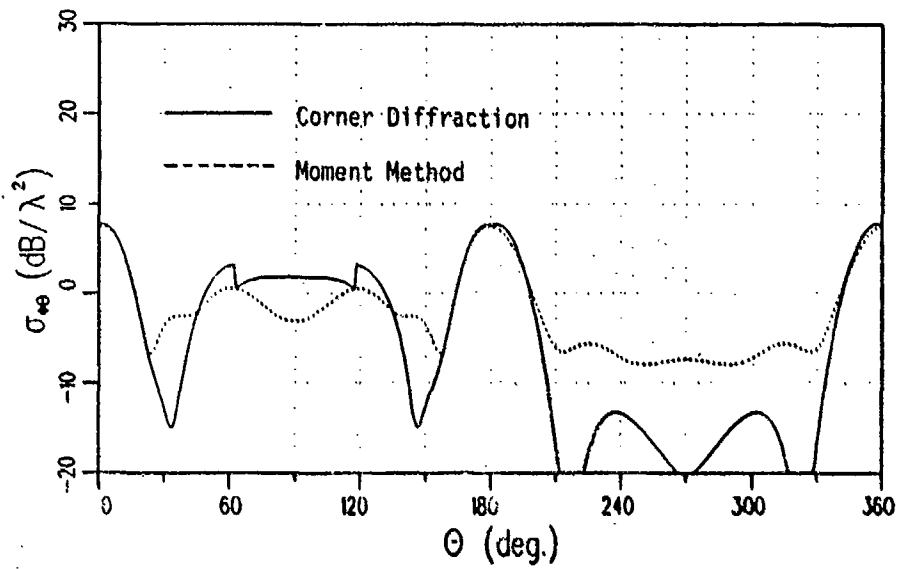
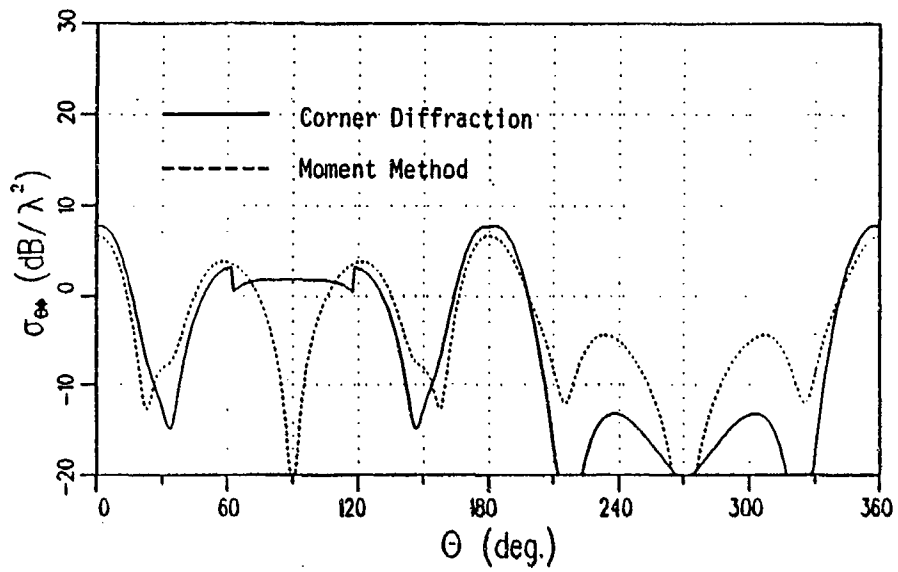


Figure 9: Flat plate scattering (cross-polarized fields),  $\phi^s = 122^\circ$ , from [11].

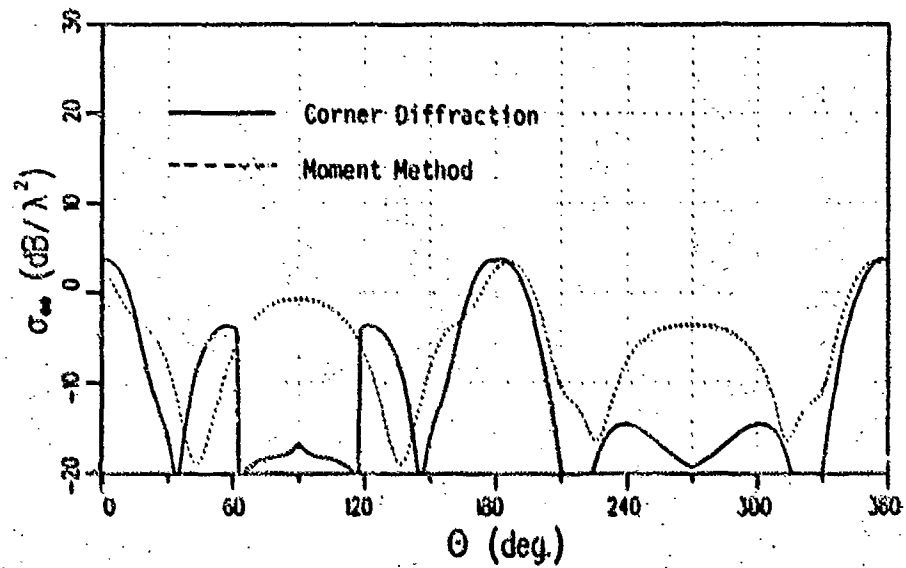
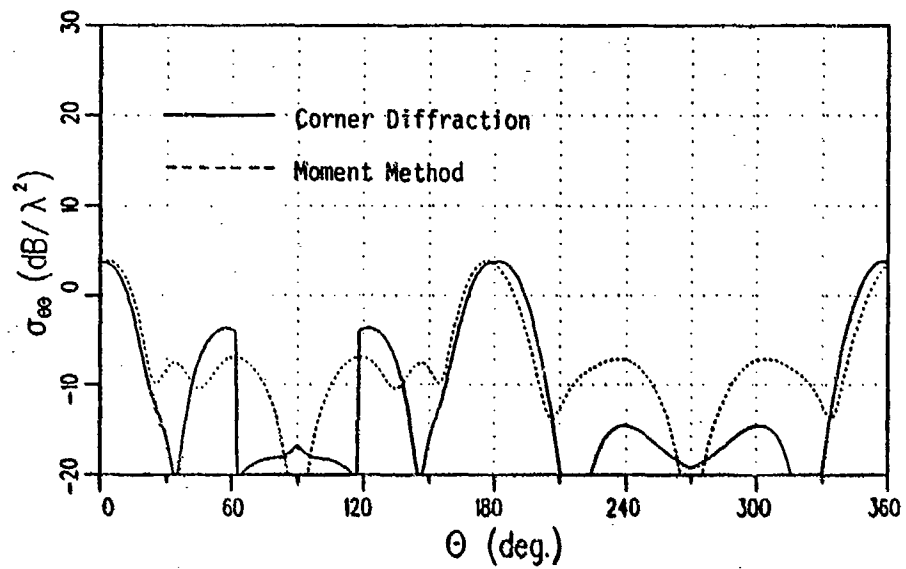


Figure 10: Flat plate scattering (co-polarized fields),  $\phi^s = 122^\circ$ , from [11].

## CHAPTER III

### DIFFRACTION FROM DIELECTRIC WEDGES AND CORNERS

#### 3.1 Introduction

The aim of this chapter is to develop a scattering formulation, based on the UTD, for a dielectric corner. The reflection and transmission of plane waves at a dielectric-dielectric interface are first reviewed. Next, two cases in which dielectric modifications have previously been made to the UTD are discussed. These were for the problems of edge diffraction from a two-dimensional dielectric slab [6] and from a two-dimensional dielectric wedge [7]. By extending the method arrived at in [7], a modified UTD solution is developed for three-dimensional dielectric edge and corner diffraction.

#### 3.2 Reflection and Transmission at a Dielectric Interface

In this section, attention is given to a linearly polarized plane wave obliquely incident on a planar interface between two media. Medium 1 is a non-magnetic, lossless dielectric; medium 2 is a non-magnetic and, in general, lossy dielectric.

Consider first the case of perpendicular polarization, where the electric field direction is perpendicular to the plane of incidence (the plane formed by the incident ray and the interface normal). This is illustrated in Figure 11. The reflection coefficient,  $R_{\perp}$ , is defined as the ratio of the reflected electric field amplitude to the incident electric field amplitude. The transmission coefficient,  $T_{\perp}$ , is defined as the

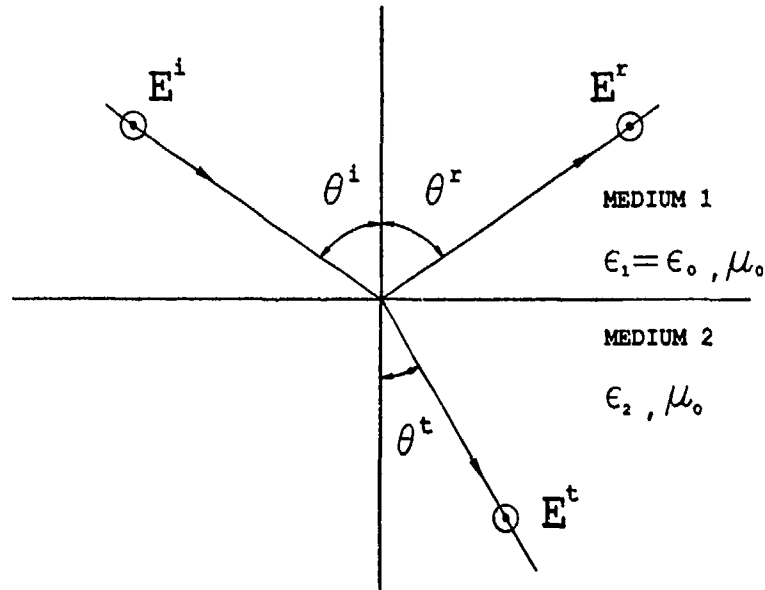


Figure 11: Reflection and transmission at a dielectric interface, perpendicular polarization.

ratio of the transmitted electric field amplitude to the incident electric field amplitude. These Fresnel coefficients can be found by applying the boundary conditions at the interface; that is, by enforcing the condition that the tangential electric and magnetic fields be continuous at the interface. Doing so results in the following

$$R_{\perp} = \frac{\cos \theta^i - \sqrt{(\epsilon_2/\epsilon_1) - \sin^2 \theta^i}}{\cos \theta^i + \sqrt{(\epsilon_2/\epsilon_1) - \sin^2 \theta^i}}, \text{ and} \quad (3.1)$$

$$T_{\perp} = \frac{2 \cos \theta^i}{\cos \theta^i + \sqrt{(\epsilon_2/\epsilon_1) - \sin^2 \theta^i}}. \quad (3.2)$$

Note that  $T_{\perp} = 1 + R_{\perp}$ .

Consider next the case of parallel polarization, as shown in Figure 12. The reflection coefficient,  $R_{\parallel}$ , is defined as the ratio of the reflected magnetic field amplitude to the incident magnetic field amplitude. The transmission coefficient,

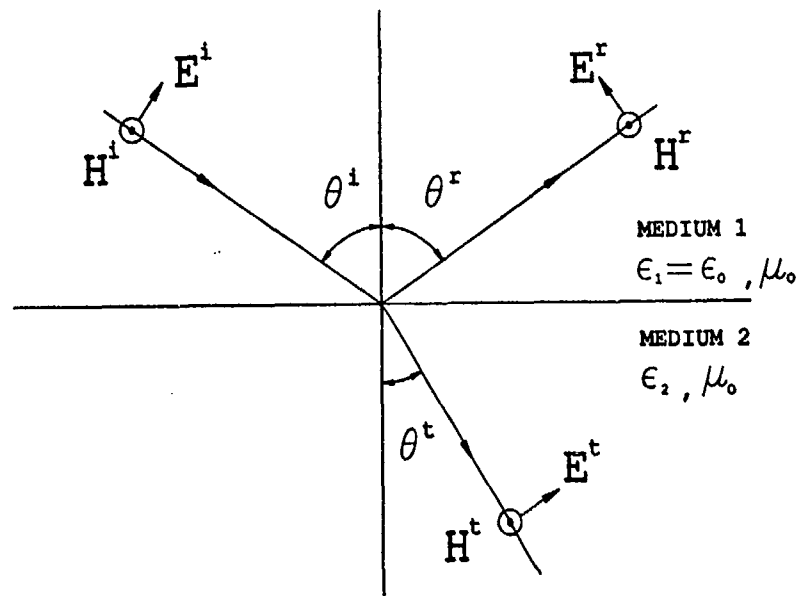


Figure 12: Reflection and transmission at a dielectric interface, parallel polarization.

$T_{\parallel}$ , is defined as the ratio of the transmitted magnetic field amplitude to the incident magnetic field amplitude. Enforcing boundary conditions as before, one finds that

$$R_{\parallel} = \frac{(\epsilon_2/\epsilon_1) \cos \theta^i - \sqrt{(\epsilon_2/\epsilon_1) - \sin^2 \theta^i}}{(\epsilon_2/\epsilon_1) \cos \theta^i + \sqrt{(\epsilon_2/\epsilon_1) - \sin^2 \theta^i}}, \text{ and} \quad (3.3)$$

$$T_{\parallel} = \frac{2(\epsilon_2/\epsilon_1) \cos \theta^i}{(\epsilon_2/\epsilon_1) \cos \theta^i + \sqrt{(\epsilon_2/\epsilon_1) - \sin^2 \theta^i}}. \quad (3.4)$$

Note that  $T_{\parallel} = 1 + R_{\parallel}$ . Since the incident and reflected fields are in the same medium, the ratio of the reflected electric field amplitude to the incident electric field amplitude is also given by  $R_{\parallel}$ .

For both polarizations, one finds that  $\theta^r = \theta^i$  and  $\sin \theta^t = \sqrt{\epsilon_1/\epsilon_2} \sin \theta^i$ , which are known as Snell's laws of reflection and refraction, respectively.

This study is concerned with the Fresnel reflection coefficients,  $R_{\perp}$  and  $R_{\parallel}$ , for reasons that will become apparent later. Note that  $R_{\perp}$  and  $R_{\parallel}$  are complex for complex  $\epsilon_2$ . Also, if  $\epsilon_2$  is real but less than  $\epsilon_1$ ,  $R_{\perp}$  and  $R_{\parallel}$  will be complex; however, that situation will not arise here. Complex  $\epsilon_2$  will also result in the angle of refraction  $\theta^t$  being complex. (In this instance,  $\theta^t$  is clearly not the true angle of refraction. The true angle of refraction can be found in a manner analogous to that done by Stratton [12, pages 500-505] for the problem of refraction in a conducting medium. This is not presently of interest.)

Using the ray-fixed coordinate system for three-dimensional reflection shown in Figure 3 (Section 2.3), the reflected field  $\mathbf{E}^r(s)$  is written as

$$\begin{bmatrix} E_{\parallel}^r(s) \\ E_{\perp}^r(s) \end{bmatrix} = \begin{bmatrix} R_{\parallel} & 0 \\ 0 & R_{\perp} \end{bmatrix} \begin{bmatrix} E_{\parallel}^i(Q_R) \\ E_{\perp}^i(Q_R) \end{bmatrix} e^{-jks} \quad (3.5)$$

where  $\mathbf{E}^i(Q_R)$  is the field incident at a reflection point,  $Q_R$ , and  $s$  is the distance along the reflected ray from  $Q_R$ .

Figures 13 and 14 illustrate the behavior of  $|R_{\parallel}|$  and  $|R_{\perp}|$  versus angle of incidence for three values of  $\epsilon_2$ . Note that the complex permittivity  $\epsilon_2$  can be written as  $\epsilon_2 = \epsilon_2' - j\epsilon_2''$ , where  $\epsilon_2''$  represents the lossy nature of the dielectric. When the material is lossless,  $|R_{\parallel}|$  vanishes at the Brewster (or polarizing) angle. Also, as grazing incidence is approached, both  $|R_{\parallel}|$  and  $|R_{\perp}|$  approach unity.

### 3.3 Two-Dimensional Dielectric Slab

The first application of the UTD to a dielectric scatterer was developed by Burnside and Burgener [6], who studied the case of a thin, lossless dielectric slab. The geometry is illustrated in Figure 15. The dielectric slab they considered was

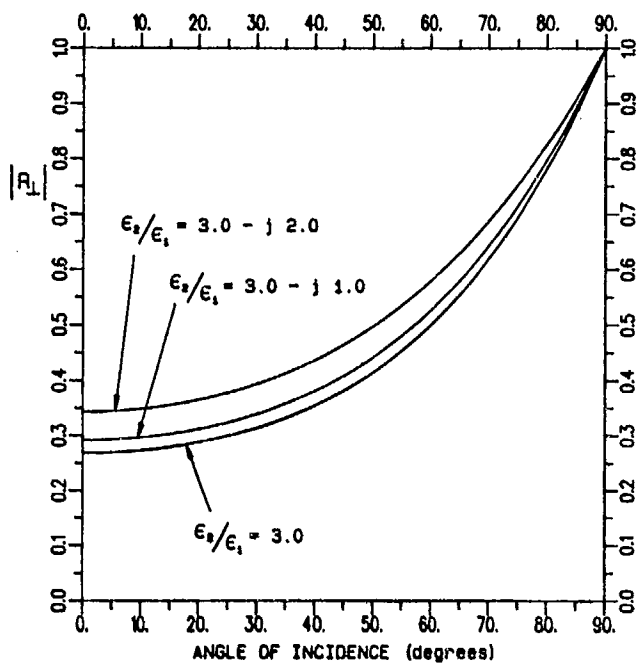


Figure 13: Plot of  $|R_{\perp}|$  vs.  $\theta^i$  for various  $\epsilon_2$ .

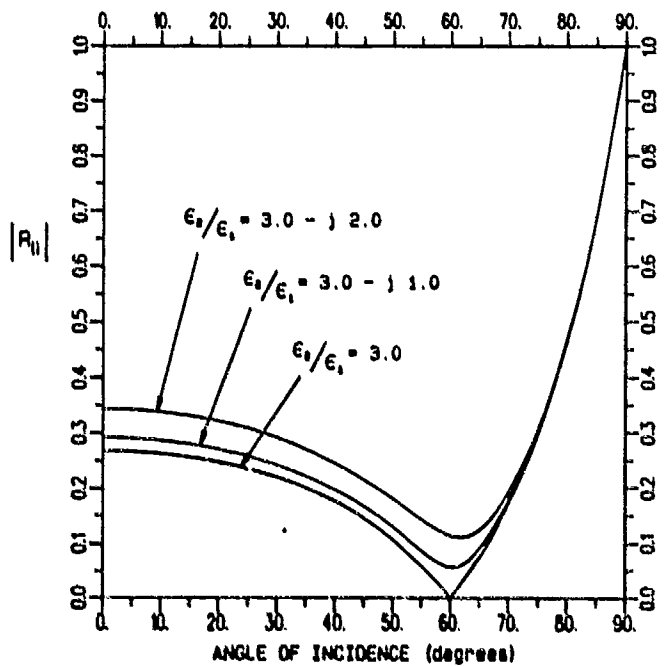


Figure 14: Plot of  $|R_{\parallel}|$  vs.  $\theta^i$  for various  $\epsilon_2$ .

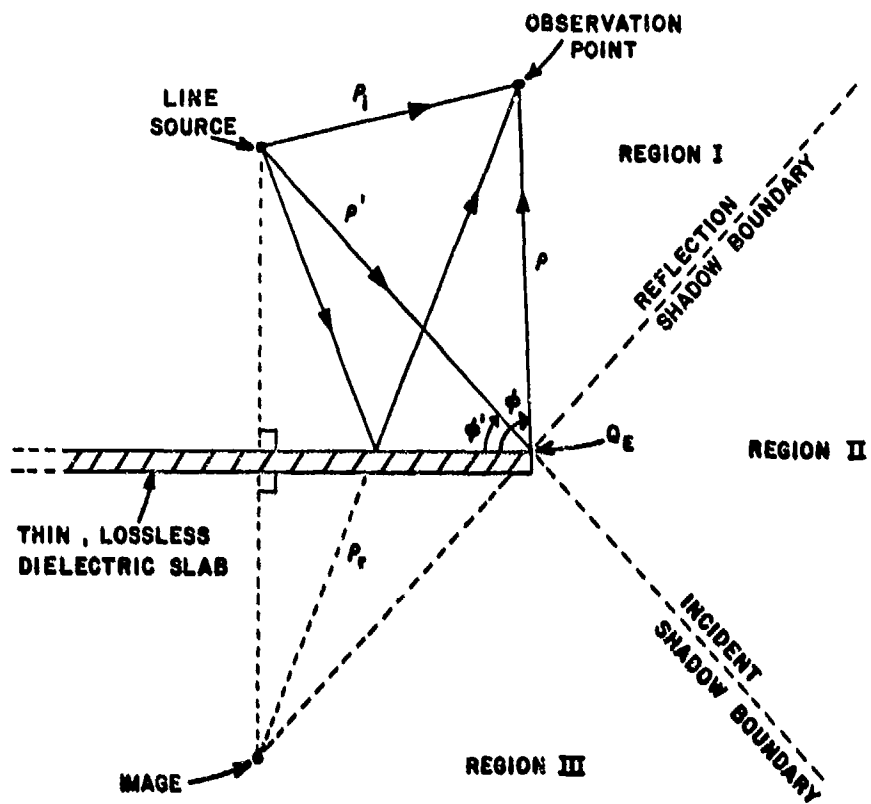


Figure 15: Geometry for diffraction from a 2D semi-infinite dielectric slab.

of any thin uniform material, but subject to the following restrictions:

- The diffractions can be assumed to emanate from the edge point  $Q_E$ .
- Energy leaving  $Q_E$  tangential to the slab, as a surface wave or a transmission through the endface, can be assumed negligible.
- Loss within the slab can be assumed negligible.

They first wrote expressions for the incident, reflected, and transmitted fields of a semi-infinite dielectric slab (assuming unit magnitude excitation) as follows:

$$u^{inc} = \begin{cases} \frac{e^{-jk\rho_i}}{\sqrt{\rho_i}} & \text{in regions I and II, and} \\ 0 & \text{in region III} \end{cases} \quad (3.6)$$

$$u^{ref} = \begin{cases} R^{total} \frac{e^{-jk\rho_r}}{\sqrt{\rho_r}} & \text{in region I, and} \\ 0 & \text{in regions II and III} \end{cases} \quad (3.7)$$

and

$$u^{tran} = \begin{cases} 0 & \text{in regions I and II, and} \\ T^{total} \frac{e^{-jk\rho_i}}{\sqrt{\rho_i}} & \text{in region III.} \end{cases} \quad (3.8)$$

Note that the transmitted (reflected) field is written as the product of a total transmission (reflection) coefficient and the field that would have been incident upon the observer from the source (image) in the absence of the dielectric slab. The coefficients  $R^{total}$  and  $T^{total}$  account for the multiple interactions that take place within the slab to produce the total reflection and transmission fields, each of which is an infinite sum of waves. This is illustrated in Figure 16.  $R^{total}$  and  $T^{total}$  are each expressed as an infinite series, with each term in the series representing one component of the reflected or transmitted field, respectively.  $R^{total}$  and  $T^{total}$  are found by proper attention to the various phase delays and coefficients of single

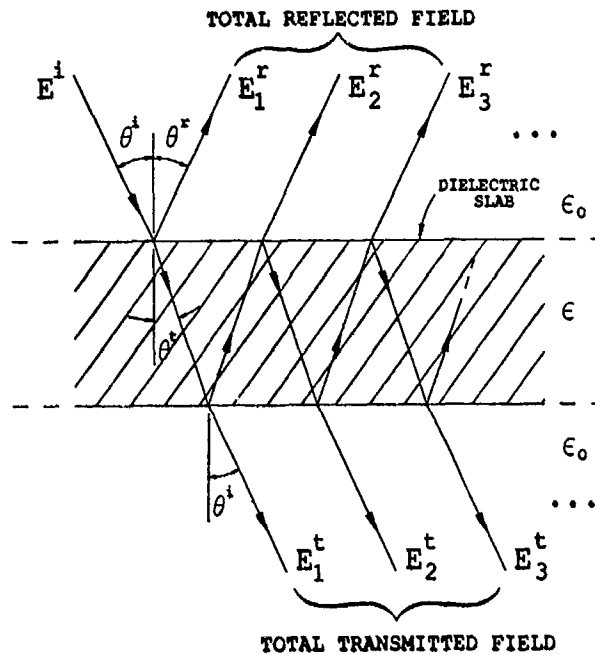


Figure 16: Multiple interactions within dielectric slab.

reflection and transmission involved. Note that plane wave propagation was assumed for the field incident on the slab, the field within the slab, and the reflected and transmitted fields. Thus, neither the source nor the observer must be too close to the slab.

Now, an expression for the diffracted field is desired. Comparing the dielectric semi-infinite slab to the perfectly-conducting case, one notes that the discontinuities at the two shadow boundaries have changed. This is due to a different reflected field, and to the presence of a transmitted field. Since the diffracted field arises to smooth out the discontinuities at the GO shadow boundaries, and since these discontinuities have been scaled by  $R^{total}$  and  $1 - T^{total}$  (as compared to the perfectly-conducting case), one should scale the diffracted field in the same manner. This was the approach proposed in [6]. Recall that the solution for the

two-dimensional perfectly-conducting half-plane is given by

$$u_h^{dif} \sim u^{inc}(Q_E) D_h \frac{e^{-jk\rho}}{\sqrt{\rho}} \quad (3.9)$$

where

$$D_h = \underbrace{D(\phi - \phi')}_{ISB \text{ term}} \mp \underbrace{D(\phi + \phi')}_{RSB \text{ term}} \quad (3.10)$$

and

$$D(\phi \pm \phi') = \frac{-e^{-j\pi/4} F[kLa(\phi \pm \phi')]}{2\sqrt{2\pi k} \cos\left(\frac{\phi \pm \phi'}{2}\right)} \quad (3.11)$$

The diffraction coefficient is then scaled to [6]

$$D_h = \left[ (1 - T_{\parallel}^{total}) D(\phi - \phi') + R_{\parallel}^{total} D(\phi + \phi') \right] \quad (3.12)$$

Note that the solution given above for the conducting half-plane is a special case of the wedge solution given in Section 2.2, found by setting the wedge angle to zero. Also, note that for a perfect conductor one has  $T_{\parallel}^{total} = 0$ , while  $R_{\parallel}^{total} = \mp 1$ . Thus, the proposed dielectric solution reduces to the correct result for the perfectly-conducting case.

The validity of this solution was verified by comparison with Moment Method results, for the case of Figure 17. In [6], it was concluded that the results were accurate for  $\rho$ , greater than a wavelength (which stems from the plane wave approximation), and for angles of incidence  $\phi$ , up to  $40^\circ$  (and possibly  $60^\circ$ ) from normal incidence (to avoid exciting a surface wave). Finally, the theory had made the assumption that the thickness  $D$  was less than  $1/10$  of a wavelength. However, based on comparison with measurements, accurate results were obtained for thicknesses up to  $1/2$  wavelength.

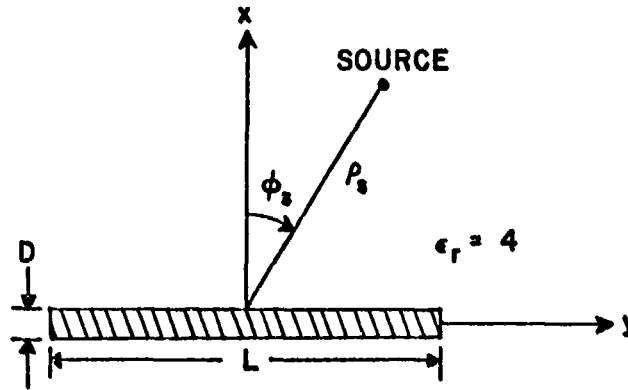


Figure 17: Finite 2D dielectric slab with line source illumination.

### 3.4 Two-Dimensional Dielectric Wedge

In the previous section, a dielectric modification was made to the UTD enabling edge diffraction calculations for a two-dimensional dielectric slab. This section considers the use of a similar modification for the more general problem of a two-dimensional dielectric wedge. This problem has received considerable attention by a number of authors. However, DeWitt[7] reports that many of the published solutions to this problem are either very limited or too complicated to be of practical use. Alternatively, Rawlins [8] has developed an approximate solution which can be numerically evaluated fairly easily. He derives a general integral equation for an infinite dielectric wedge with arbitrary wedge angle and permittivity. A Neumann series solution of the integral equation is then found through a perturbation technique. Rawlins takes the first term of this series and, using asymptotic methods, finds explicit expressions for the diffracted field of a *right angle* dielectric wedge under these constraints:

- The incident field is planar, with the electric field vector parallel to the edge of the wedge.

- One must have  $1 < \epsilon_r < 2$  for convergence of the Neumann series.
- The incident direction is in the quadrant opposite the wedge.

Rawlins' solution will be used later for comparison with the solution to be presented here.

The dielectric modification to the UTD discussed now was proposed by DeWitt [7], as an extension of the work done in the previous section. Since it is in the UTD format, it will be numerically efficient. Furthermore, as a simple modification to the UTD, it will not have the constraints mentioned above. The first step in this modification is to consider the effect that the dielectric material has on the discontinuities at the shadow boundaries. It is immediately apparent that the wedge problem is much more complex than the slab. One cannot speak of the reflected or transmitted fields alone in that the multiple interactions which occur within the wedge are of a more complicated nature. However, it was found in [7] that the following method works very well. First, due to the vanishing wedge thickness at the edge, energy will pass through the tip and tend to smooth the discontinuity at the ISB; thus, the ISB terms in the diffracted field are considered negligible. Second, it was chosen to modify the RSB terms by multiplying them by the Fresnel reflection coefficient for the initial external reflection from the corresponding wedge face. The final step is related to the principle of reciprocity. The solution, as presented thus far, does not satisfy reciprocity. This is true since the reflection coefficient depends on the angle of incidence,  $\theta^i$ , which changes when source and observer are interchanged. Thus, in [7], the  $R_{\perp}$  were calculated by replacing  $\theta^i$  with half the angle between the incident and scatter directions. The resulting formulation for the field diffracted from the edge of a dielectric wedge is

$$u^{dif} \sim u^{inc}(Q_E) D_h \frac{e^{-jk\rho}}{\sqrt{\rho}} \quad (3.13)$$

where  $u^{inc}(Q_E)$  is the field incident on the edge, and the diffraction coefficient,  $D_h$ , is written as

$$D_h = \frac{-e^{-j\pi/4}}{2n\sqrt{2\pi k}} \left\{ R_{\perp} \cot \left[ \frac{\pi + (\phi + \phi')}{2n} \right] F[kLa^+(\phi + \phi')] + R_{\perp} \cot \left[ \frac{\pi - (\phi + \phi')}{2n} \right] F[kLa^-(\phi + \phi')] \right\} . \quad (3.14)$$

The reflection coefficients,  $R_{\perp}$ , are given by Equations (3.1) and (3.3), respectively. There is no distinction between the reflection coefficient for the  $o$  and  $n$  face terms, since the convention used for the angle of incidence depends only on the incident and scattered directions.

The following plots compare the UTD calculations of [7] with the solution of Rawlins for bistatic scattering from a two-dimensional dielectric wedge. The electric field vector of the incident field is parallel to the edge, the scattered field is computed at a distance of 50 wavelengths from the edge, and the relative permittivity of the wedge is equal to 1.1. This value of  $\epsilon_r$  is chosen because Rawlins' solution is more accurate for  $\epsilon_r$  close to one. The three figures correspond to three incident directions, as indicated. Overall, the agreement between the two solutions is very good. They differ most significantly along the wedge faces. Here, one would expect Rawlins' solution to be more accurate since it uses the correct boundary conditions. On the other hand, the modified UTD solution may be less accurate near the wedge faces since the presence of surface waves was not considered. (Note that later, when this method is extended to pyramidal absorber scattering, the incident and scatter directions never lie along a pyramidal face.)

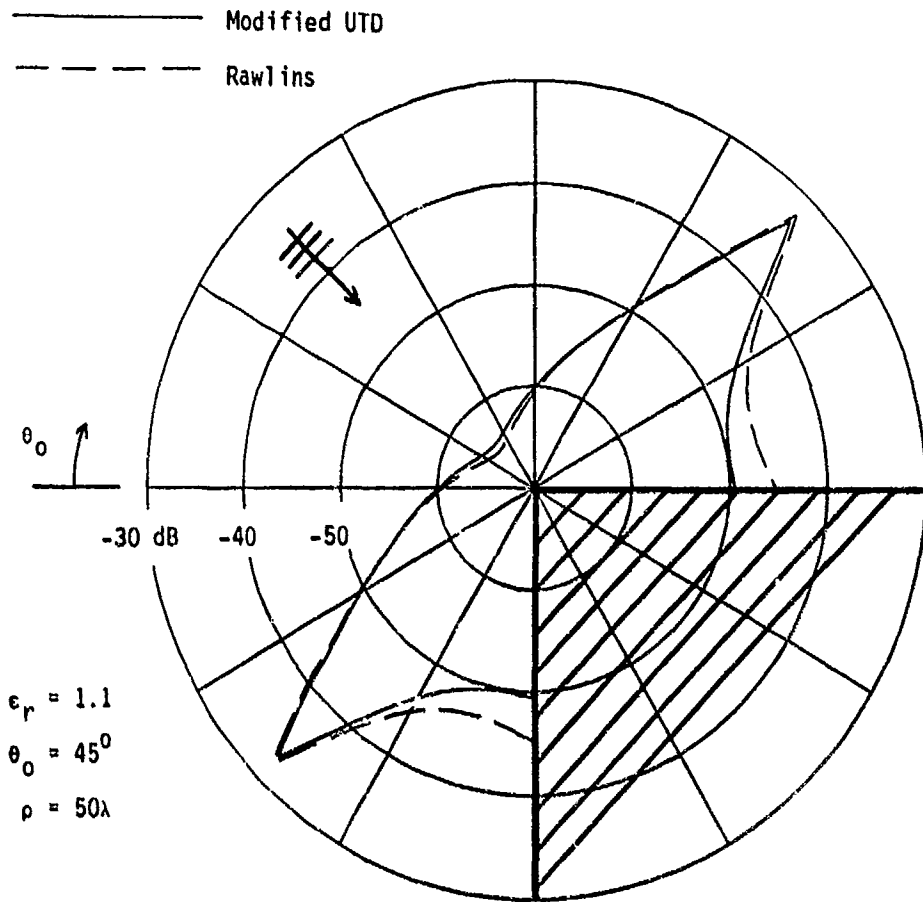


Figure 18: Bistatic scattering from a right angle dielectric wedge, modified UTD vs Rawlins' solution ( $\theta_0 = 45^\circ$ ).

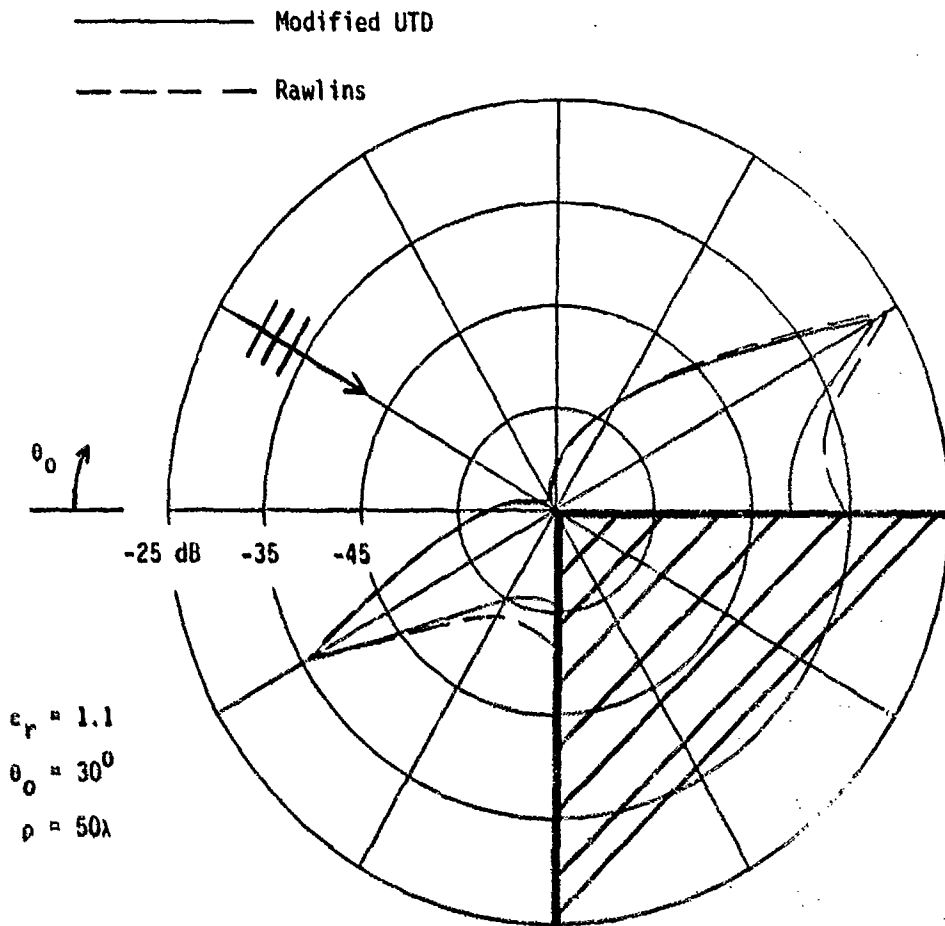


Figure 19: Bistatic scattering from a right angle dielectric wedge, modified UTD vs Rawlins' solution ( $\theta_o = 30^\circ$ ).

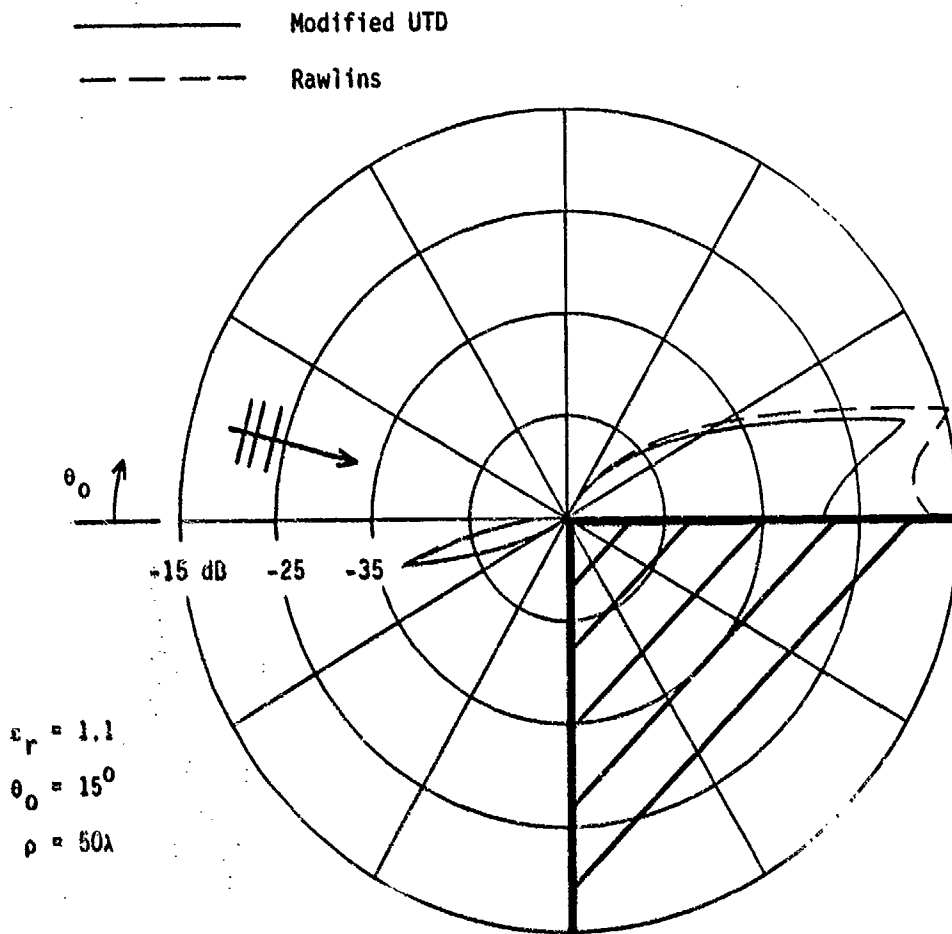


Figure 20: Bistatic scattering from a right angle dielectric wedge, modified UTD vs Rawlins' solution ( $\theta_0 = 15^\circ$ ).

One should keep in mind that a good engineering approximation is being sought for a very complex problem. The method proposed in [7] has proven to work very well for the cases in which there is available a method to compare against. This modified UTD approach will serve as the basis for the work in the remainder of this study.

### 3.5 Three-Dimensional Dielectric Wedge

In this section, the dielectric modification to the UTD solution proposed in [7] for a two-dimensional wedge will be extended to the problem of an infinite dielectric wedge in three-dimensional space. The edge diffracted field of a perfectly-conducting three-dimensional wedge, as depicted in Figure 4, may be written as

$$\mathbf{E}^d(s) \sim [AD(\phi - \phi') + BD(\phi + \phi')] \cdot \mathbf{E}^i(Q_E) \sqrt{\frac{\rho}{s(\rho + s)}} e^{-jks} \quad (3.15)$$

where

$$D(\phi \pm \phi') = \frac{-e^{-j\pi/4}}{2n\sqrt{2\pi k \sin \beta_o}} \left\{ \cot \left[ \frac{\pi + (\phi \pm \phi')}{2n} \right] F[kLa^+(\phi \pm \phi')] \right. \\ \left. + \cot \left[ \frac{\pi - (\phi \pm \phi')}{2n} \right] F[kLa^-(\phi \pm \phi')] \right\} \quad (3.16)$$

and the dyadic coefficients  $A$  and  $B$  are given by

$$A = -\hat{\beta}_o \hat{\beta}'_o - \hat{\phi} \hat{\phi}' \quad (3.17)$$

$$B = \hat{\beta}_o \hat{\beta}'_o - \hat{\phi} \hat{\phi}' \quad (3.18)$$

This may be expressed in matrix notation as

$$\begin{bmatrix} E_{\beta_o}^d(s) \\ E_{\phi}^d(s) \end{bmatrix} = [AD(\phi - \phi') + BD(\phi + \phi')] \begin{bmatrix} E_{\beta_o}^i(Q_E) \\ E_{\phi}^i(Q_E) \end{bmatrix} \sqrt{\frac{\rho}{s(\rho + s)}} e^{-jks} \quad (3.19)$$

where  $A$  and  $B$  are matrices given by

$$A = \begin{bmatrix} -1 & 0 \\ 0 & -1 \end{bmatrix} \quad (3.20)$$

$$B = \begin{bmatrix} 1 & 0 \\ 0 & -1 \end{bmatrix} . \quad (3.21)$$

The goal here is to determine the dyadic coefficients  $A$  and  $B$  that will properly scale the  $D(\phi \mp \phi')$  terms when the wedge is dielectric. The approach is again similar to that of [6] for the two-dimensional dielectric slab. For the moment, assume that  $R_{\perp}$  and  $T_{\perp}$  represent total reflection and transmission coefficients for the dielectric wedge, respectively. The discontinuities at the reflection shadow boundaries will now be investigated to determine the coefficient  $B$ . The question of field polarizations must be taken into consideration. Recall that the field reflected from a planar interface is most conveniently written in terms of its ray-fixed components  $\hat{u}_{\perp}$ ,  $\hat{u}_{\parallel}^i$ , as was done in Equation (3.5). On the other hand, the diffracted field formulation deals with the  $\hat{\beta}'_o$ ,  $\hat{\phi}'$  components of the incident field, and the  $\hat{\beta}_o$ ,  $\hat{\phi}$  components of the diffracted field. To find the discontinuities in the reflected field relative to these field polarizations, consider an incident ray reflecting off a (planar) wedge face. The point of reflection is infinitesimally close to the edge, so that the reflected ray is virtually along the RSB, on the lit side (as shown in Figure 21). The ordinary plane of incidence and edge-fixed planes of incidence and reflection are indicated in Figure 22. Define  $\alpha$  to be the angle between the ordinary plane of incidence and the edge-fixed plane of incidence. One can then take the incident field expressed in its  $\hat{\beta}'_o$ ,  $\hat{\phi}'$  components, transform them into  $\hat{u}_{\perp}$ ,  $\hat{u}_{\parallel}^i$  components, use Equation (3.5) to find the reflected field in its  $\hat{u}_{\perp}$ ,  $\hat{u}_{\parallel}^r$  components, and then transform this reflected field into its  $\hat{\beta}_o$ ,  $\hat{\phi}$  components. Doing so,

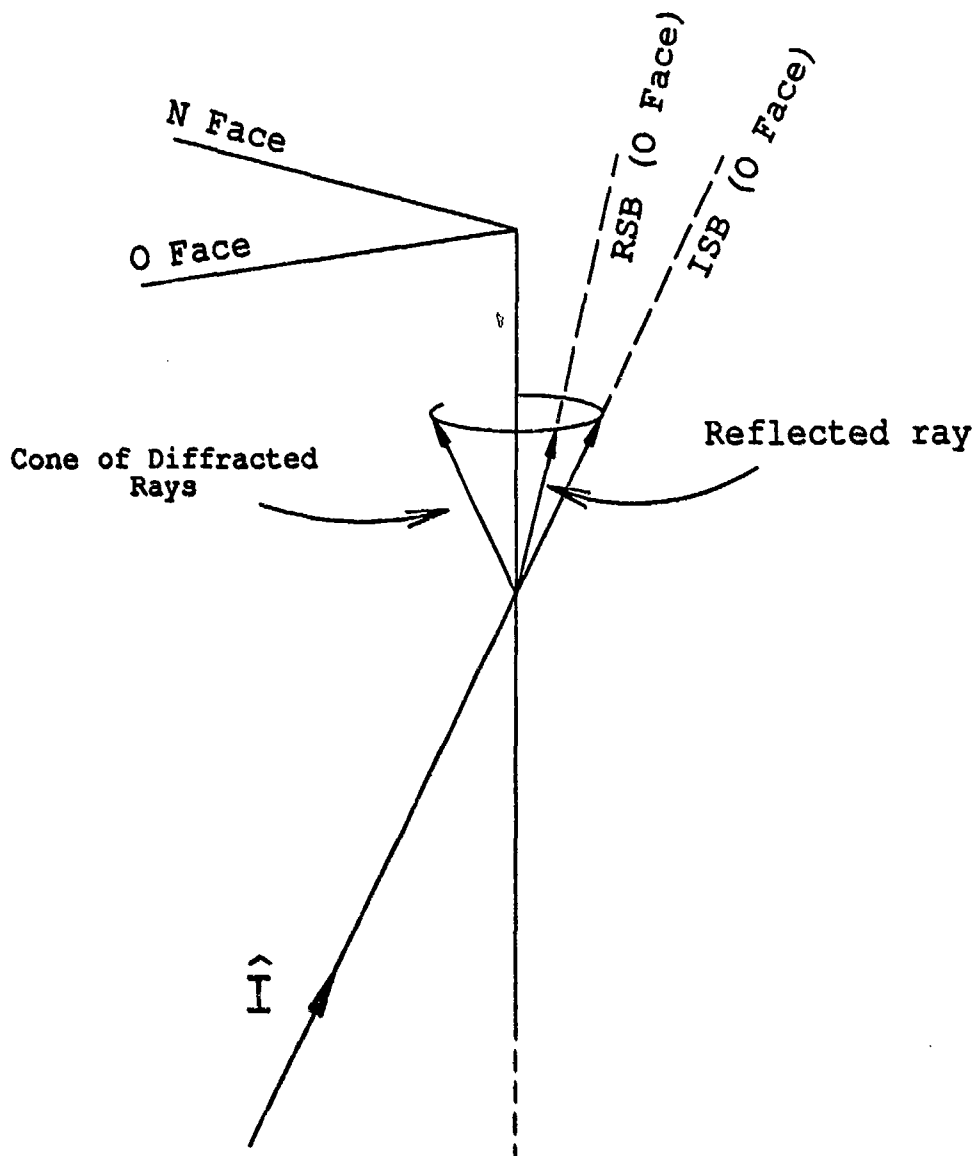


Figure 21: Reflection and diffraction at a three-dimensional dielectric wedge.

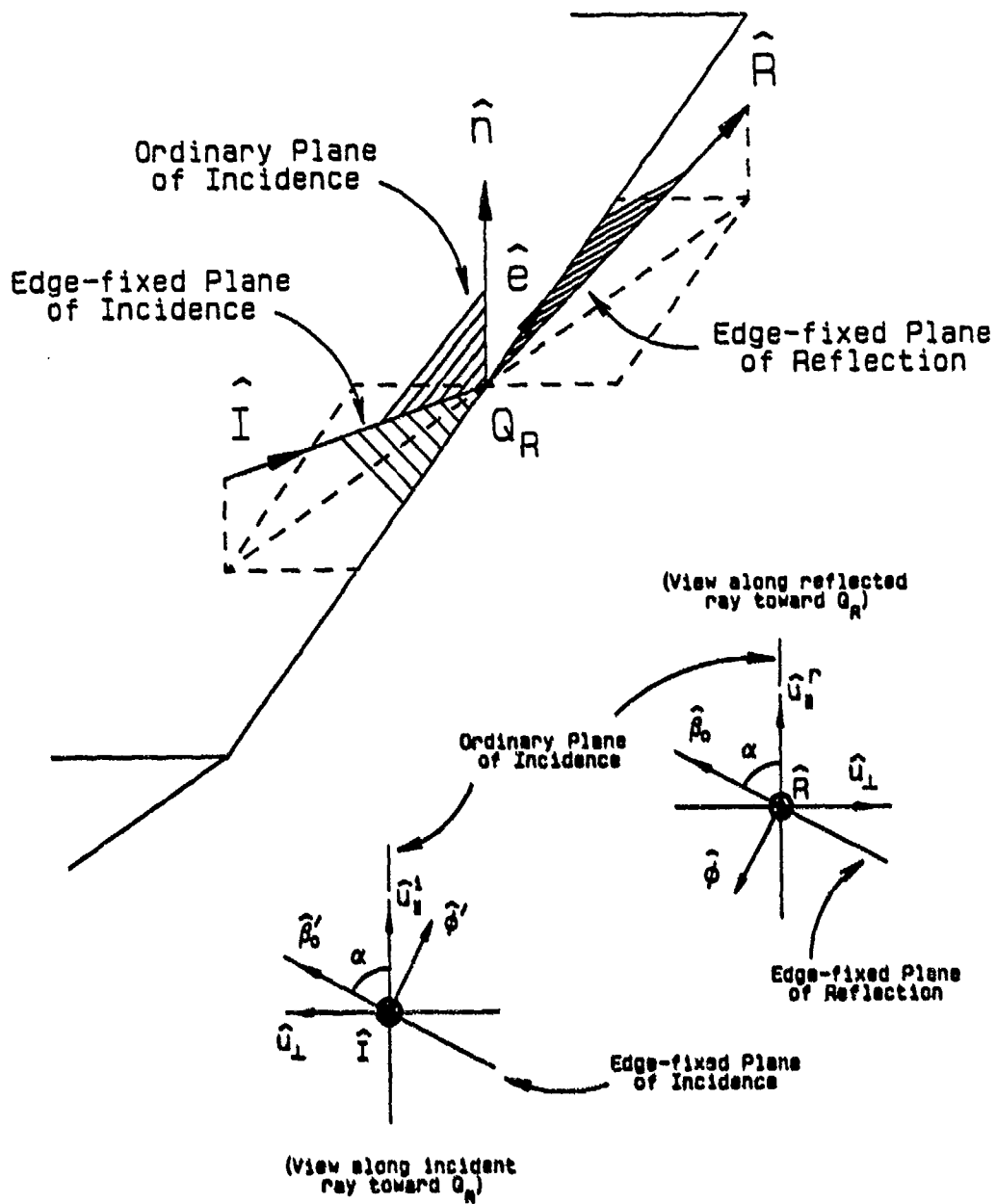


Figure 22: Pertinent field polarizations for reflection near wedge edge.

one finds that the reflected field  $\mathbf{E}^r(s)$  can be written as

$$\begin{bmatrix} E_{\beta_o}^r(s) \\ E_{\phi}^r(s) \end{bmatrix} = \begin{bmatrix} R_{\parallel} \cos^2 \alpha - R_{\perp} \sin^2 \alpha & (R_{\parallel} + R_{\perp}) \sin \alpha \cos \alpha \\ -(R_{\parallel} + R_{\perp}) \sin \alpha \cos \alpha & -R_{\parallel} \sin^2 \alpha + R_{\perp} \cos^2 \alpha \end{bmatrix} \quad (3.22)$$

$$\times \begin{bmatrix} E_{\beta_o}^i(Q_R) \\ E_{\phi}^i(Q_R) \end{bmatrix} e^{-jks}$$

where  $\mathbf{E}^i(Q_R)$  is the field incident at the reflection point  $Q_R$ , and  $s$  is the distance along the reflected ray from  $Q_R$ . This result is valid for any incident direction which illuminates the wedge face. Since the reflected field is zero on the dark side of the RSB, the  $2 \times 2$  matrix in Equation (3.22) represents the discontinuities associated with the RSB of the wedge face being considered. Thus, the scaling coefficient for the  $D(\phi + \phi')$  term of the diffracted field is written in matrix form as

$$B = \begin{bmatrix} R_{\parallel} \cos^2 \alpha - R_{\perp} \sin^2 \alpha & (R_{\parallel} + R_{\perp}) \sin \alpha \cos \alpha \\ -(R_{\parallel} + R_{\perp}) \sin \alpha \cos \alpha & -R_{\parallel} \sin^2 \alpha + R_{\perp} \cos^2 \alpha \end{bmatrix}_o^n \quad (3.23)$$

where the subscript indicates that the values vary with the  $o$  and  $n$  faces. The angle  $\alpha$  depends on the  $o$  and  $n$  faces because the two faces have different normal vectors and thus different ordinary planes of incidence. Note that the scaling for the  $o(n)$  face term is found when the  $o(n)$  face is illuminated, but will be used for all incident directions (regardless of whether or not the  $o(n)$  face is illuminated). This is of no concern. The same was done in the canonical problem of the two-dimensional perfectly-conducting wedge, where the reflection coefficients are  $\pm 1$ . When a certain boundary does not exist, the corresponding term in the diffraction formulation is typically negligible.

Following a similar approach, the discontinuity in the incident shadow boundary (ISB) terms is found to be the difference between the field on the lit side (the

incident field) and the field on the shadow side (the transmitted field), which is expressed as

$$\begin{bmatrix} E_{\beta_o}^i(s) \\ E_{\phi}^i(s) \end{bmatrix}_{Lit} - \begin{bmatrix} E_{\beta_o}^t(s) \\ E_{\phi}^t(s) \end{bmatrix}_{Shadow} = \begin{bmatrix} -1 + T_{||} \cos^2 \alpha + T_{\perp} \sin^2 \alpha & (T_{||} - T_{\perp}) \sin \alpha \cos \alpha \\ (T_{||} - T_{\perp}) \sin \alpha \cos \alpha & -1 + T_{||} \sin^2 \alpha + T_{\perp} \cos^2 \alpha \end{bmatrix} \begin{bmatrix} E_{\beta_o}^i(Q_E) \\ E_{\phi}^i(Q_E) \end{bmatrix} e^{-jks} \quad (3.24)$$

where  $E^i(Q_E)$  is the field incident at  $Q_E$  and  $s$  is the distance from  $Q_E$  to the field point. Thus, the scaling coefficient for the  $D(\phi - \phi')$  term of the diffracted field is written in matrix form as

$$A = \begin{bmatrix} -1 + T_{||} \cos^2 \alpha + T_{\perp} \sin^2 \alpha & (T_{||} - T_{\perp}) \sin \alpha \cos \alpha \\ (T_{||} - T_{\perp}) \sin \alpha \cos \alpha & -1 + T_{||} \sin^2 \alpha + T_{\perp} \cos^2 \alpha \end{bmatrix}_o \quad (3.25)$$

where the subscript again indicates that the values vary with the  $o$  and  $n$  faces. This procedure was first used in [6] for the problem of a slab in three-dimensional space.

Using these results, and rearranging Equation (3.19) somewhat, the edge diffracted field of a three-dimensional dielectric wedge can be written as

$$\begin{bmatrix} E_{\beta_o}^d(s) \\ E_{\phi}^d(s) \end{bmatrix} \sim \begin{bmatrix} D_a & D_b \\ D_c & D_d \end{bmatrix} \begin{bmatrix} E_{\beta_o}^i(Q_E) \\ E_{\phi}^i(Q_E) \end{bmatrix} \sqrt{\frac{\rho}{s(\rho + s)}} e^{-jks} \quad (3.26)$$

where

$$\begin{aligned} D_a &= (R_{||} \cos^2 \alpha - R_{\perp} \sin^2 \alpha)_n D_n(\phi + \phi') \\ &+ (R_{||} \cos^2 \alpha - R_{\perp} \sin^2 \alpha)_o D_o(\phi + \phi') \\ &+ (-1 + T_{||} \cos^2 \alpha + T_{\perp} \sin^2 \alpha)_n D_n(\phi - \phi') \\ &+ (-1 + T_{||} \cos^2 \alpha + T_{\perp} \sin^2 \alpha)_o D_o(\phi - \phi') \end{aligned} \quad (3.27)$$

$$D_b = [(R_{\parallel} + R_{\perp}) \sin \alpha \cos \alpha]_n D_n(\phi + \phi') \quad (3.28)$$

$$+ [(R_{\parallel} + R_{\perp}) \sin \alpha \cos \alpha]_o D_o(\phi + \phi')$$

$$+ [(T_{\parallel} - T_{\perp}) \sin \alpha \cos \alpha]_n D_n(\phi - \phi')$$

$$+ [(T_{\parallel} - T_{\perp}) \sin \alpha \cos \alpha]_o D_o(\phi - \phi')$$

$$D_c = - [(R_{\parallel} + R_{\perp}) \sin \alpha \cos \alpha]_n D_n(\phi + \phi') \quad (3.29)$$

$$- [(R_{\parallel} + R_{\perp}) \sin \alpha \cos \alpha]_o D_o(\phi + \phi')$$

$$+ [(T_{\parallel} - T_{\perp}) \sin \alpha \cos \alpha]_n D_n(\phi - \phi')$$

$$+ [(T_{\parallel} - T_{\perp}) \sin \alpha \cos \alpha]_o D_o(\phi - \phi')$$

$$D_d = (R_{\perp} \cos^2 \alpha - R_{\parallel} \sin^2 \alpha)_n D_n(\phi + \phi') \quad (3.30)$$

$$+ (R_{\perp} \cos^2 \alpha - R_{\parallel} \sin^2 \alpha)_o D_o(\phi + \phi')$$

$$+ (-1 + T_{\parallel} \sin^2 \alpha + T_{\perp} \cos^2 \alpha)_n D_n(\phi - \phi')$$

$$+ (-1 + T_{\parallel} \sin^2 \alpha + T_{\perp} \cos^2 \alpha)_o D_o(\phi - \phi')$$

and

$$D_o(\beta) = \frac{-e^{-j\pi/4}}{2n\sqrt{2\pi k} \sin \beta_o} \cot \left[ \frac{\pi \mp \beta}{2n} \right] F [kLa^{\mp}(\beta)] \quad (3.31)$$

Note that the parallel and perpendicular components of the incident and diffracted field are cross-coupled. This is due to the dielectric nature of the wedge; this cross-coupling does not exist for a perfectly-conducting wedge.

The preceding formulation is included for the sake of completeness; it aids in visualizing the overall effect of the dielectric (more than the specialized form of this solution that follows). Recall that  $R_{\perp}$  and  $T_{\perp}$  have as yet not been defined. Since reflection is a local phenomenon at high frequencies, plane wave incidence is assumed and Fresnel coefficients are used. The final step here will be to use the dielectric modification of [7] discussed in the previous section. Thus,  $R_{\perp}$  will consider only the initial external reflections off the wedge faces. Also, recall that

the usual angle of incidence is replaced by half the angle between incident and scattered directions in the computation of these reflection coefficients. Therefore the distinction between the  $o$  and  $n$  faces for  $R_{\perp}$  no longer exists. (However, the distinction between the  $o$  and  $n$  faces for  $\alpha$  remains.) The  $T_{\perp}$  are set to unity, which is equivalent to considering the ISB terms negligible. With these conventions, the edge diffracted fields of a three-dimensional dielectric wedge are given by

$$\begin{bmatrix} E_{\beta_o}^d(s) \\ E_{\phi}^d(s) \end{bmatrix} \sim \begin{bmatrix} D_a & D_b \\ D_c & D_d \end{bmatrix} \begin{bmatrix} E_{\beta_o}^i(QE) \\ E_{\phi}^i(QE) \end{bmatrix} \sqrt{\frac{\rho}{s(\rho+s)}} e^{-jks} \quad (3.32)$$

where

$$\begin{aligned} D_a = & (R_{\parallel} \cos^2 \alpha_n - R_{\perp} \sin^2 \alpha_n) D_n(\phi + \phi') \\ & + (R_{\parallel} \cos^2 \alpha_o - R_{\perp} \sin^2 \alpha_o) D_o(\phi + \phi') \end{aligned} \quad (3.33)$$

$$\begin{aligned} D_b = & (R_{\parallel} + R_{\perp}) \sin \alpha_n \cos \alpha_n D_n(\phi + \phi') \\ & + (R_{\parallel} + R_{\perp}) \sin \alpha_o \cos \alpha_o D_o(\phi + \phi') \end{aligned} \quad (3.34)$$

$$\begin{aligned} D_c = & - (R_{\parallel} + R_{\perp}) \sin \alpha_n \cos \alpha_n D_n(\phi + \phi') \\ & - (R_{\parallel} + R_{\perp}) \sin \alpha_o \cos \alpha_o D_o(\phi + \phi') \end{aligned} \quad (3.35)$$

$$\begin{aligned} D_d = & (R_{\perp} \cos^2 \alpha_n - R_{\parallel} \sin^2 \alpha_n) D_n(\phi + \phi') \\ & + (R_{\perp} \cos^2 \alpha_o - R_{\parallel} \sin^2 \alpha_o) D_o(\phi + \phi') \end{aligned} \quad (3.36)$$

and  $D_n(\phi + \phi')$  is given by Equation (3.31).

### 3.6 Dielectric Corner Diffraction

At this point, the extension to dielectric corner diffraction follows almost intuitively. The corner diffraction solution for the perfectly conducting three-dimensional wedge, presented in Section 2.4, is modified here just as the edge diffraction formulation was modified in the previous section. Again, the dielectric

conventions of [7] are used. The corner diffracted fields associated with one corner and one edge of a finite three-dimensional dielectric wedge in the near field with spherical wave incidence are given by

$$\begin{bmatrix} E_{\beta_{oc}}^c(s) \\ E_{\phi}^c(s) \end{bmatrix} \sim \begin{bmatrix} C_a(Q_E) & C_b(Q_E) \\ C_c(Q_E) & C_d(Q_E) \end{bmatrix} \begin{bmatrix} E_{\beta_c}^i(Q_C) \\ E_{\phi'}^i(Q_C) \end{bmatrix} \frac{e^{-j\pi/4}}{\sqrt{2\pi k}} \times \quad (3.37)$$

$$\frac{\sqrt{\sin \beta_c \sin \beta_{oc}}}{(\cos \beta_{oc} - \cos \beta_c)} F[kL_c a(\pi + \beta_{oc} - \beta_c)] \frac{e^{-jks}}{s}$$

where

$$C_a(Q_E) = (R_{||} \cos^2 \alpha_n - R_{\perp} \sin^2 \alpha_n) C_n(\phi + \phi') + (R_{||} \cos^2 \alpha_o - R_{\perp} \sin^2 \alpha_o) C_o(\phi + \phi') \quad (3.38)$$

$$C_b(Q_E) = (R_{||} + R_{\perp}) \sin \alpha_n \cos \alpha_n C_n(\phi + \phi') + (R_{||} + R_{\perp}) \sin \alpha_o \cos \alpha_o C_o(\phi + \phi') \quad (3.39)$$

$$C_c(Q_E) = - (R_{||} + R_{\perp}) \sin \alpha_n \cos \alpha_n C_n(\phi + \phi') - (R_{||} + R_{\perp}) \sin \alpha_o \cos \alpha_o C_o(\phi + \phi') \quad (3.40)$$

$$C_d(Q_E) = (R_{\perp} \cos^2 \alpha_n - R_{||} \sin^2 \alpha_n) C_n(\phi + \phi') + (R_{\perp} \cos^2 \alpha_o - R_{||} \sin^2 \alpha_o) C_o(\phi + \phi') \quad (3.41)$$

and

$$C_n(\beta) = \frac{-e^{-j\pi/4}}{2n\sqrt{2\pi k \sin \beta_o}} \times \quad (3.42)$$

$$\cot\left(\frac{\pi \mp(\beta)}{2n}\right) F[kLa^{\mp}(\beta)] \left| F\left[\frac{La^{\mp}(\beta)/\lambda}{kL_c a(\pi + \beta_{oc} - \beta_c)}\right] \right|$$

This form will be used to calculate the bistatic scattering from the tip of an absorber pyramid. It is applied four times, once for each of the four edges associated with the tip. The modeling of the pyramid and specifics on how this calculation is performed are the subject of the next chapter.

## CHAPTER IV

### TIP DIFFRACTION FROM PYRAMIDAL ABSORBER

#### 4.1 Introduction

In this chapter, the modified UTD solution for dielectric corner diffraction will be applied to an absorber pyramid. The modeling of the pyramid is considered first, and the calculation of several variables in the solution is discussed. Results are then shown for various monostatic and bistatic geometries.

#### 4.2 Tip Diffraction Calculations

The pyramidal tip is treated as a corner in a three-dimensional wedge, which has four planar surfaces and four edges intersecting at a common point. Recall that the corner diffraction solution gives the fields associated with one corner and one edge; thus, it must be applied to the pyramidal tip four times.

To begin, consider the conventions illustrated in Figure 23. The tip of the pyramid is placed at the origin of a cartesian coordinate system. This will serve as the primary coordinate system; all coordinate systems introduced later will be defined in terms of this primary system. The pyramid is oriented so that a vector normal to face 1 or 3 would have no  $\hat{y}$  component, and a vector normal to face 2 or 4 would have no  $\hat{z}$  component. The pyramid's shape is characterized by a single angle,  $\alpha$ , which is that angle between any two adjacent edges. (Note that

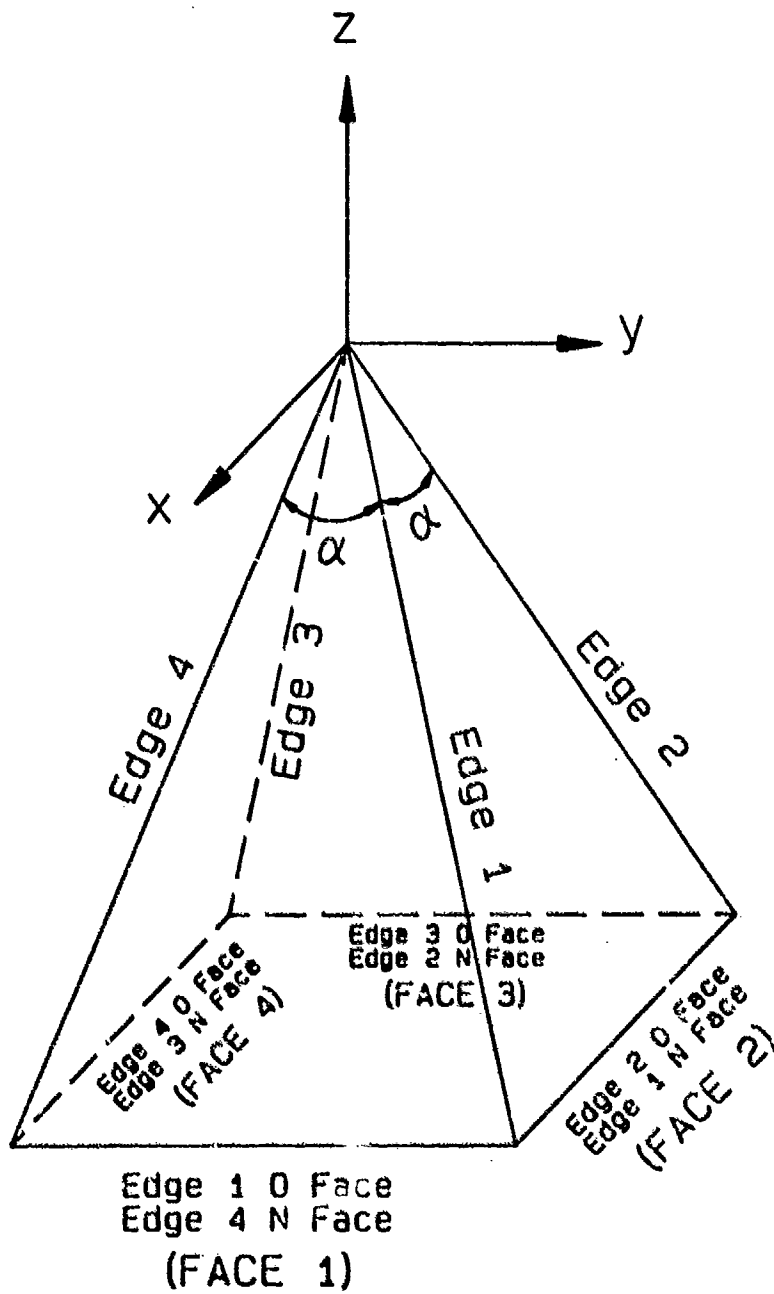


Figure 23: Conventions used for pyramid geometry.

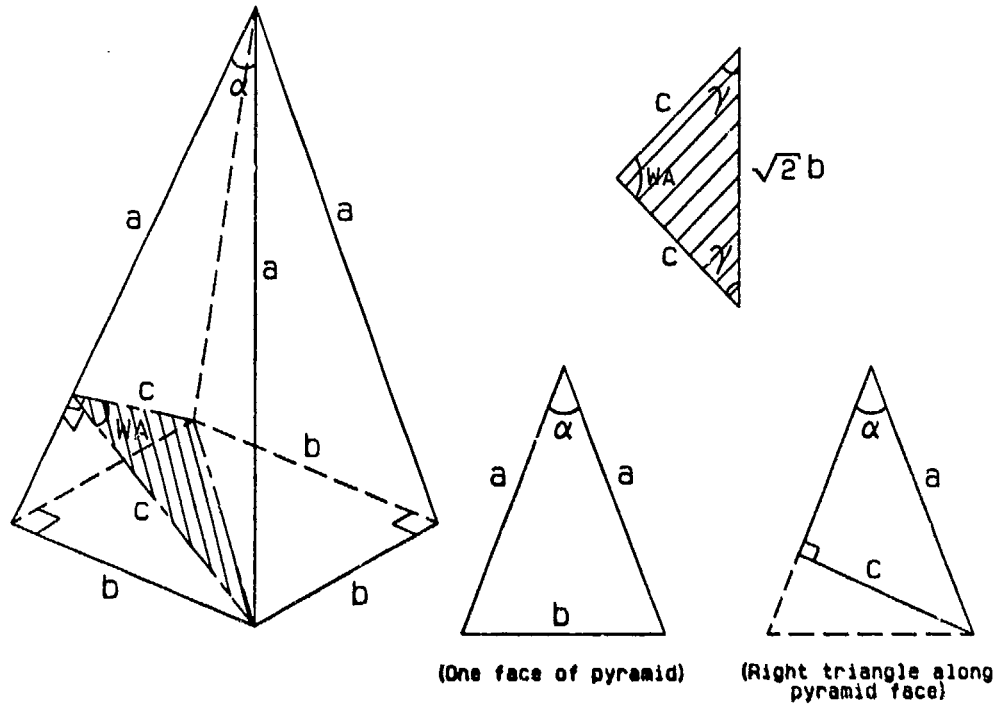


Figure 24: Determination of the pyramidal wedge angle, WA.

considering the tip contribution only is equivalent to the pyramid being of infinite extent.)

First, consider the wedge angle, WA, a variable that depends only on the geometry of the pyramid. This angle is most easily found by means of the triangle shown shaded in Figure 24. This triangle has two vertices at opposite corners of the pyramid base, while its third vertex lies along one edge of the pyramid. This third vertex is located such that the triangle sides adjacent to it are perpendicular to the pyramid edge, as shown. The wedge angle is the angle at this third vertex of the triangle, as indicated. Applying the law of cosines to one face of the pyramid yields

$$b = \sqrt{2a^2(1 - \cos \alpha)} \quad (4.1)$$

while the right triangle depicted along the pyramid face yields

$$c = a \sin \alpha \quad (4.2)$$

Applying next the law of sines to the shaded triangle yields

$$\frac{\sqrt{2}b}{\sin WA} = \frac{c}{\sin \gamma} \quad (4.3)$$

Substituting Equations (4.1), (4.2), and  $\sin \gamma = \cos(WA/2)$  into Equation (4.3) then yields

$$\frac{2a\sqrt{1 - \cos \alpha}}{\sin WA} = \frac{a \sin \alpha}{\cos(WA/2)} \quad (4.4)$$

Since  $\sin WA = 2 \sin(WA/2) \cos(WA/2)$ , one finds the wedge angle to be given by

$$WA = 2 \sin^{-1} \left( \frac{\sqrt{1 - \cos \alpha}}{\sin \alpha} \right) \quad (4.5)$$

This expression is of course valid for all four edges of the pyramid.

Next, an edge-fixed coordinate system is needed for each pyramid edge. The coordinate systems chosen are rectangular; each has an edge vector,  $\hat{e}$ , directed along the edge toward the pyramid tip, a normal vector,  $\hat{n}$ , normal to the  $o$  face of the corresponding edge, and a bi-normal vector,  $\hat{e}'$ , which lies along the  $o$  face and is defined by  $\hat{e}' = \hat{n} \times \hat{e}$ . The edge-fixed coordinate system for edge 1 is depicted in Figure 25. Note that a new angle,  $\beta$ , has been introduced, which is the angle formed by opposite edges of the pyramid; it will be useful in determining the edge-fixed coordinate systems. Applying the law of cosines to each of the two triangles inset in Figure 25 and equating the results yields

$$\cos \beta = 2 \cos \alpha - 1 \quad (4.6)$$

Further manipulation reveals that

$$\cos(\beta/2) = \sqrt{\cos \alpha} \quad , \text{ and} \quad (4.7)$$

$$\sin(\beta/2) = \sqrt{2} \sin(\alpha/2) \quad (4.8)$$

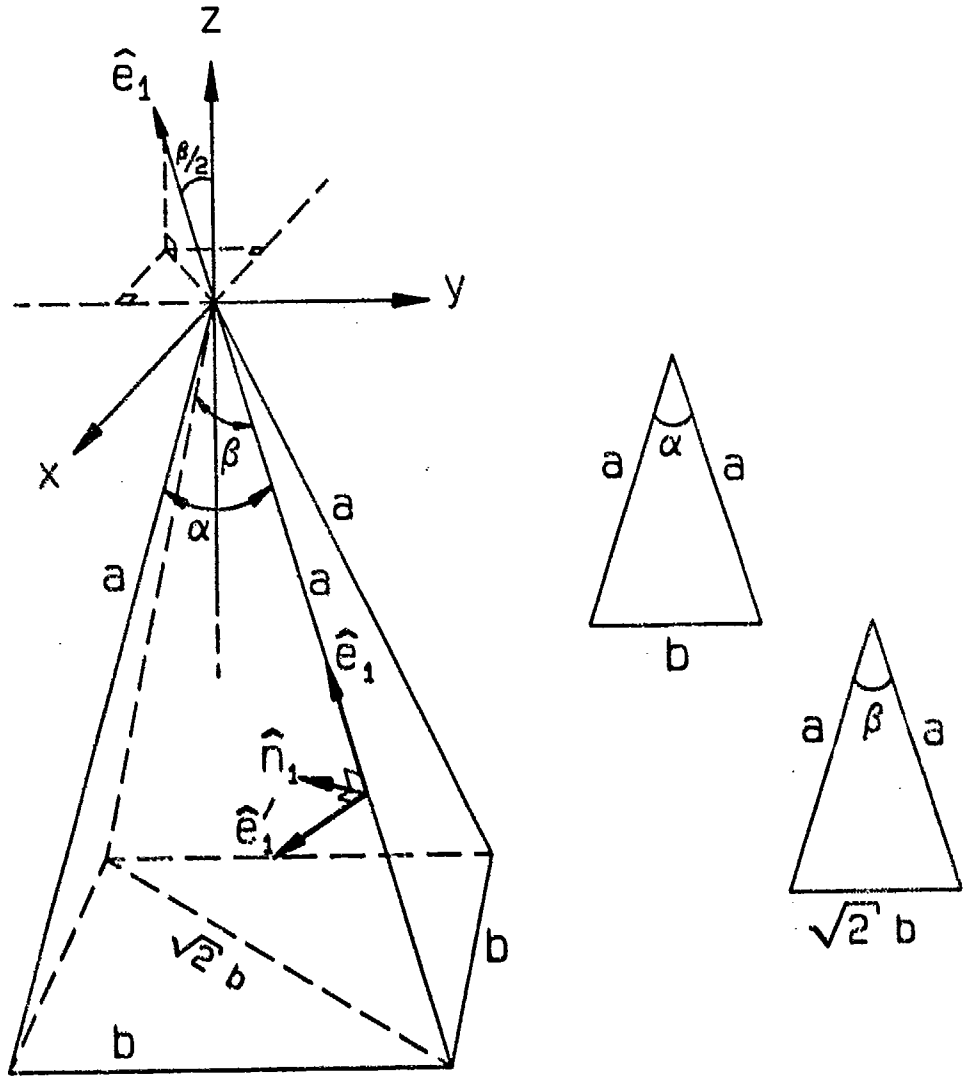


Figure 25: Edge-fixed coordinate system for pyramid edge 1.

It is then clear that

$$e_{1z} = \cos(\beta/2) = \sqrt{\cos \alpha} , \text{ and} \quad (4.9)$$

$$e_{1x} = e_{1y} = -\frac{1}{\sqrt{2}} \sin(\beta/2) = -\sin(\alpha/2) . \quad (4.10)$$

From the symmetry present, one can immediately see that the four edge vectors are given by

$$\hat{e}_1 = -\hat{x} \sin(\alpha/2) - \hat{y} \sin(\alpha/2) + \hat{z} \sqrt{\cos \alpha} \quad (4.11)$$

$$\hat{e}_2 = \hat{x} \sin(\alpha/2) - \hat{y} \sin(\alpha/2) + \hat{z} \sqrt{\cos \alpha} \quad (4.12)$$

$$\hat{e}_3 = \hat{x} \sin(\alpha/2) + \hat{y} \sin(\alpha/2) + \hat{z} \sqrt{\cos \alpha} , \text{ and} \quad (4.13)$$

$$\hat{e}_4 = -\hat{x} \sin(\alpha/2) + \hat{y} \sin(\alpha/2) + \hat{z} \sqrt{\cos \alpha} . \quad (4.14)$$

Now, let us consider the normal vectors. Since  $\hat{n}_1$  is orthogonal to  $\hat{e}_1$  and to the  $o$  face of edge 1, it may be found as

$$\hat{n}_1 = \frac{\hat{y} \times \hat{e}_1}{|\hat{y} \times \hat{e}_1|} = \hat{x}A + \hat{z}B \quad (4.15)$$

where this computation is performed numerically. Note that  $A, B > 0$ . The remaining normal vectors, due to the symmetry involved, are given in terms of  $A$  and  $B$  as

$$\hat{n}_2 = \hat{y}A + \hat{z}B \quad (4.16)$$

$$\hat{n}_3 = -\hat{x}A + \hat{z}B , \text{ and} \quad (4.17)$$

$$\hat{n}_4 = -\hat{y}A + \hat{z}B . \quad (4.18)$$

Finally, consider the bi-normal vectors. The first is written as

$$\hat{e}'_1 = \hat{n}_1 \times \hat{e}_1 = \hat{x}C - \hat{y}D - \hat{z}E \quad (4.19)$$

where  $C$ ,  $D$ , and  $E$  are also found numerically. Note that  $C, D, E > 0$ . Again, from the symmetry present, the remaining bi-normal vectors may be written as

$$\hat{e}'_2 = \hat{x}D + \hat{y}C - \hat{z}E \quad (4.20)$$

$$\hat{e}'_3 = -\hat{x}C + \hat{y}D - \hat{z}E, \text{ and} \quad (4.21)$$

$$\hat{e}'_4 = -\hat{x}D - \hat{y}C - \hat{z}E. \quad (4.22)$$

These edge-fixed coordinate systems will be used later to determine various angles and unit vectors.

Next, consider the illumination of the pyramid by a spherical wave emanating from a source point,  $S$ . Figure 26 illustrates the dielectric corner diffraction geometry associated with the tip and one edge of the pyramid. The source and observation points are in the far zone of the tip. Thus the field incident at the tip is approximately planar. Note that source and observer are assumed to recede into the far zone at an equal rate; that is, they are equidistant from the tip. Thus, while the location of  $Q_E$  is not known, there is no ambiguity in the value of  $\beta'_0$ . The computation of  $\beta'_0$  will be described shortly. Assume that the incident electric field is known in terms of its  $\hat{\theta}^i$ ,  $\hat{\phi}^i$  components and its incidence angles  $\theta^i$ ,  $\phi^i$ ; as shown in Figure 27. The aim is to find the scattered field in a direction specified by the scattering angles  $\theta^s$ ,  $\phi^s$ . The  $\hat{x}$ ,  $\hat{y}$ , and  $\hat{z}$  components of  $\mathbf{E}^i$  are found by a simple transformation, while  $\hat{I}$  and  $\hat{D}$  are given by

$$\hat{I} = -\hat{x} \sin \theta^i \cos \phi^i - \hat{y} \sin \theta^i \sin \phi^i - \hat{z} \cos \theta^i, \text{ and} \quad (4.23)$$

$$\hat{D} = \hat{x} \sin \theta^s \cos \phi^s + \hat{y} \sin \theta^s \sin \phi^s + \hat{z} \cos \theta^s. \quad (4.24)$$

Note that the incident and scattered directions are assumed to be in the upper ( $z > 0$ ) half-space.



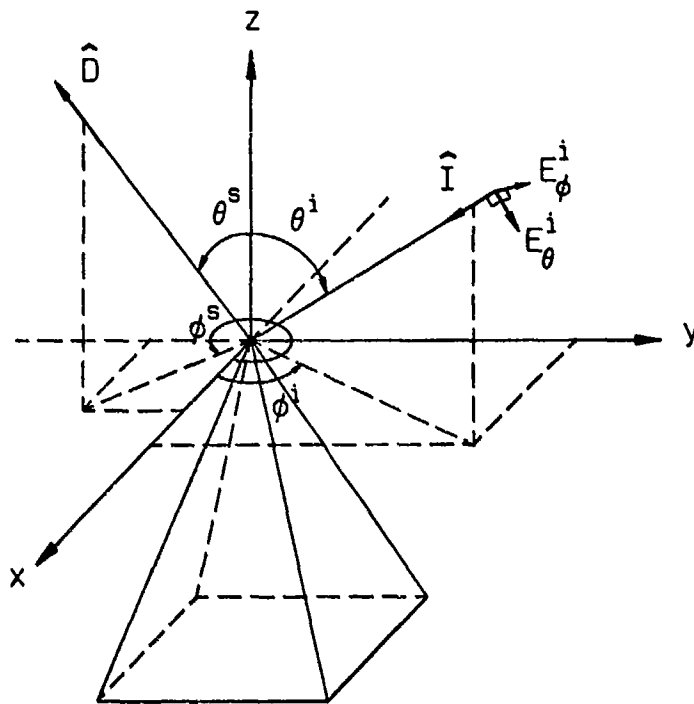


Figure 27: Geometry for incident and scattered fields of a pyramid tip.

To implement the corner diffraction solution, the angles  $\phi$  and  $\phi'$  must be found for each edge. Consider the unit vector  $\hat{I}$  directed toward a corner diffraction point,  $Q_C$ , as illustrated in Figure 28. From the lengths labeled, it is clear that  $\hat{I}$  is expressed in the edge-fixed coordinate system as

$$\hat{I} = -\hat{e}' \sin \beta_c \cos \phi' - \hat{n} \sin \beta_c \sin \phi' + \hat{e} \cos \beta_c . \quad (4.25)$$

In a similar manner, one would find that

$$\hat{D} = \hat{e}' \sin \beta_{oc} \cos \phi + \hat{n} \sin \beta_{oc} \sin \phi + \hat{e} \cos \beta_{oc} . \quad (4.26)$$

From the expression given for  $\hat{I}$ , one can see that the angle  $\phi'$  of the  $m^{\text{th}}$  edge is found as

$$\phi'_m = \tan^{-1} \left( \frac{-\hat{I} \cdot \hat{n}_m}{-\hat{I} \cdot \hat{e}'_m} \right) \quad (4.27)$$

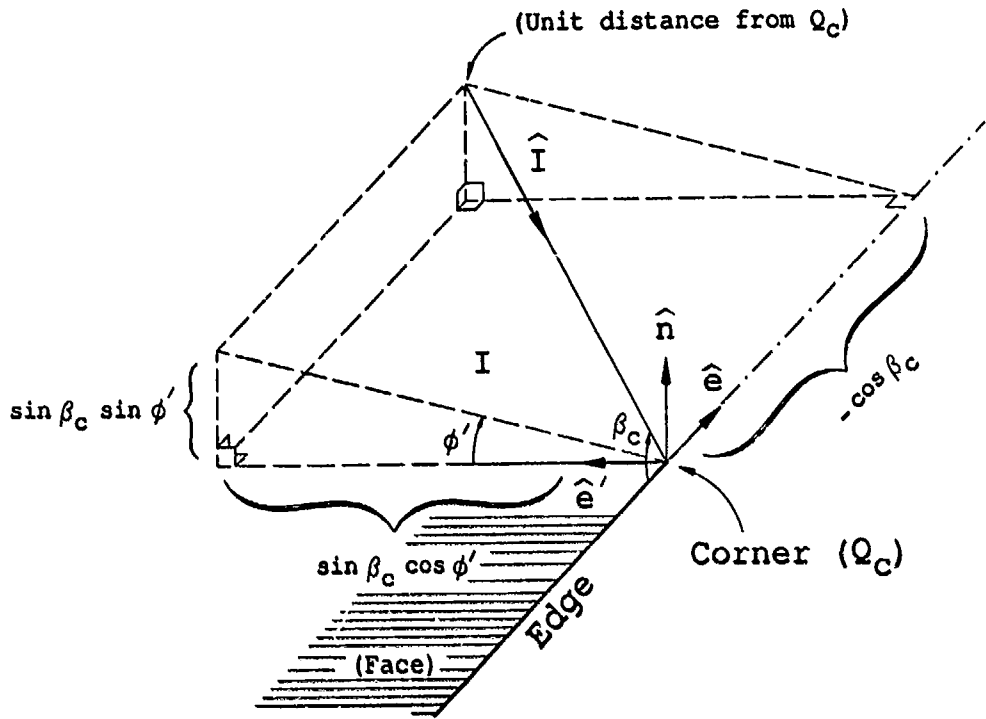


Figure 28: Determination of  $\phi$  and  $\phi'$  at an arbitrary edge.

while the expression given for  $\hat{D}$  is used to find  $\phi$  of the  $m^{\text{th}}$  edge as

$$\phi_m = \tan^{-1} \left( \frac{\hat{D} \cdot \hat{n}_m}{\hat{D} \cdot \hat{e}'_m} \right) . \quad (4.28)$$

Note that the minus signs in the numerator and denominator of Equation (4.27) are retained to allow a computer algorithm to return the angle  $\phi'$  in the proper quadrant. By definition,  $0 < \phi, \phi' < 2\pi$ . If  $\phi'_m$  or  $\phi_m$  is greater than  $\pi$ , then the diffracted fields associated with the  $m^{\text{th}}$  edge are ignored, since that edge is shadowed (the incident or scattered field direction is inside the extension of the wedge). Although regions of space do exist where there is no diffracted field contribution from some edge, there is no region of space that sees no contribution from any edge. For the case of backscatter, note that  $\phi_m = \phi'_m$ .

The reflection coefficients,  $R_{\perp}$  and  $R_{\parallel}$ , are found by Equations (3.1) and (3.3),

respectively. Recall that the incidence angle used in these calculations is half the angle between incident and scattered directions, and can be found by

$$\theta_{RC}^i = \frac{1}{2} \cos^{-1}(-\hat{I} \cdot \hat{D}) . \quad (4.29)$$

These reflection coefficients ( $R_{\perp}$  and  $R_{\parallel}$ ) apply to all four edges. For the backscatter case,  $\theta_{RC}^i = 0$ .

The unit vectors  $\hat{\phi}'$ ,  $\hat{\beta}_c$ ,  $\hat{\phi}$ , and  $\hat{\beta}_{oc}$ , which were defined in Section 2.4, can now be more conveniently defined (for the  $m^{\text{th}}$  edge) as

$$\hat{\phi}'_m = \hat{n}_m \cos \phi'_m - \hat{e}'_m \sin \phi'_m \quad (4.30)$$

$$\hat{\beta}_{c_m} = \hat{\phi}'_m \times \hat{I} \quad (4.31)$$

$$\hat{\phi}_m = \hat{n}_m \cos \phi_m - \hat{e}'_m \sin \phi_m , \text{ and} \quad (4.32)$$

$$\hat{\beta}_{oc_m} = \hat{\phi}_m \times \hat{D} . \quad (4.33)$$

The angles  $\beta_c$  and  $\beta_{oc}$  associated with the  $m^{\text{th}}$  edge are found as

$$\beta_{c_m} = \cos^{-1}(\hat{I} \cdot \hat{e}_m) , \text{ and} \quad (4.34)$$

$$\beta_{oc_m} = \cos^{-1}(\hat{D} \cdot \hat{e}_m) . \quad (4.35)$$

For backscatter,  $\beta_{oc_m} = \pi - \beta_{c_m}$ .

A good deal more effort is involved in finding the angle  $\beta'_o$ . Consider the geometry illustrated in Figure 29.  $\mathbf{R}_s$  and  $\mathbf{R}_o$  are vectors originating at the tip and terminating at the source and observation points, respectively. These vectors must be of equal length, although their actual length does not matter here. Thus one can choose  $\mathbf{R}_s = -\hat{I}$ , and  $\mathbf{R}_o = \hat{D}$ . Line segments are drawn from the source and observation points perpendicular to the edge extension; their lengths are labeled  $l_{s_m}$  and  $l_{o_m}$ , and the points at which they intersect the edge extension

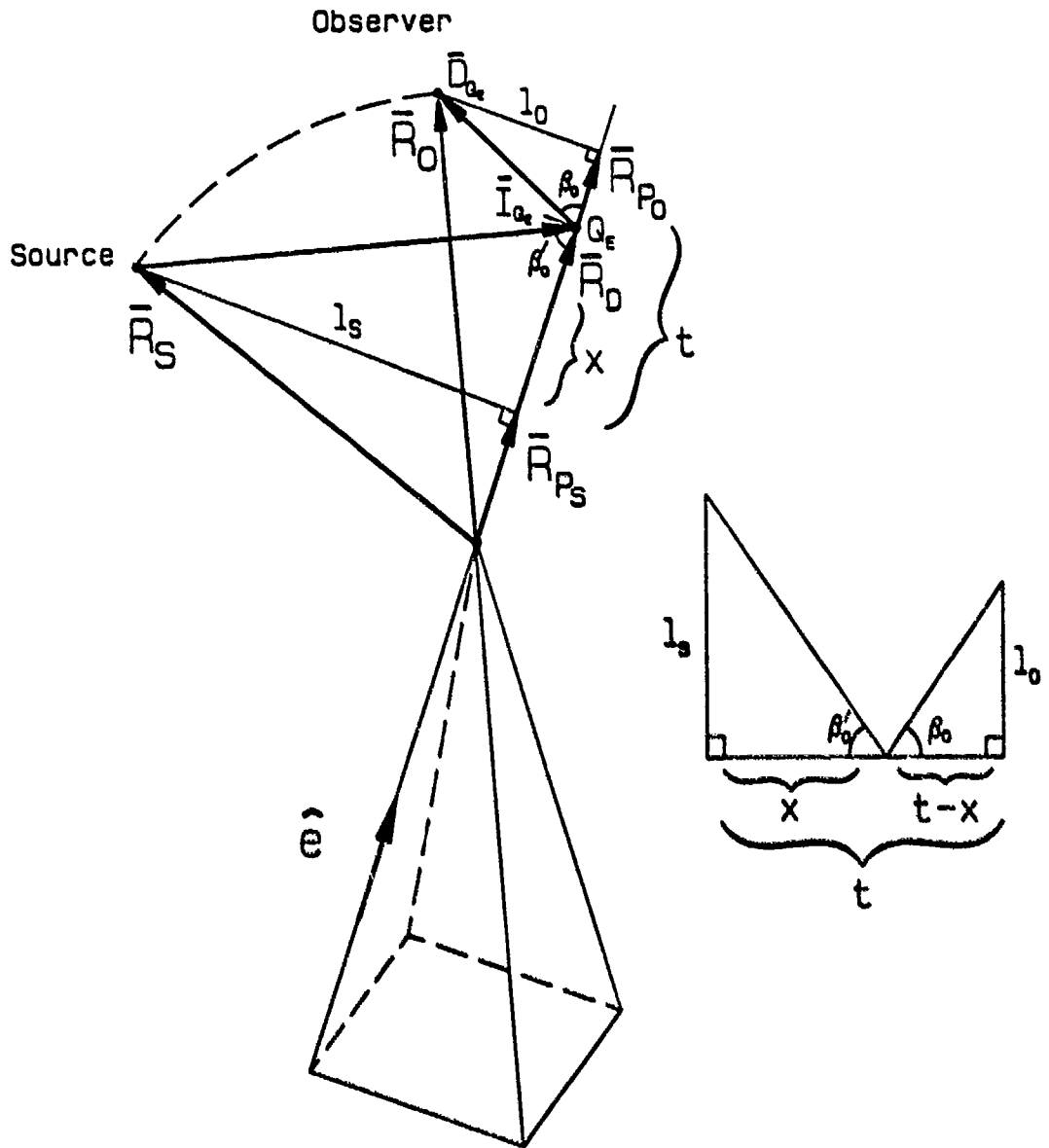


Figure 29: Determination of  $\beta'_0$  at an arbitrary edge.

are located by the vectors  $\mathbf{R}_{P_{sm}}$  and  $\mathbf{R}_{P_{om}}$ , respectively. The vectors  $\mathbf{R}_{P_{sm}}$  and  $\mathbf{R}_{P_{om}}$  can be found as

$$\mathbf{R}_{P_{sm}} = (\mathbf{R}_s \cdot \hat{e}_m) \hat{e}_m \quad (4.36)$$

$$\mathbf{R}_{P_{om}} = (\mathbf{R}_o \cdot \hat{e}_m) \hat{e}_m \quad (4.37)$$

while the distances  $l_{sm}$  and  $l_{om}$  can be found as

$$l_{sm} = |\mathbf{R}_s - \mathbf{R}_{P_{sm}}|, \text{ and} \quad (4.38)$$

$$l_{om} = |\mathbf{R}_o - \mathbf{R}_{P_{om}}|. \quad (4.39)$$

Now, consider the line segments drawn from the source and observation points to the edge diffraction point  $Q_{Em}$ . A pair of similar triangles exists, though not coplanar, as indicated in the inset of Figure 29. Since

$$\frac{x_m}{l_{sm}} = \frac{l_m - x_m}{l_{om}} \quad (4.40)$$

the distance  $x_m$  can be written as

$$x_m = \frac{l_{sm} l_m}{l_{sm} + l_{om}} \quad (4.41)$$

where

$$l_m = |\mathbf{R}_{P_{om}} - \mathbf{R}_{P_{sm}}| = (\mathbf{R}_o - \mathbf{R}_s) \cdot \hat{e}_m. \quad (4.42)$$

The vector  $\mathbf{R}_{D_m}$ , directed from the tip to the edge diffraction point, is then clearly given by

$$\mathbf{R}_{D_m} = \mathbf{R}_{P_{sm}} + x_m \hat{e}_m \quad (4.43)$$

and the unit vector  $\hat{i}_{Q_{Em}}$  is given by

$$\hat{i}_{Q_{Em}} = \frac{\mathbf{R}_{D_m} - \mathbf{R}_s}{|\mathbf{R}_{D_m} - \mathbf{R}_s|}. \quad (4.44)$$

With  $\hat{I}_{Q_{Em}}$  known,  $\beta'_o$  for the  $m^{\text{th}}$  edge can be found as

$$\beta'_{om} = \cos^{-1}(\hat{I}_{Q_{Em}} \cdot \hat{e}_m) \quad (4.45)$$

and, of course,  $\beta_{om} = \beta'_{om}$ . In the case of backscatter, this reduces simply to  $\beta_{om} = \beta'_{om} = \pi/2$ , for all edges.

Looking back to the dielectric corner diffraction solution presented in Section 3.6, one sees that the angle  $\alpha$  (the angle formed by the ordinary and edge-fixed planes of incidence, not to be confused with the angle  $\alpha$  of the pyramid) is used repeatedly in the definition of  $C_a(Q_E)$ ,  $C_b(Q_E)$ ,  $C_c(Q_E)$ , and  $C_d(Q_E)$ . This angle, although useful in visualizing the diffraction solution, will not be explicitly used in the computation of the corner diffracted fields. Rather, the  $C(Q_E)$  may be expressed as

$$C_a(Q_E) = [\psi_2^n \psi_4^n R_{\perp} + \psi_1^n \psi_3^n R_{\parallel}] C_n(\phi + \phi') + [\psi_2^o \psi_4^o R_{\perp} + \psi_1^o \psi_3^o R_{\parallel}] C_o(\phi + \phi') \quad (4.46)$$

$$C_b(Q_E) = [\psi_1^n \psi_4^n R_{\perp} - \psi_2^n \psi_3^n R_{\parallel}] C_n(\phi + \phi') + [\psi_1^o \psi_4^o R_{\perp} - \psi_2^o \psi_3^o R_{\parallel}] C_o(\phi + \phi') \quad (4.47)$$

$$C_c(Q_E) = [\psi_2^n \psi_3^n R_{\perp} - \psi_1^n \psi_4^n R_{\parallel}] C_n(\phi + \phi') + [\psi_2^o \psi_3^o R_{\perp} - \psi_1^o \psi_4^o R_{\parallel}] C_o(\phi + \phi') \quad (4.48)$$

and

$$C_d(Q_E) = [\psi_1^n \psi_3^n R_{\perp} + \psi_2^n \psi_4^n R_{\parallel}] C_n(\phi + \phi') + [\psi_1^o \psi_3^o R_{\perp} + \psi_2^o \psi_4^o R_{\parallel}] C_o(\phi + \phi'). \quad (4.49)$$

The variables  $\psi_{1,2,3,4}^o$  for the  $m^{\text{th}}$  edge are given by

$$\psi_{1m}^o = \hat{u}_{\perp m}^o \cdot \hat{\phi}'_m \quad (4.50)$$

$$\psi_{2m}^o = \hat{u}_{\perp m}^o \cdot \hat{\beta}_{cm} \quad (4.51)$$

$$\psi_{3m}^o = \hat{u}_{\perp m}^o \cdot \hat{\phi}_m, \text{ and} \quad (4.52)$$

$$\psi_{4m}^o = \hat{u}_{\perp m}^o \cdot \hat{\beta}_{ocm} \quad (4.53)$$

The unit vector  $\hat{u}_{\perp}^o$  for the  $m^{\text{th}}$  edge is given by

$$\hat{u}_{\perp m}^o = \frac{\hat{n}_m^o \times \hat{I}}{|\hat{n}_m^o \times \hat{I}|} \quad (4.54)$$

Note that  $\hat{n}_m^o$  is the unit vector normal to the  $o$  or  $n$  face, respectively, of the  $m^{\text{th}}$  edge.

Next, consider the distance parameters. Recall from Section 2.4 that

$$L = \frac{s' s''}{s' + s''} \sin^2 \beta_o, \text{ and} \quad (4.55)$$

$$L_c = \frac{s_c s}{s_c + s} \quad (4.56)$$

Thus,  $L$  and  $L_c$  increase without bound as source and observer move into the far zone. For this reason, the transition functions  $F[kL_c a(\pi + \beta_{oc} - \beta_c)]$  and  $F[kLa^{\pm}(\phi + \phi')]$  can be set to unity. This is equivalent to saying that an observer in the far zone will never be in the transition regions associated with the edge diffraction shadow boundary or the GO reflection shadow boundaries, respectively. (This is due to the fact that the transition regions collapse to the shadow boundaries in the far zone; an observer can only be in the transition region by being exactly on the shadow boundary.) On the other hand, the ratio  $L/L_c$  remains finite and the modification factor is significant in the solution. Upon considering Figures 26 and 29, it can be seen that  $L/L_c$  depends not on the absolute values of  $s$ ,  $s_c$ ,  $s'$ , and  $s''$ , but on their relative values. Thus one can compute, for the  $m^{\text{th}}$  edge,

$$(L/L_c)_m = \frac{\left( \frac{s'_m s''_m}{s'_m + s''_m} \right) \sin^2 \beta_{om}}{\left( \frac{s_c s}{s_c + s} \right)} \quad (4.57)$$

Note that

$$s_c = s = |\mathbf{R}_s| = |\mathbf{R}_o| \quad (4.58)$$

$$s'_m = |\mathbf{I}_{QE_m}| = |\mathbf{R}_{D_m} - \mathbf{R}_s|, \text{ and} \quad (4.59)$$

$$s''_m = |\mathbf{D}_{QE_m}| = |\mathbf{R}_o - \mathbf{R}_{D_m}|. \quad (4.60)$$

For the backscatter case, this reduces to  $(L/L_c)_m = \sin \beta_{cm}$ .

The only quantities not yet mentioned are  $E_{\beta_c}^i(Q_C)$  and  $E_{\phi}^i(Q_C)$ . These are found simply by taking appropriate dot products.

### 4.3 Sample Calculations

The computations discussed in the previous section have been used to generate the "Absorber code". In this section, the Absorber code is used to calculate the scattering from a single pyramidal tip in various monostatic and bistatic scattering cases. The conventions defined in Figures 23 and 27 will be referred to here. The following figures plot the ratio of the amplitude of the scattered electric field to that of the incident electric field. Since the observer is assumed to be in the far zone, the  $1/s$  term in the corner diffraction formulation is ignored.

First consider the backscatter case, depicted by the solid curve in Figure 30, where  $\phi^i = \phi^s = 0^\circ$  and  $0^\circ < \theta^i = \theta^s < 90^\circ$ . The incident electric field is  $\theta$  polarized, the frequency is 5 GHz, and the pyramidal absorber is characterized by  $\alpha = 21^\circ$  and  $\epsilon_r = 1.45 - j0.58$ . As  $\theta^i$  varies, the incident ray striking the tip sweeps through the  $\phi = 0^\circ$  plane, which is perpendicular to face 1. As  $\theta^i$  increases through  $10^\circ$ , a small discontinuity is seen; here face 3 drops into the shadow region, and false shadow boundaries (see Section 2.4) exist for the  $o$  face of edge 2 and the  $n$  face of edge 3. As  $\theta^i$  increases through  $79^\circ$ , the source is broadside to face 1, and a singularity is seen. Note that a singularity in these far-zone calculations

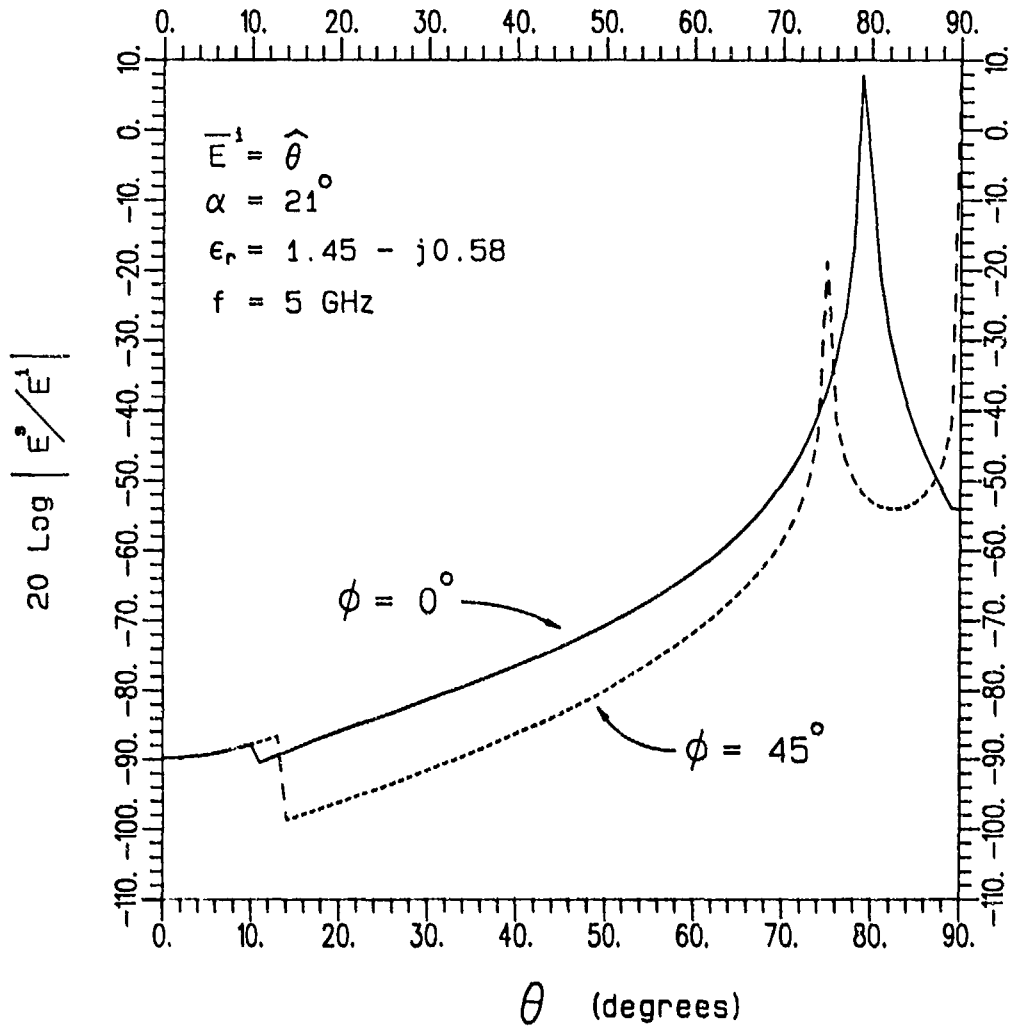


Figure 30: Backscatter in the  $\phi = 0^\circ$  and  $45^\circ$  planes from the tip of an absorber pyramid.

indicates that the local field behavior is cylindrical or planar (as opposed to spherical). (A singularity would not occur in a near-zone calculation, where all distance variables are well-known, all transition functions are included in the calculation, and the  $1/s$  spread factor is not dropped.) In the solid curve of Figure 30, the singularity occurs when the source (observer) is broadside to face 1. At broadside, the observer is at the GO RSBs of face 1 and the edge diffraction SBs of edges 1 and 4. The incident field, assumed planar, produces a planar reflected field from face 1. To smooth the discontinuity caused by the (planar) reflected field, the edge diffracted field must behave as a planar field near the RSB, which lies along the edge diffraction SB. Thus, the corner diffracted field must behave as a planar field in this same (backscatter) direction in order to smooth the discontinuity in the edge diffracted field.

The second (dashed) curve in Figure 30 is for the same case, except that  $\phi^i = \phi^s = 45^\circ$ . At  $\theta^i = 0^\circ$ , both curves have the same value since both represent nose-on incidence. This is also the lowest backscatter value on the plot, indicating that the absorber performs best at nose-on incidence, as expected. In the second case, as  $\theta^i$  varies, the incident ray striking the tip sweeps through the  $\phi = 45^\circ$  plane, which contains edge 1. A discontinuity is seen at  $\theta^i = 14^\circ$ ; here faces 3 and 4 drop into the shadow region, false shadow boundaries exist for the  $o$  face of edge 2 and the  $n$  face of edge 4, and contributions from edge 3 are ignored since  $\phi_3, \phi_3' > n\pi$ . This case has a singularity at  $\theta^i = 75^\circ$ , where the source direction is perpendicular to edge 1; this case has another singularity at  $\theta^i = 90^\circ$ , where the source direction is perpendicular to both edges 2 and 4. In these instances, the source (observer) is along edge diffraction SBs only. Edge diffracted rays leaving the edge move in parallel directions to the (far zone) observer. Thus, the edge and corner diffracted fields again do not decay as a spherical wave, and a singularity

results in the calculations.

Note that if one were to consider a finite pyramid (by including base diffraction), these singularities would not exist. Planar GO fields would emanate from finite faces, and planar edge diffracted fields would emanate from finite edges; both would radiate at one precise angle, neither are seen in the far zone. Of course, the tip diffracted term does not change, its singular component cancels with a like component of the base diffracted field.

Figure 31 illustrates the effect of the pyramid angle  $\alpha$ . The two values considered for  $\alpha$  are  $10^\circ$  and  $21^\circ$ ; other parameters are indicated in the figure. Clearly the tip diffracted fields decrease a few dB with decreasing  $\alpha$ . Of course, for constant pyramid height, smaller values of  $\alpha$  mean more pyramids per square foot. Changing  $\alpha$  also affects the geometry of reflected and transmitted fields.

Next the effect of absorber permittivity is illustrated in Figure 32, where the two curves correspond to  $\epsilon_r = 1.45 - j0.58$  and  $\epsilon_r = 1.38 - j0.2$ . These values correspond to medium and light doping, respectively [7]. Other parameters are indicated in the figure. Again, the tip diffracted fields decrease a few dB with decreasing permittivity (note that it is the imaginary part of the permittivity that has decreased most significantly). Of course, attempting to use this lower doped material throughout the pyramid to reduce the scattered fields would detract from the nature of the absorbing material. However, tapered material could be used to solve this problem.

The frequency under consideration has no effect upon the nature of any scattering plot; varying frequency can only shift the plot up or down. This results from the pyramid being effectively of infinite extent.

A bistatically scattered field case is depicted in Figure 33, where the incident direction is specified by  $\theta^i = 45^\circ$ ,  $\phi^i = 0^\circ$  and the scattered direction by

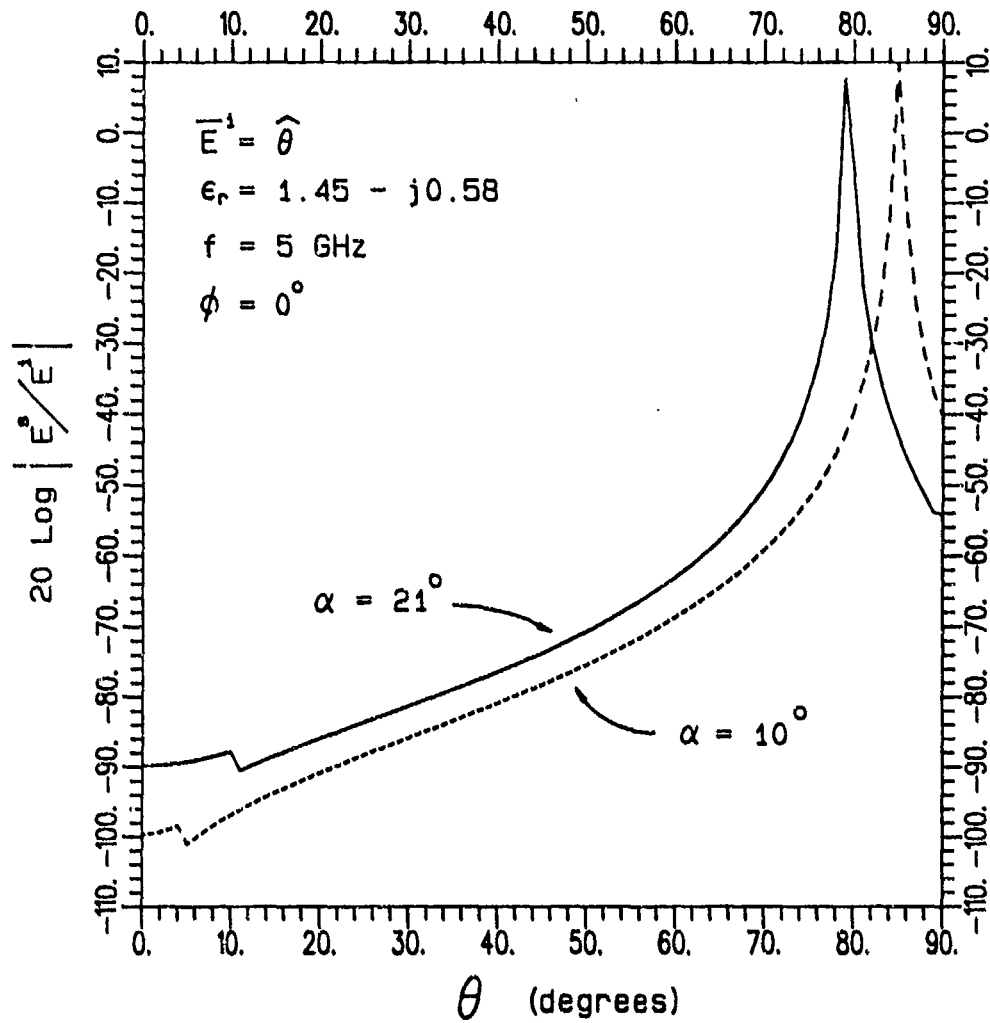


Figure 31: Backscatter from a pyramidal absorber tip in the  $\phi = 0^\circ$  plane, for two values of  $\alpha$ .

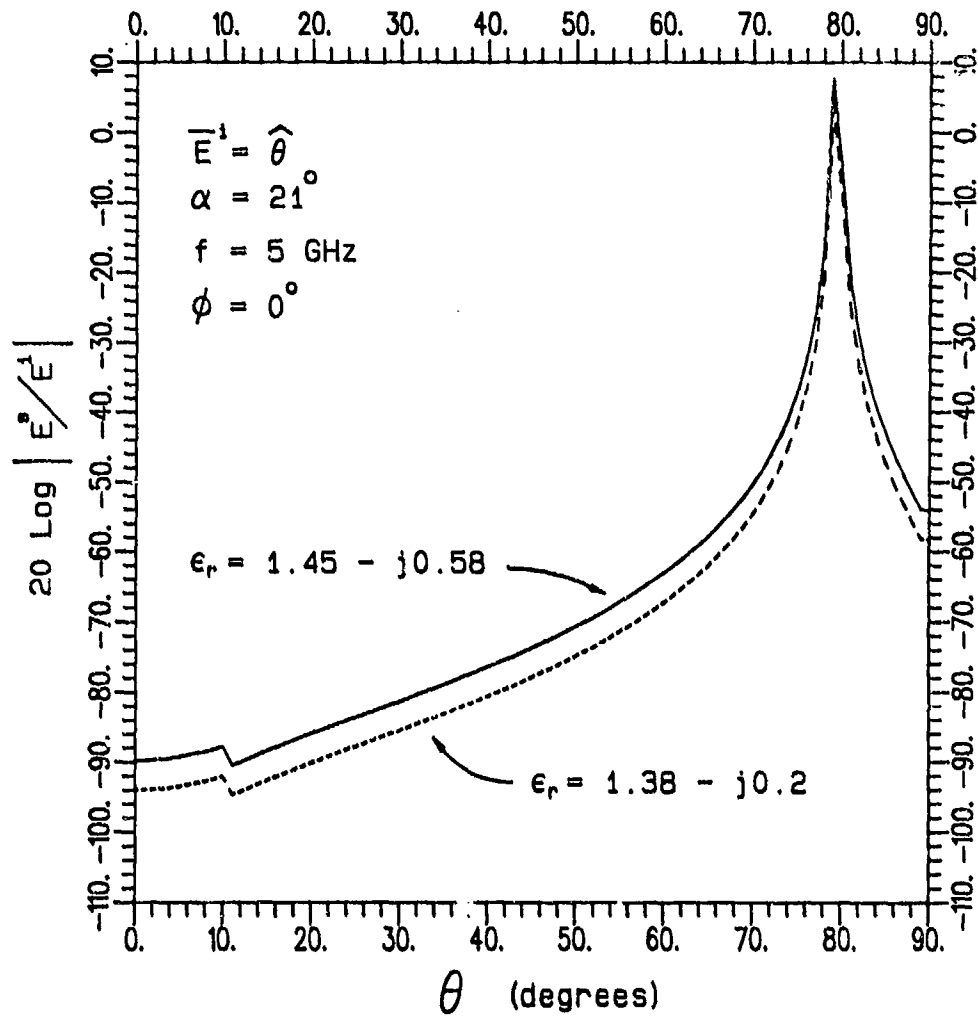


Figure 32: Backscatter from a pyramidal absorber tip in the  $\phi = 0^\circ$  plane, for two values of  $\epsilon_r$ .

$0^\circ < \theta^s < 90^\circ$ ,  $\phi^s = 180^\circ$ . Again, the remaining parameters are indicated in the figure. The first discontinuity, at about  $\theta^s = 45^\circ$ , is due to false shadow boundaries associated with the  $o$  face of edge 2 and the  $n$  face of edge 3. The second discontinuity, at about  $\theta^s = 55^\circ$ , is due to false shadow boundaries associated with the  $o$  face of edge 4 and the  $n$  face of edge 1.

One more bistatic case is illustrated in Figure 34, where  $\theta^i = 45^\circ$ ,  $\phi^i = 0^\circ$ ,  $\theta^s = 45^\circ$ , and  $0^\circ < \phi^s < 360^\circ$ . Thus the incident direction is fixed, and the scattered direction sweeps through a conical pattern centered on the  $z$  axis. There are two causes for the various discontinuities, false shadow boundaries and edge shadowing ( $\phi$  or  $\phi'$  not in the range from 0 to  $n\pi$  for some edge). These are specified in the figure.

While the discontinuities seen in these plots may seem rather severe, one must realize that the levels involved are extremely low, and that a very complex phenomenon is being treated approximately. There is no desire, in the present study, to attempt to eliminate these discontinuities. In chapter VI, comparisons made between calculations and measurements for both a single pyramid and many pyramids will build confidence in this scattering formulation.

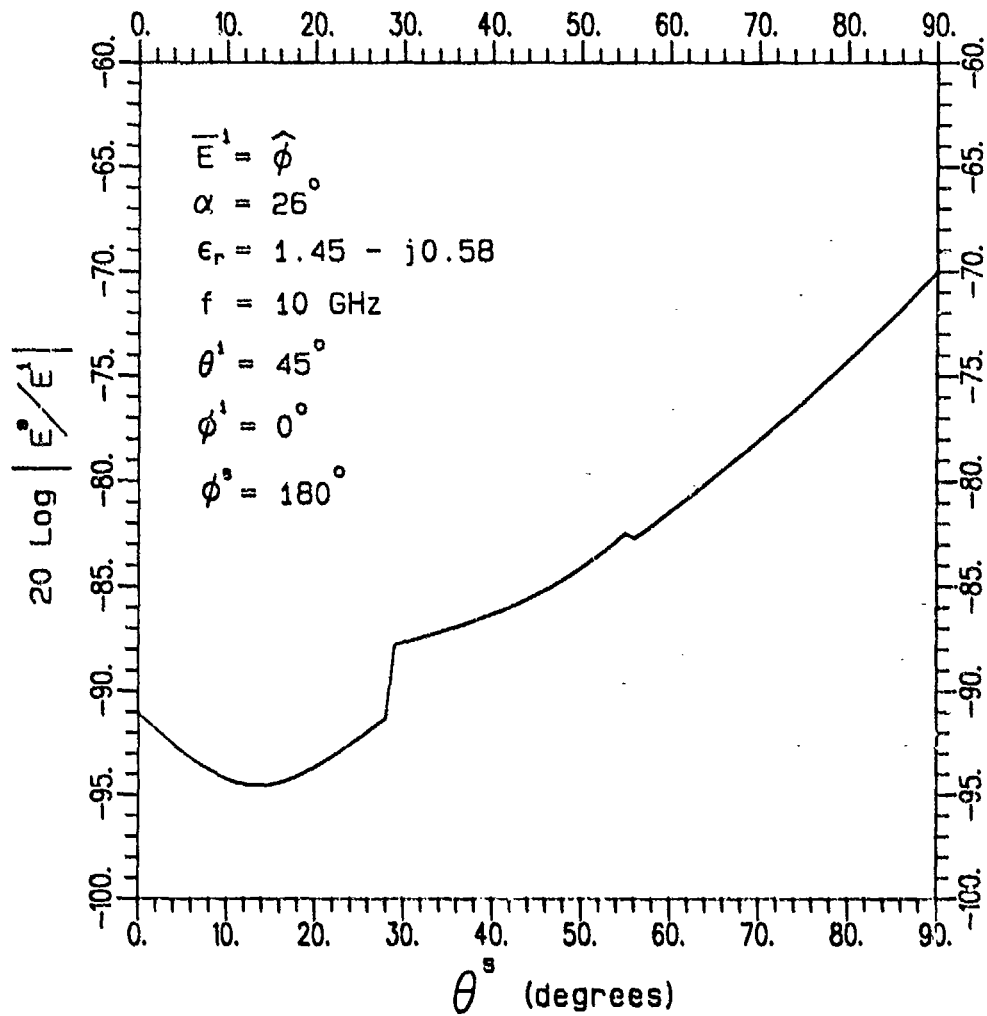


Figure 33: Bistatic scattering in the  $xz$  plane from the tip of an absorber pyramid.

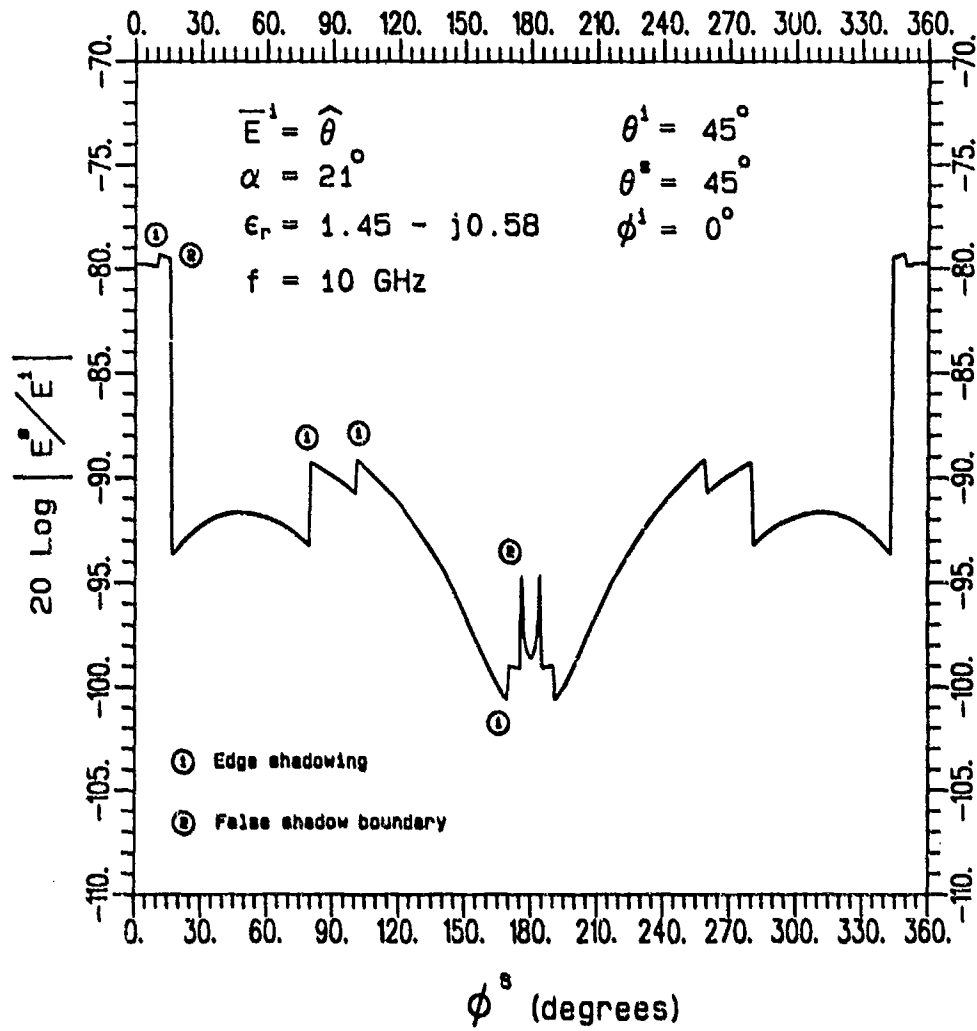


Figure 34: Bistatic scattering along the  $\theta^s = 45^\circ$  cone from the tip of an absorber pyramid.

## CHAPTER V

### PYRAMIDAL ABSORBER SCATTERING IN A COMPACT RANGE

#### 5.1 Introduction

In chapter III, the formulation for dielectric corner diffraction was developed. Chapter IV then described how to apply this formulation to a pyramidal tip, thus generating the single pyramid bistatic scattering code (Absorber code). This chapter investigates the scattering from the pyramidal absorber material in the compact range chamber that occurs during normal operation of the range. The method of calculation is discussed first, followed by sample calculations.

#### 5.2 Method of Calculation

The scattering into the target zone of a compact range from the pyramidal absorber which lines the ceiling, side walls, and floor of an anechoic chamber is now considered. Figure 35 shows typical absorber scattering paths for ceiling and floor absorber. Similar paths exist for absorber along the side walls. The analysis is limited to tip diffraction, which is believed to be the dominant scatterer as the incident or scatter direction moves away from nose-on incidence [7,13]. This has been demonstrated in bistatic measurements where scattering was measured at various angles from a wall of pyramidal absorber [7]. In any case, the Absorber code computes only tip diffraction and will be used here to predict the total absorber

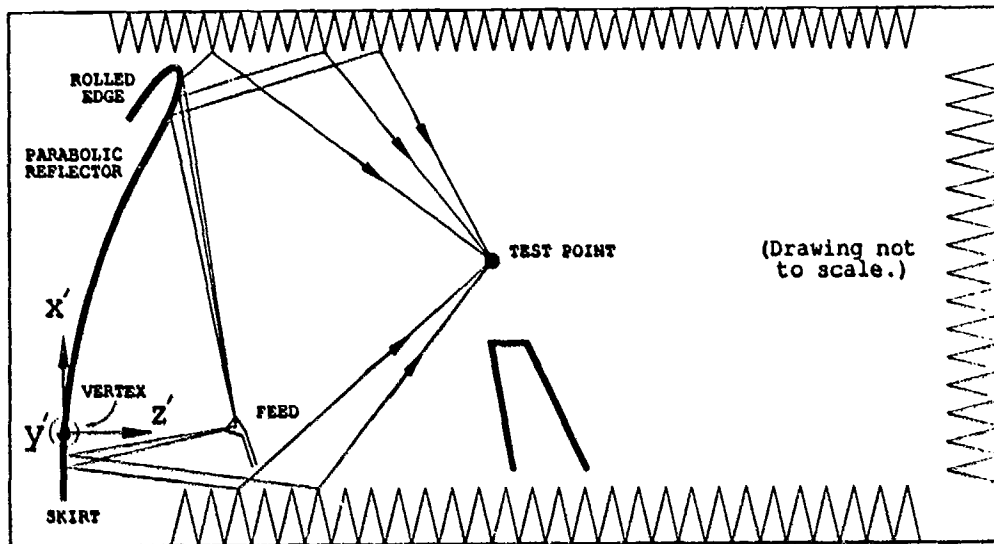


Figure 35: Typical absorber scattering paths calculated by CHAMBER.

scattering that takes place in a chamber.

A computer program, CHAMBER, has been written to calculate the absorber scattering in a compact range chamber. CHAMBER considers a simple rectangular room, as depicted in Figure 36. The ceiling, side walls, and floor are lined with pyramidal absorber. The rear wall is neglected since it would be outside the range gate in a well-designed room. A focus-fed semi-circular parabolic reflector with a rolled edge and a skirt illuminates the room. This is also depicted in Figure 36. Note that the origin of a cartesian coordinate system is placed at the reflector vertex. This is henceforth referred to as the "room coordinate system." A few variables used in CHAMBER are shown in Figure 36, they are defined as follows:

$x\_tips\_ceil$  = Room  $x'$  coordinate of tips of ceiling pyramids.

$x\_tips\_floor$  = Room  $x'$  coordinate of tips of floor pyramids.

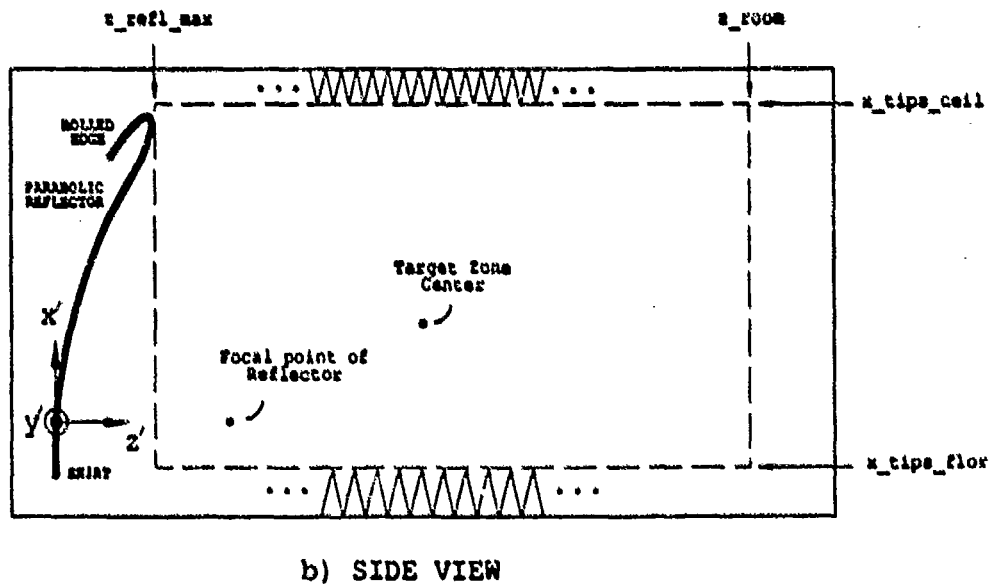
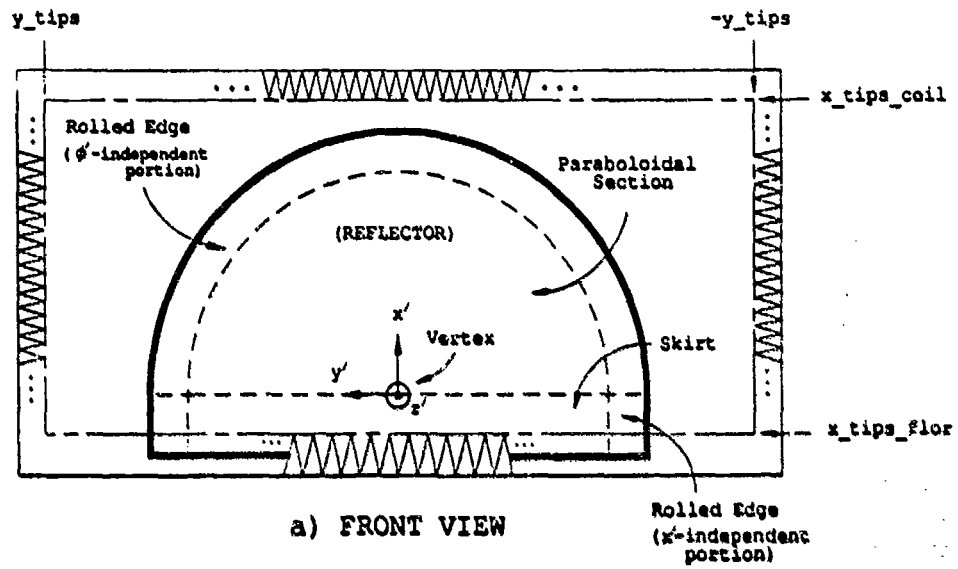


Figure 36: Anechoic room considered in absorber scatter calculations.

**y\_tips** = Room  $y'$  coordinate of tips of side wall pyramids.

**z\_refl\_max** = Maximum  $z'$  coordinate of range reflector.

**z\_room** = Maximum  $z'$  coordinate considered in the room.

It is through these variables that one specifies the room dimensions. The user must also specify the intended location of the target zone center, along with absorber parameters, feed and reflector parameters, and timing parameters. This is described fully in Appendix A, which explains how to run CHAMBER.

CHAMBER begins by choosing patches along the ceiling, walls, and floor that it will consider for its scattering calculations. The extent of these patches roughly coincides with the variables described above. However, it is desirable to have patch dimensions that are multiples of 0.5 ft. Thus, CHAMBER finds the following variables:

**x\_room\_min** = Smallest multiple of 0.5 ft  $\geq$  **x\_tips\_floor**.

**x\_room\_max** = Largest multiple of 0.5 ft  $\leq$  **x\_tips\_ceil**.

**y\_room\_min** = Zero.

**y\_room\_max** = Largest multiple of 0.5 ft  $\leq$  **y\_tips**.

**z\_room\_min** = Smallest multiple of 0.5 ft  $\geq$  **z\_refl\_max**.

**z\_room\_max** = Largest multiple of 0.5 ft  $\leq$  **z\_room**.

The ceiling patch is then specified by

$$y_{\text{room\_min}} \leq y' \leq y_{\text{room\_max}} \quad (5.1)$$

$$z_{\text{room\_min}} \leq z' \leq z_{\text{room\_max}}, \text{ and} \quad (5.2)$$

$$z' = x_{\text{tips\_ceil}} \quad (5.3)$$

while the side wall patch is specified by

$$x_{\text{room\_min}} \leq x' \leq x_{\text{room\_max}} \quad (5.4)$$

$$z_{\text{room\_min}} \leq z' \leq z_{\text{room\_max}}, \text{ and} \quad (5.5)$$

$$y' = y_{\text{tips}} \quad (5.6)$$

and the floor patch is specified by

$$y_{\text{room\_min}} \leq y' \leq y_{\text{room\_max}} \quad (5.7)$$

$$z_{\text{room\_min}} \leq z' \leq z_{\text{room\_max}}, \text{ and} \quad (5.8)$$

$$x' = x_{\text{tips\_flor}}. \quad (5.9)$$

Note that these patches cover *half* of the ceiling, *one* side wall, and *half* of the floor. However, CHAMBER does effectively consider both sides of the room. This will become clear shortly.

CHAMBER then divides each patch into "resolution" cells which measure  $0.5' \times 0.5'$ . Imaginary grids are set up for each patch, with grid points at the center of each cell, as depicted in Figure 37. CHAMBER assumes that a pyramidal tip is present at each grid point, and all calculations will be made with this imaginary tip in mind. These calculations are then assumed valid for each of the actual pyramids within the corresponding cell.

CHAMBER now determines the illumination at each grid point. To do this, the Semi-Circular Compact Range Reflector Code [9] has been taken and modified for the current problem. The result, subroutine REFL.CODE, provides CHAMBER with the following information for each grid point:

- The (complex)  $x'$ ,  $y'$ , and  $z'$  components of the illuminating GO electric field. (This is a reflected field from the compact range reflector.)

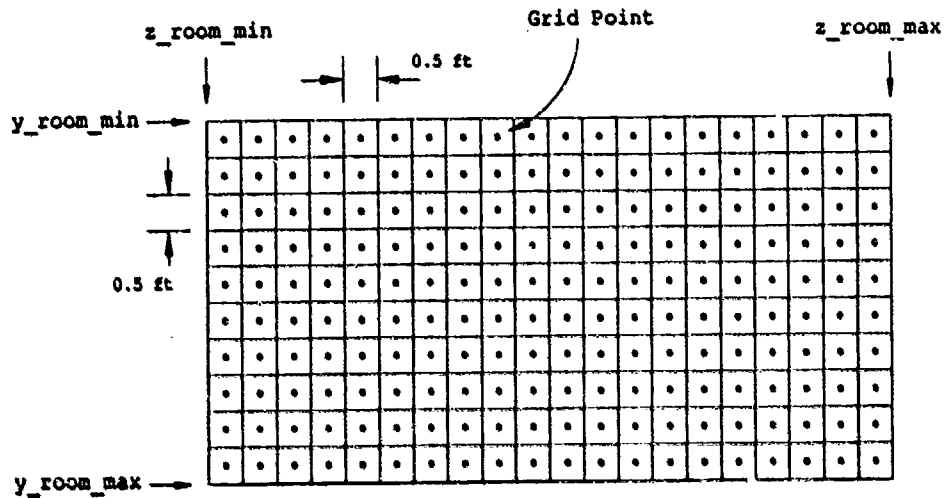


Figure 37: Imaginary grid along ceiling patch.

- The corresponding point of reflection on the reflector.

Note that the Reflector code does not provide accurate phase information for the fields outside the target zone, due to an approximate method used in finding reflection points along the rolled edge of the reflector. (The only exception to this is the portion of the floor illuminated by the skirt, where reflection points are easily found.) However, phase information would not be used here anyway, due to the random nature of the tip positions. (Pyramidal absorber typically comes in 2' x 2' blocks, which are not perfectly aligned when placed in the room. Also, the height of individual pyramids varies, and pyramids tend to bend, twist, and sag.) CHAMBER does, however, use the phase information provided to determine the relative polarization of the field components, which is, of course, essential. Thus, at this point, CHAMBER has the following information at each grid point:

- The amplitude (and sign) of the  $x'$ ,  $y'$ , and  $z'$  components of the illuminating electric field.
- The incident direction of the field illuminating the grid point (since the corresponding reflection point is known).

Next, CHAMBER must compute the scattering from each grid point to the field test point. The choice of field test point will be addressed later when the various options available in CHAMBER are discussed. For the moment, assume that the test point is fixed somewhere in the target region. The Absorber code will be used to compute the scattering from each grid point. Recall that the Absorber code considers a pyramidal tip located at the origin of a cartesian coordinate system, as depicted in Figure 23. This is referred to here as the "pyramidal coordinate system". The Absorber code requires the input variables  $\theta^i$ ,  $\phi^i$ ,  $E_\theta^i$ ,  $E_\phi^i$ ,  $\theta^s$ , and  $\phi^s$ . These pertain to the pyramidal coordinate system. Thus, a pyramidal coordinate system must be located at each grid point. Note that the  $z$  axis of each pyramidal coordinate system must be directed into the room, since this corresponds to the pyramid being directed into the room. Sample ceiling, wall, and floor pyramid coordinate systems are shown in Figure 38, along with the room coordinate system.

Consider a ceiling pyramid coordinate system whose origin is at some observation point (grid point) of the illuminating field. The coordinates of this origin in the room coordinate system may be expressed as

$$(x', y', z') = (x_0, y_0, z_0) \quad (5.10)$$

The transformation between room coordinates  $(x', y', z')$  and ceiling pyramid co-

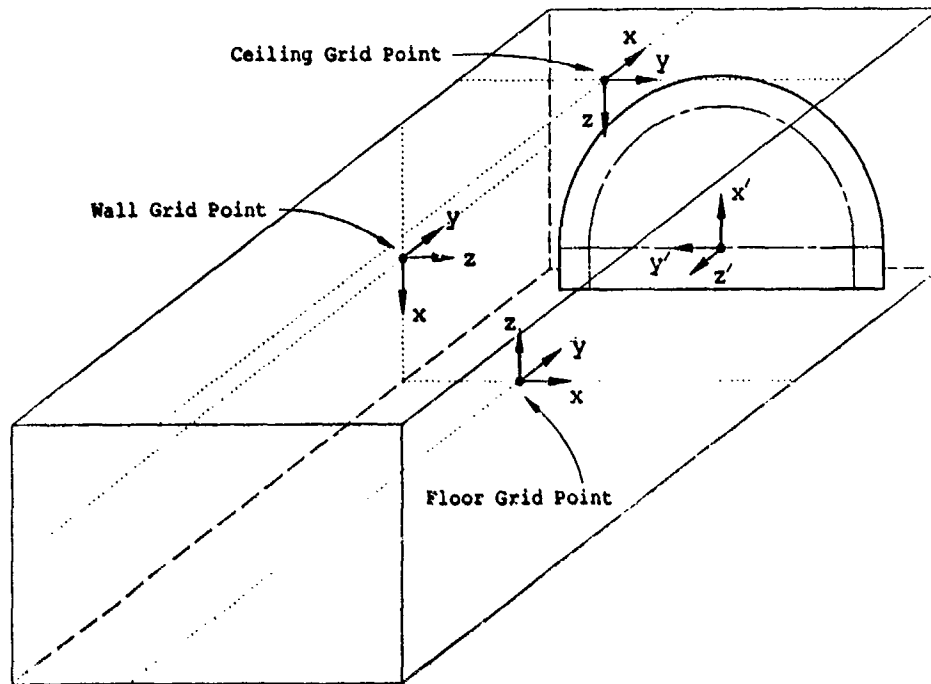


Figure 38: Typical "pyramidal coordinate systems" used by the Absorber Code.

ordinates  $(x, y, z)$  is given by

$$x = z_0 - z' \quad (5.11)$$

$$y = y_0 - y' \text{ , and} \quad (5.12)$$

$$z = x_0 - x' \text{ .} \quad (5.13)$$

Let the reflection point (on the reflector) corresponding to this grid point be expressed in the room coordinate system as

$$(x', y', z') = (x_r, y_r, z_r) \text{ .} \quad (5.14)$$

Then, this reflection point is expressed in the ceiling pyramid coordinate system as

$$(x, y, z) = (z_0 - z_r, y_0 - y_r, x_0 - x_r) \text{ .} \quad (5.15)$$

Similarly, if a grid point along the wall is specified by

$$(x', y', z') = (x_o, y_o, z_o) \quad (5.16)$$

and its corresponding reflection point is specified by

$$(x', y', z') = (x_r, y_r, z_r) \quad (5.17)$$

then the reflection point is expressed in the wall pyramid coordinate system as

$$(x, y, z) = (x_o - x_r, z_o - z_r, y_o - y_r) . \quad (5.18)$$

The analogous result for a reflection point which corresponds to a floor grid point is expressed in the floor pyramid coordinate system as

$$(x, y, z) = (y_o - y_r, z_o - z_r, -x_o + x_r) . \quad (5.19)$$

Thus, every grid point is the origin of a pyramidal coordinate system, and the reflection point corresponding to each grid point is known in terms of its  $(x, y, z)$  coordinates in this coordinate system. These coordinates can be used to find the angles of incidence required by the Absorber code  $(\theta^i, \phi^i)$ .

Next, the field illuminating each grid point must be expressed in the pyramidal coordinate system at that grid point. The amplitude (and sign) of the illuminating electric field is known in room coordinates for every grid point; let these (signed) amplitudes be denoted by  $E_{x'}$ ,  $E_{y'}$ , and  $E_{z'}$ . These can be expressed in the pyramidal coordinate directions at a ceiling grid point through the following transformation

$$E_x = -E_{z'} \quad (5.20)$$

$$E_y = -E_{y'} \quad , \text{ and} \quad (5.21)$$

$$E_z = -E_{x'} . \quad (5.22)$$

For a wall grid point, the transformation is given by

$$E_x = -E_{x'} \quad (5.23)$$

$$E_y = -E_{z'} \text{ , and} \quad (5.24)$$

$$E_z = -E_{y'} \quad (5.25)$$

while the transformation for a floor grid point is given by

$$E_x = -E_{y'} \quad (5.26)$$

$$E_y = -E_{z'} \text{ , and} \quad (5.27)$$

$$E_z = E_{x'} \text{ .} \quad (5.28)$$

Thus, the incident field components ( $E_\theta^i$ ,  $E_\phi^i$ ) required by the Absorber code can be found for all grid points as

$$E_\theta^i = E_x \cos \theta^i \cos \phi^i + E_y \cos \theta^i \sin \phi^i - E_z \sin \theta^i \text{ , and} \quad (5.29)$$

$$E_\phi^i = -E_x \sin \phi^i + E_y \cos \phi^i \quad (5.30)$$

where  $E_x$ ,  $E_y$ ,  $E_z$ ,  $\theta^i$ , and  $\phi^i$  pertain to that grid point.

CHAMBER finds the scattering angles ( $\theta^s$ ,  $\phi^s$ ) from the room coordinates of the grid point and field test point. CHAMBER then provides all of these variables ( $\theta^i$ ,  $\phi^i$ ,  $E_\theta^i$ ,  $E_\phi^i$ ,  $\theta^s$ ,  $\phi^s$ ) along with the pyramid angle,  $\alpha$ , the pyramid relative permittivity,  $\epsilon_r$ , and the frequency under consideration to the Absorber code (for each grid point).

The Absorber code returns the complex  $x$ ,  $y$ , and  $z$  components of the field scattered from every grid point to the test point (with the  $1/s$  spreading factor being ignored). CHAMBER uses these results, along with the distance from each grid point to the field test point (to account for spreading), to determine the scattered power contribution from every grid point to the field test point. The

contribution from each grid point is weighted by the number of pyramids in the corresponding cell.

This explains how CHAMBER computes the power scattered from each cell of the ceiling, wall, and floor patches to the test point. Recall, however, that these patches lie along one side of the room, and it was stated earlier that CHAMBER considers both sides of the room. To understand the approach used to account for the second side of the room ( $y' < 0$ ), consider Figure 39. Point F represents the feed, while point C is an arbitrary ceiling grid point, and R is the reflection point on the rolled edge corresponding to C. Let T be the field test point under consideration. The two diagrams in Figure 39 correspond to two locations of the test point; the following discussion applies to both cases.

The absorber scattering discussed thus far corresponds to the path F-R-C-T. However, for every ceiling grid point C, there is an image point  $C_{IM}$  from which one must determine the power scattered to the test point. (Note that  $C_{IM}$  has the same  $x'$ ,  $z'$  coordinates as C, but the negative of the  $y'$  coordinate of C.  $R_{IM}$  and  $T_{IM}$  are imaged in the same manner.) This second scattering path of interest is F- $R_{IM}$ - $C_{IM}$ -T. Due to the symmetry present in this problem, the power scattered to  $T_{IM}$  via path F-R-C- $T_{IM}$  is identical to the power scattered to T via path F- $R_{IM}$ - $C_{IM}$ -T. Computing the scatter via the latter path requires less of a programming effort and less computer run time. Thus, CHAMBER computes the scattered power contribution to test point T from ceiling point C via path F-R-C-T, and computes the contribution to test point T from ceiling point  $C_{IM}$  via path F-R- $C_{IM}$ -T. This is done with every ceiling grid point, so that the entire image of the ceiling patch is considered. The wall and floor patches are treated similarly. (Note that when the test point moves to the room centerline, the test point and its image merge. The scattered power from any grid point and its image

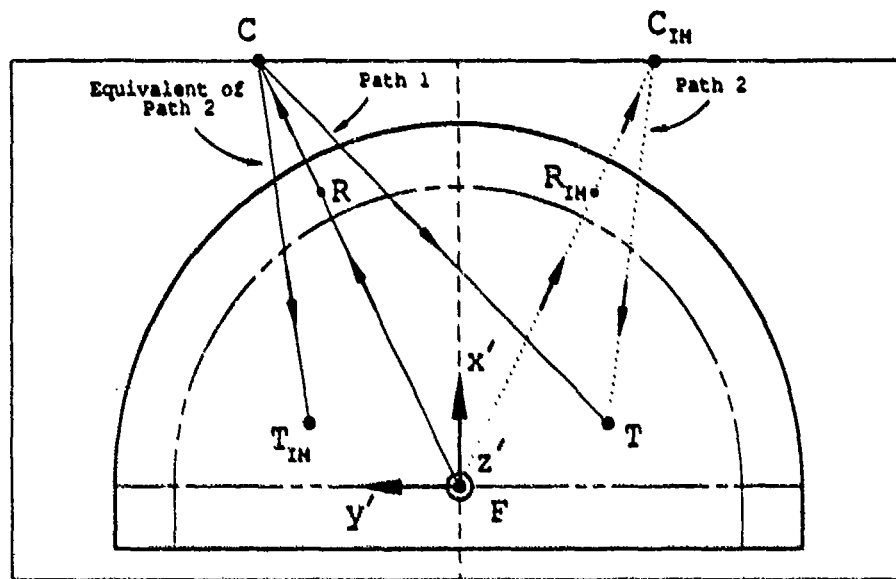
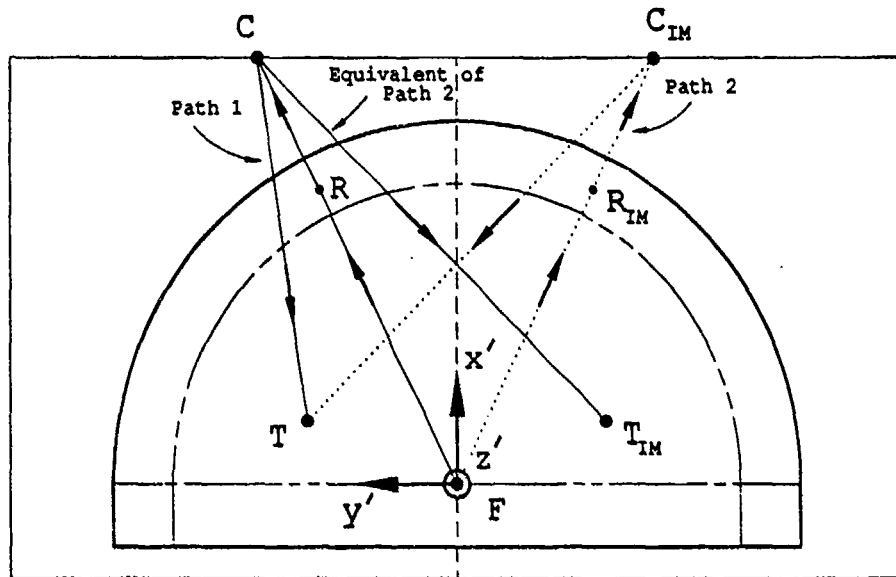


Figure 39: Equivalent absorber scattering paths used by CHAMBER for the ( $y' < 0$ ) side of the room.

is then the same, and need be computed only once.)

Thus, CHAMBER computes the scattered power contribution from the entire ceiling, wall, and floor patches and their images. However, only scattered fields arriving within a certain time window are considered. This is handled as follows. It is assumed that the chamber operates with a narrow transmit pulse (in the OSU range this is about 5 - 7 ns) and a relatively wide receive window (in the OSU range this is variable, typically set to 20 ns). The target zone center, the start and end times of the receive window, and the field test point have been specified by the user. The time reference is the time at which a signal would be received due to the incident plane wave scattering from a point target at the target zone center. The signal scattered from some grid point to the specified test point is considered only if that signal could then be scattered from a point target at the test point and arrive at the feed (via the reflector) within the receive window. This is illustrated in Figure 40. The reference time is the propagation time along path  $F-R_C-TZC-R_C-F$ . Assume that the reference time is 70ns, and the specified receive window start and end times are -10ns and +10ns, respectively. The scattered fields from the grid point are considered only if the propagation time along path  $F-R_A-G-TP-R_B-F$  is between 60ns and 80ns. Other timing approaches are possible; this approach computes the scattered power from the absorber which could be scattered from some feature of an extended target (at the specified test point) and arrive within the receive window, thus corrupting the desired return.

Next, there is the question of addition of the scattered fields from the various grid points. CHAMBER computes total scattered power simply by adding the scattered power contributions from the individual pyramids. In the compact range ceiling scatter experiment described in the next chapter, various assumptions of

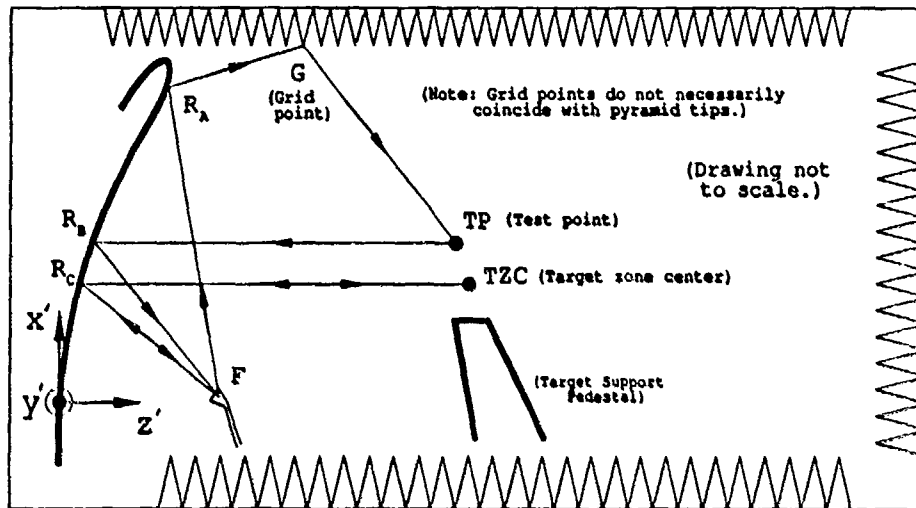


Figure 40: Timing considerations in CHAMBER.

field addition will be tested in the calculated curves.

Finally, note that all scattered power calculations are normalized to the power of the incident plane wave in the target zone. Also, if one requests CHAMBER to output the room illumination (from the range reflector), then this data is first normalized in the same manner.

### 5.3 Sample Calculations

In this section, CHAMBER is used to investigate the absorber performance for a particular compact range chamber configuration. As required by CHAMBER, a focus-fed semi-circular parabolic reflector with a rolled edge and a skirt is considered. The focal length of the reflector is 12 feet, while the radius of its parabolic section is 11.5 feet. The rolled edge is elliptical with a major axis of

4 feet and a minor axis of 1 foot. The feed horn is tilted above the horizontal by  $25^\circ$ . The tips of the ceiling pyramids are 16.25 feet above the vertex of the reflector (at  $x' = 16.25$  feet). The tips of the side wall pyramids are 20 feet to each side of the vertex of the reflector (at  $y' = \pm 20$  feet). The tips of the floor pyramids are 3.5 feet below the vertex of the reflector (at  $x' = -3.5$  feet). The ceiling and side wall pyramids are characterized by  $\alpha = 24.5^\circ$ ,  $\epsilon_r = 1.45 - j0.58$ , and a density of 20.25 pyramids per square foot. The floor pyramids are characterized by  $\alpha = 25.3^\circ$ ,  $\epsilon_r = 1.45 - j0.58$ , and a density of 4 pyramids per square foot. Note that the height of the skirt is not specified, but it is assumed to extend below the tips of the floor pyramids. The target zone center is specified to be on the room centerline, 6 feet above the reflector vertex, and 24 feet downrange from the vertex. In the room coordinate system, this is  $(x', y', z') = (6, 0, 24)$ . The relative start and end times of the receive window are  $-10$  ns and  $+10$  ns, respectively. The chamber is assumed to operate with a vertically-polarized plane wave in the target region. This is input to CHAMBER by specifying the appropriate electric and magnetic dipoles to simulate the feed (see appendix A).

Now, consider a test point coincident with the target zone center; that is, at  $(x', y', z') = (6, 0, 24)$  ft. Figure 41 displays the total scattered power versus frequency at this test point. Also shown is the scattered power from the ceiling and floor (scattered power from the side walls does not arrive during the specified time window). Clearly, the floor is the dominant scatterer for this situation.

Figures 42, 43, and 44 display the variation of scattered power versus test point  $x'$ ,  $y'$ , and  $z'$  coordinate, respectively. In all three figures, the frequency is fixed at 10 GHz. In Figure 42, the test point moves upward from  $(x', y', z') = (2, 0, 24)$  to  $(10, 0, 24)$  ft. The floor scatter is dominant when the test point is close to the floor, while the ceiling scatter dominates when the test point nears the ceiling.

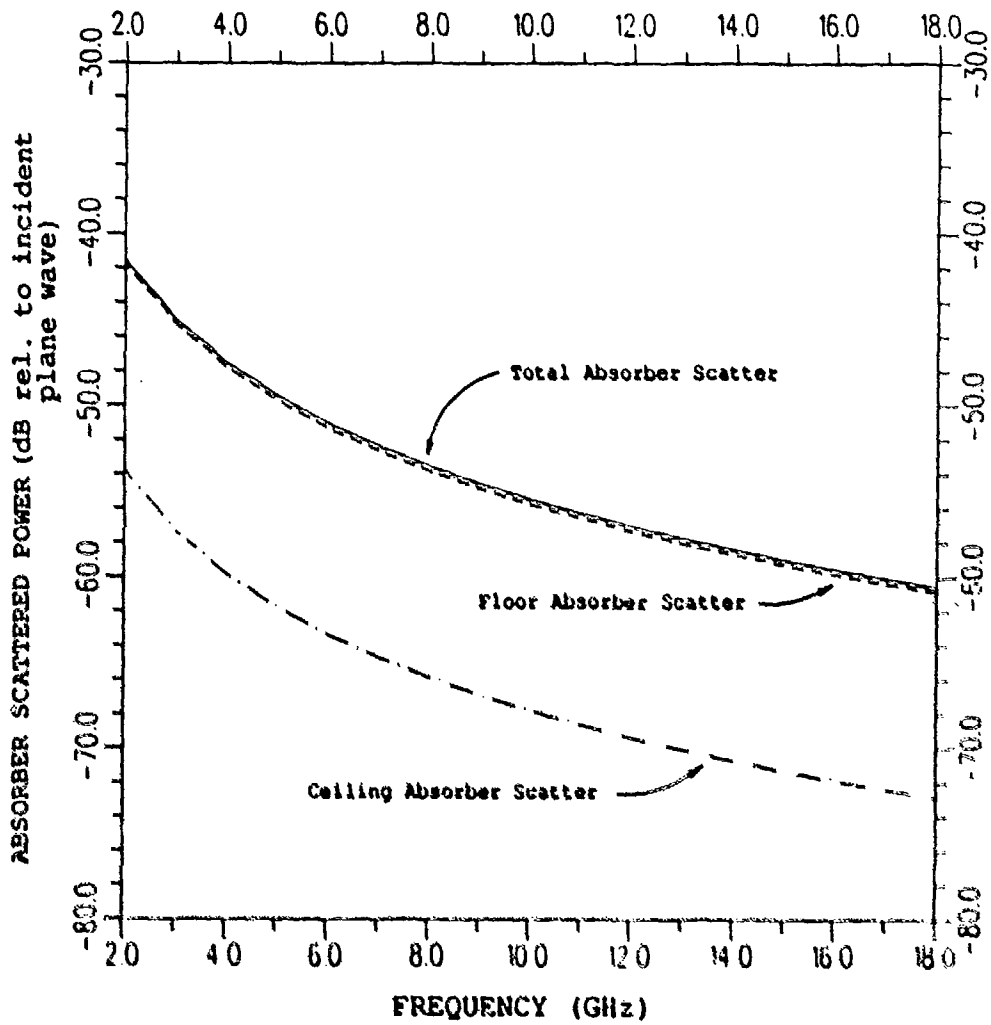


Figure 41: Absorber scattered power vs. frequency. Test point at  $(x', y', z') = (6, 0, 24)$  ft.

Owing to the nature of the Absorber code, some floor pyramids yield the small jumps present in the range  $2 < x' < 4$  ft. In Figure 43, the test point moves across the room from  $(x', y', z') = (6, -5, 24)$  to  $(6, 5, 24)$  ft. Clearly, the floor dominates throughout this range. Finally, in Figure 44, the test point moves downrange from  $(x', y', z') = (6, 0, 20)$  to  $(6, 0, 28)$  ft. Again, the floor is the major contributor to the absorber scattered power. Note that increased resolution is provided in the range  $20 < z' < 21$  ft. The singularity at 20.3 feet results from Absorber code calculations of some floor pyramids. Recall that the Absorber code is designed for far-zone calculations, and thus sets the transition functions to unity (see Section 4.2).

Now, let us fix the frequency at 10 GHz and the test point at the target zone center; that is, at  $(x', y', z') = (6, 0, 24)$  ft. Figures 45, 46, and 47 show the absorber illumination as a function of position along the ceiling, side wall and floor, respectively. Only half of the ceiling, one side wall, and half of the floor is shown, since the illumination is symmetric about the room centerline. To understand the discontinuities present in these figures, one must realize that the compact range reflector has four unique sections. Obviously, there is the parabolic section which produces the plane wave in the target region. The skirt is a cylindrical region (independent of the  $x'$  coordinate) whose  $y', z'$  behavior matches that of the parabolic section at  $x' = 0$ . The rolled edge consists of two regions; a rolled edge on the parabolic section (which is  $\phi'$ -independent, as is the parabolic section), and a rolled edge on the skirt (which is  $x'$ -independent). Figure 45 shows that the ceiling illumination is most intense along the room centerline just in front of the reflector. This portion of the ceiling is very close to the reflector, so that not much spreading occurs after reflection. There are no discontinuities in this plot

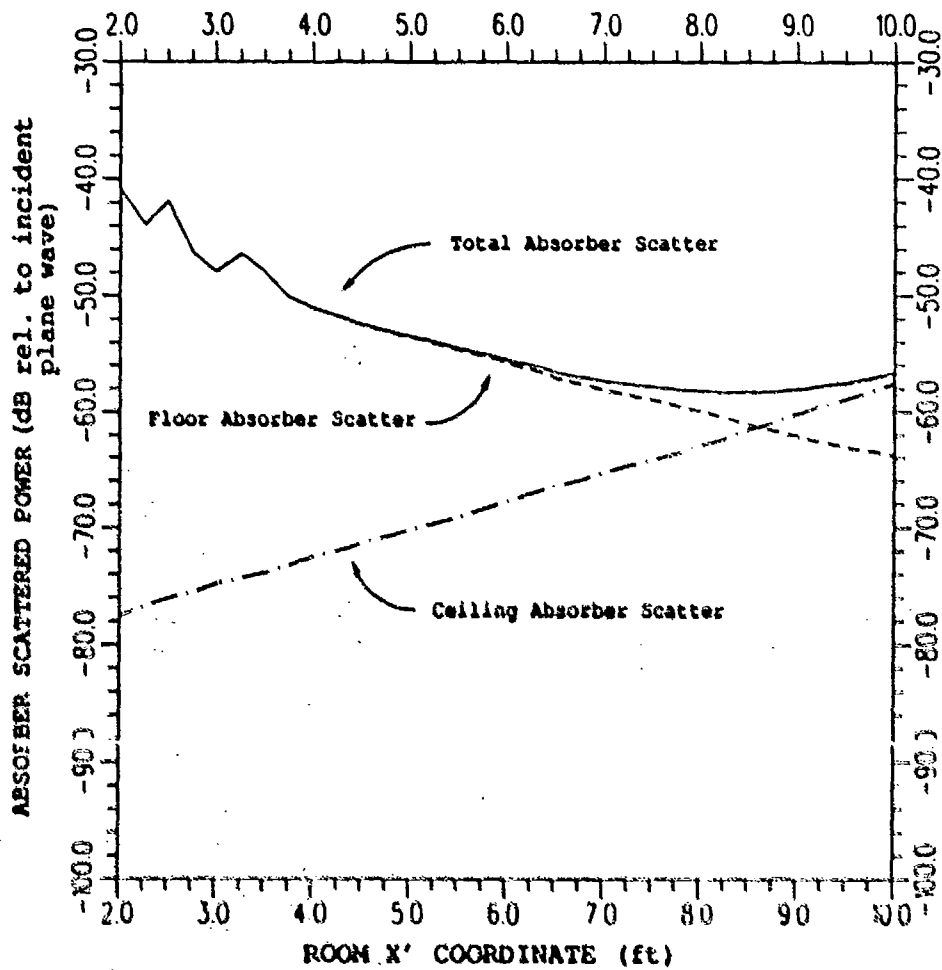


Figure 42: Absorber scattered power vs. test point  $x'$  coordinate. Frequency = 10 GHz. ( $y' = 0$ ,  $z' = 24$  ft).

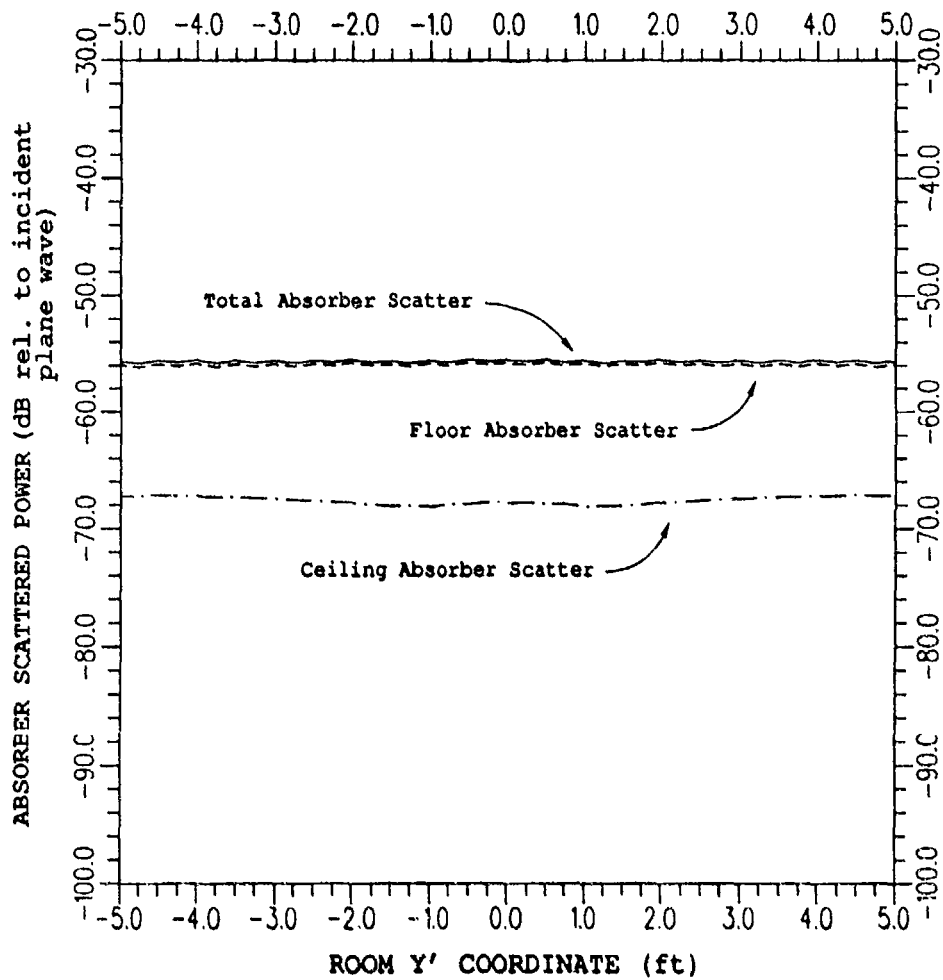


Figure 43: Absorber scattered power vs. test point  $y'$  coordinate. Frequency = 10 GHz. ( $x' = 6$  ft,  $z' = 24$  ft).

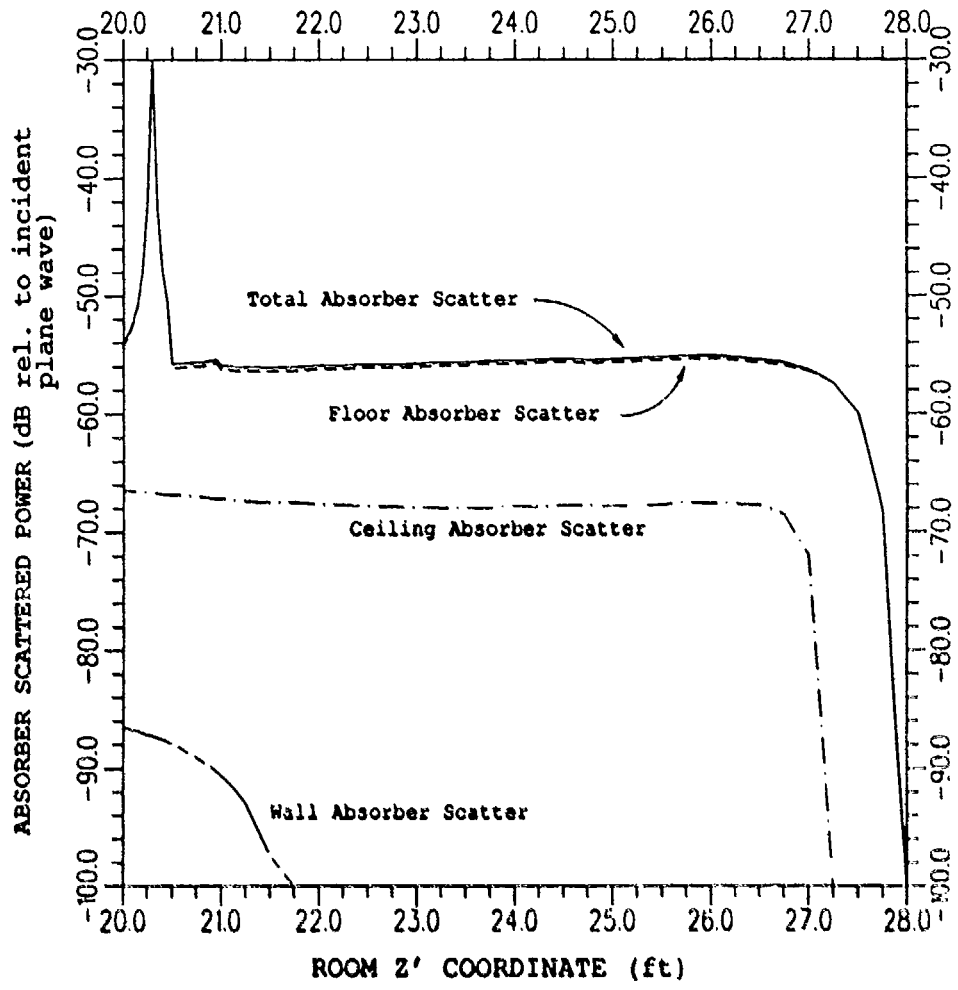


Figure 44: Absorber scattered power vs. test point  $z'$  coordinate. Frequency = 10 GHz. ( $x' = 6$  ft,  $y' = 0$ ).

since all reflection takes place on the rolled edge of the parabolic section. On the other hand, Figure 46 does have a discontinuity at  $x' = 0$ . This results from the reflection point having moved from the rolled edge of the skirt to the rolled edge of the parabolic section, thus causing a sudden change in the spread factor of the illuminating field. In Figure 47, the discontinuity at  $y' = 11.5$  feet is due to the reflection point having moved from the skirt to the skirt rolled edge. Clearly, the floor is strongly illuminated by the skirt. The absorber scattering to the test point from the ceiling and floor is depicted in Figures 48 and 49, respectively. The absorber scatter is symmetric about the room centerline, because the test point is on the room centerline. Thus, only half of the floor and ceiling is considered. Now, one can see that the receive window limits the portion of the ceiling and floor that contribute to the total absorber scatter. In fact, a plot of absorber scatter from the side wall is not included since none arrives during the specified time window. The floor scatter shows a discontinuity at  $y' = 11.5$  feet, due to the discontinuity in the illumination there. These absorber scatter plots show both smooth trends in the data and some abrupt changes. This is due largely to the Absorber code, which predicts such behavior as pyramidal incident and scatter angles vary. Finally, note that CHAMBER calculates the total absorber from the ceiling and floor to be -67.8 and -55.8 dB, respectively.

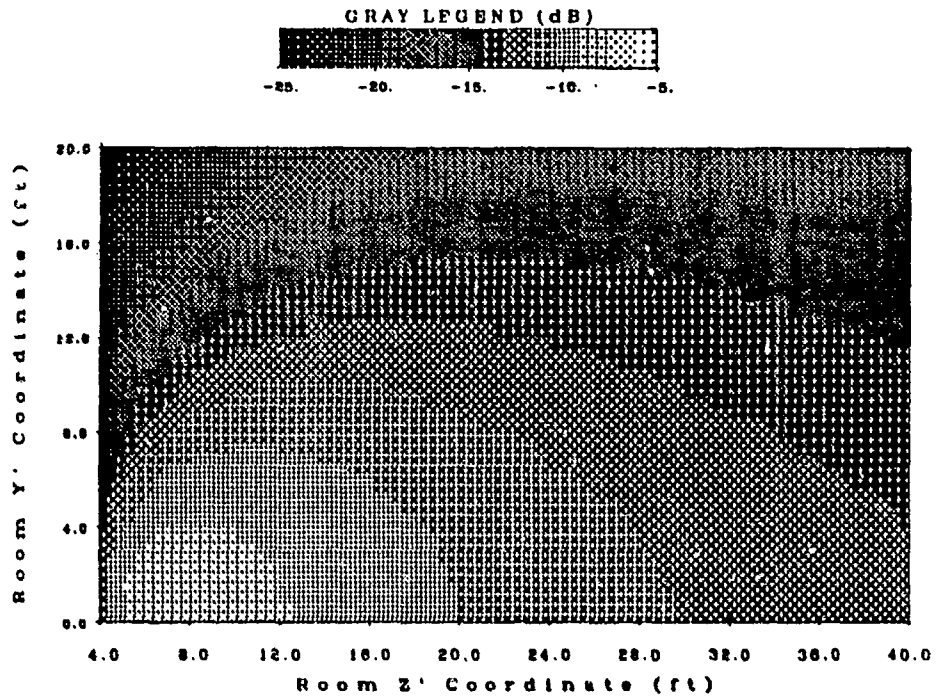


Figure 45: Ceiling illumination vs. ceiling  $y'$ ,  $z'$  coordinates. (dB rel. to incident plane wave).

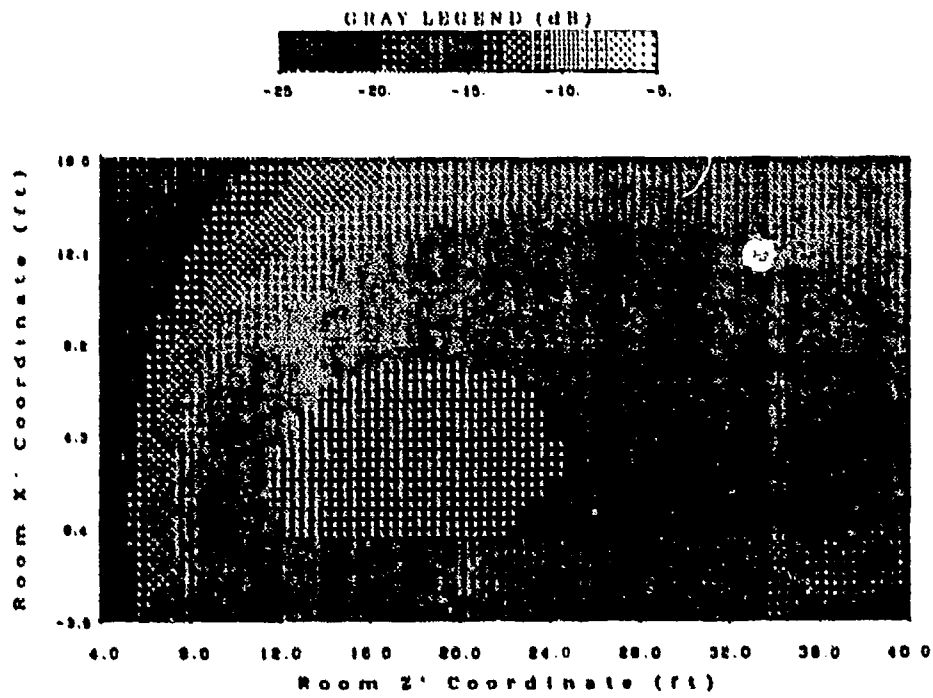


Figure 46: Wall illumination vs. wall  $x'$ ,  $z'$  coordinates. (dB rel. to incident plane wave).

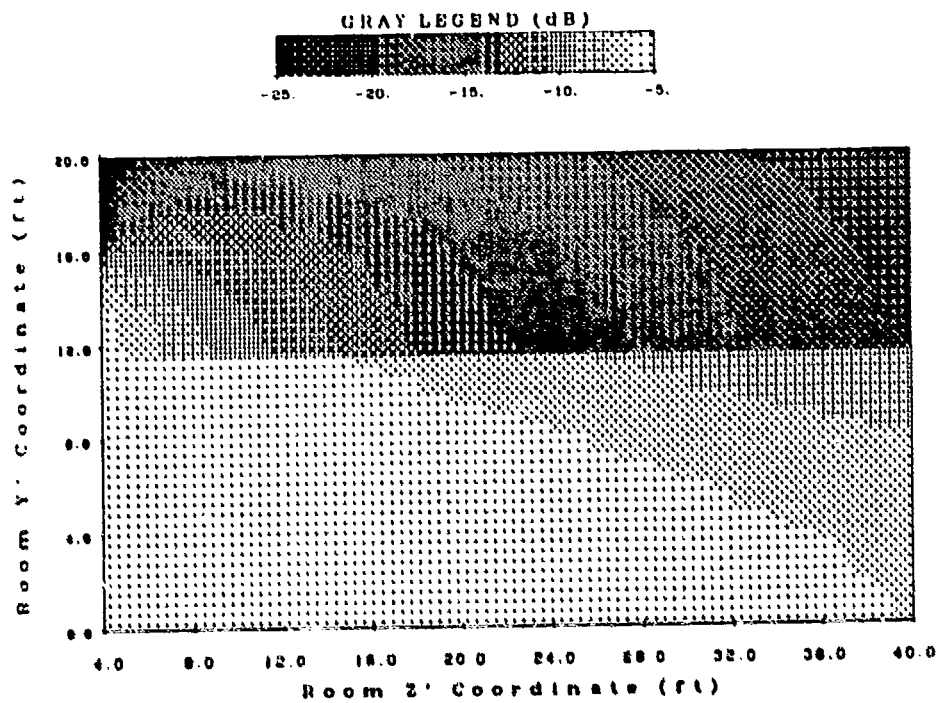


Figure 47: Floor illumination vs. floor  $y'$ ,  $z'$  coordinates. (dB rel. to incident plane wave).

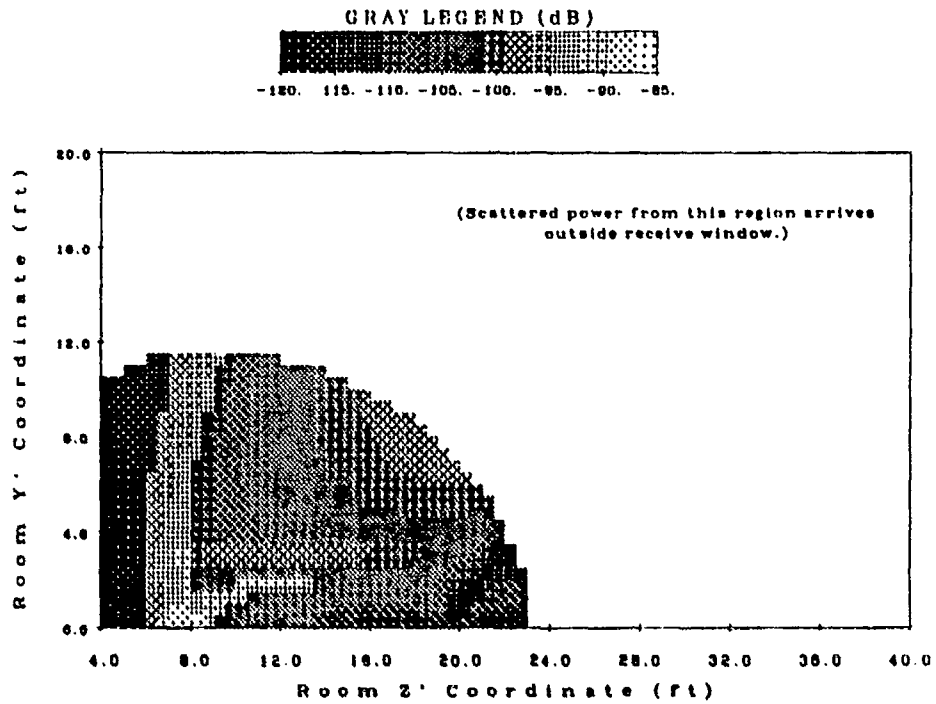


Figure 48: Ceiling scatter vs. ceiling  $y'$ ,  $z'$  coordinates. Test point at (6,0,24). (dB rel. to incident plane wave).

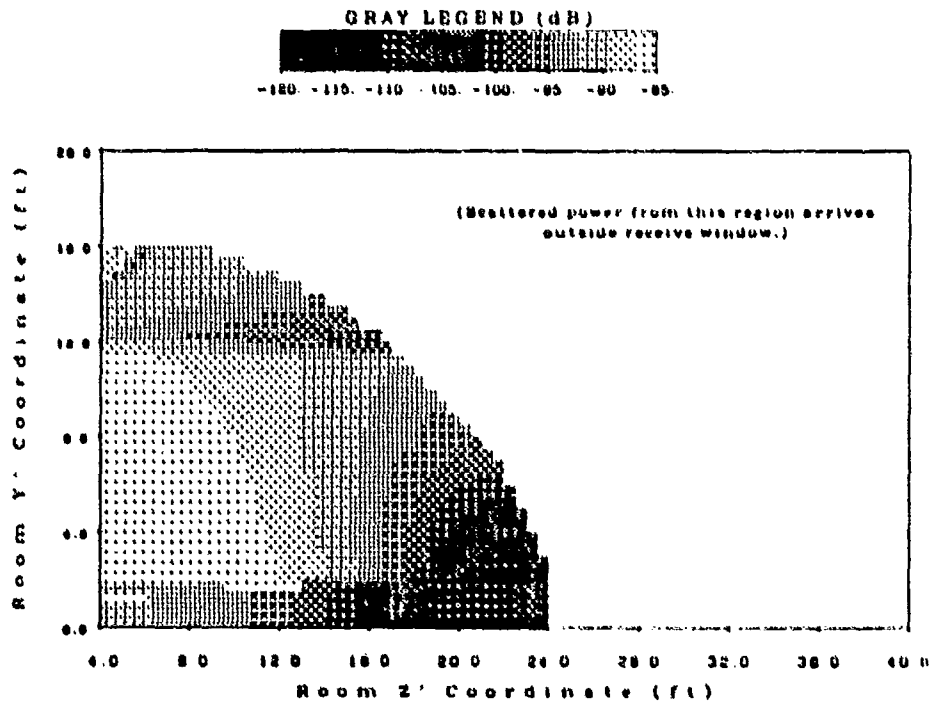


Figure 49: Floor scatter vs. floor  $y'$ ,  $z'$  coordinates. Test point at (6,0,24). (dB rel. to incident plane wave).

Now, consider a configuration identical to the previous one, except that the  $y'$  coordinate of the test point is equal to 5 feet. The test point is thus given in room coordinates as  $(x', y', z') = (6, 5, 24)$  ft. Figures 50 and 51 show the absorber scatter to this test point from the two sides of the ceiling. Figures 52 and 53 show the absorber scatter to this test point from the two sides of the floor. Again, the side walls do not contribute due to the receive window. These plots do, in general, appear as one would expect after having seen the results for the previous case. However, the lower scatter level at roughly  $4 \leq z' \leq 12$  ft,  $3 \leq y' \leq 7$  ft was not expected. The cause was found to be due to the pyramidal scattering angle  $\phi^s$ , which slowly passes through  $270^\circ$  in this region. Edge shadowing and RSB effects cause the Absorber code to predict a decreased scattering level near  $\phi^s = 270^\circ$ . Finally, note that CHAMBER now calculates the total absorber scatter from the ceiling and floor to be  $-67.2$  and  $-56.0$  dB, respectively.

Some conclusions may be drawn at this point. As mentioned earlier, the floor proved to be the dominant scatterer for the chamber configuration considered here. Also, it was seen that the walls were effectively time-gated out in all the cases considered. In Figure 44, the absorber scatter is seen to be fairly constant in the range  $20 \leq z' \leq 28$  feet. (Although not shown here, if one were to consider lower values of  $z'$ , the absorber scatter would be seen to increase as  $z'$  decreases.) Most importantly, note that the absorber scatter levels predicted here are much lower than typical levels of diffraction from the range reflector itself, which are about  $-30$  dB for present designs [13].

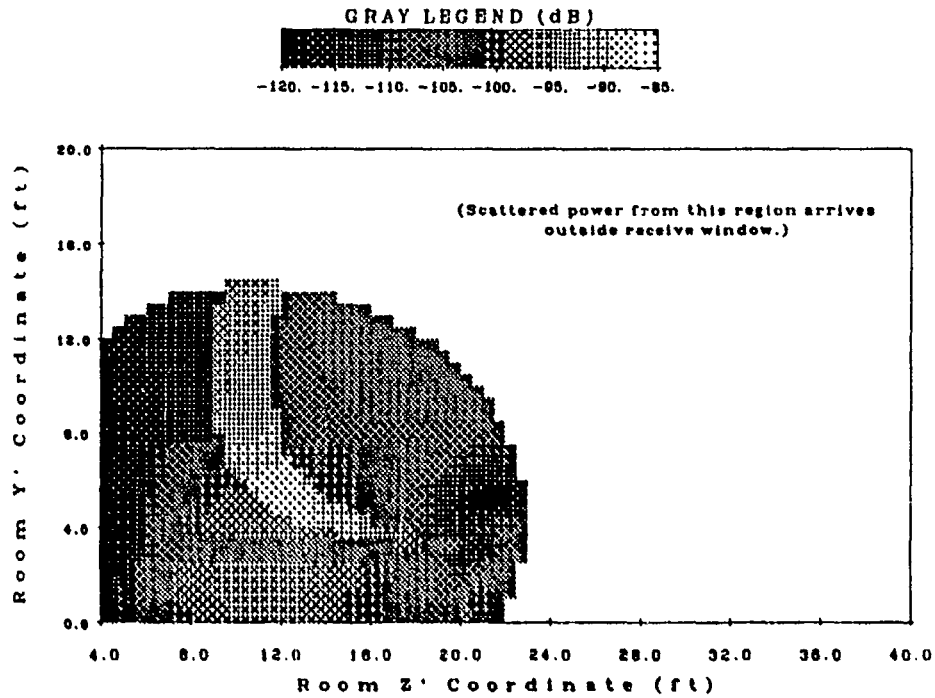


Figure 50: Ceiling scatter vs. ceiling  $y'$ ,  $z'$  coordinates ( $y' > 0$ ). Test point at (6,5,24). (dB rel. to incident plane wave).

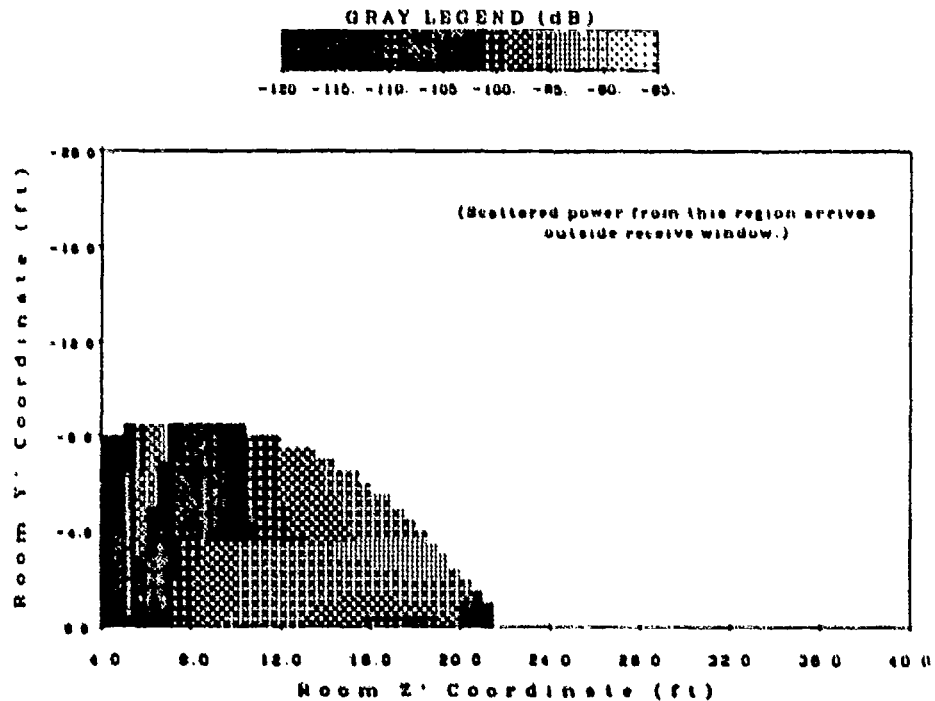


Figure 51: Ceiling scatter vs. ceiling  $y'$ ,  $z'$  coordinates ( $y' < 0$ ). Test point at (6,5,24). (dB rel. to incident plane wave).

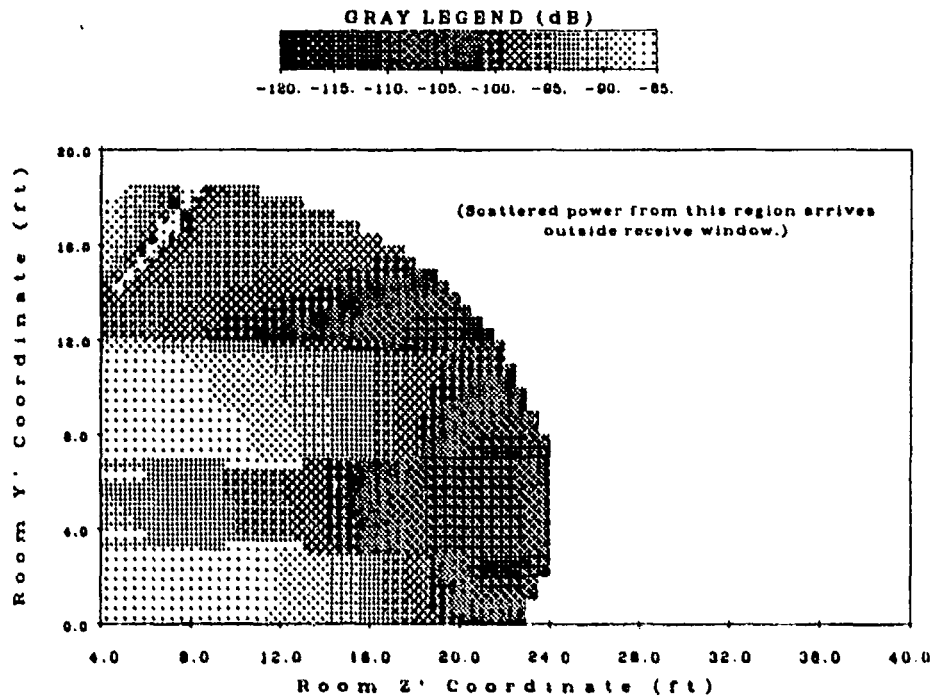


Figure 52: Floor scatter vs. floor  $y'$ ,  $z'$  coordinates ( $y' > 0$ ). Test point at (6,5,24). (dB rel. to incident plane wave).

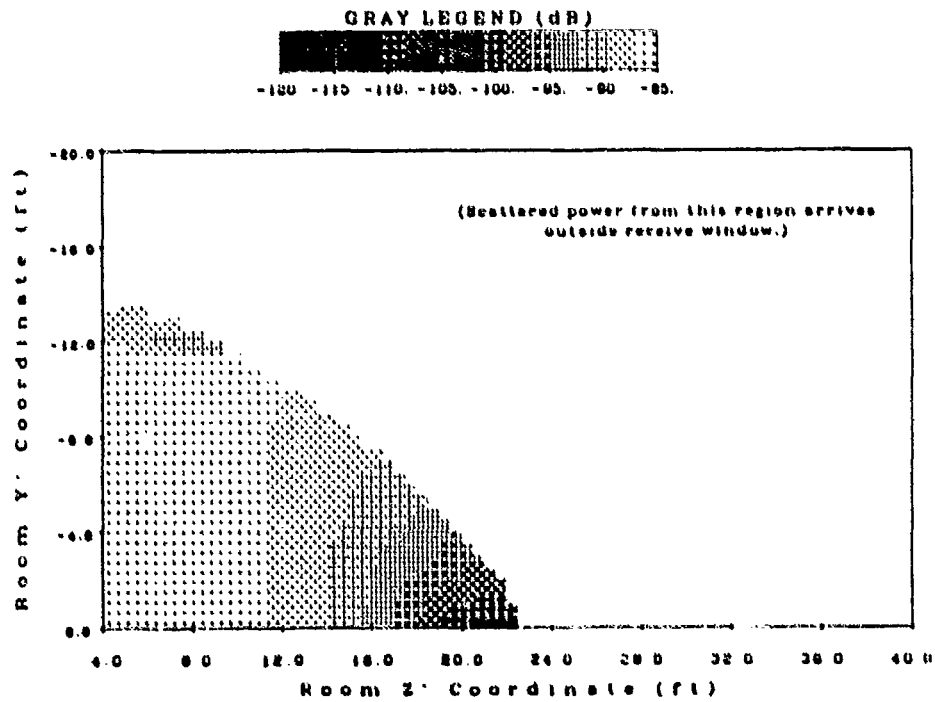


Figure 53: Floor scatter vs. floor  $y'$ ,  $z'$  coordinates ( $y' < 0$ ). Test point at (6,5,24). (dB rel. to incident plane wave).

## CHAPTER VI

### EXPERIMENTAL VERIFICATION OF PYRAMIDAL ABSORBER SCATTERING CALCULATIONS

#### 6.1 Introduction

In this chapter, absorber scattering calculations are verified through comparison with experimental results. Calculations are first compared with backscatter measurements of a single pyramid. Various assumptions on the addition of pyramidal fields are then discussed; these will apply to experiments in which many pyramids contribute to the total scatter. Calculations are then compared against measurements from an experiment in which a large number of pyramids were scattering under the same bistatic situation. Finally, calculations are compared against experimental data in which the bistatic scattering from pyramidal absorber on the ceiling of the OSU compact range was measured.

#### 6.2 Backscatter from a Single Absorber Pyramid

Backscatter measurements of a single pyramid have been made with the OSU compact range using the absorber sample depicted in Figure 54. The rear-facing pyramid served as a second available target, and as a means of balance. Frequency scans were made from 2 to 18 GHz, in 10 MHz increments, for three orientations. Two cases are presented here; these are  $\phi = 0^\circ, \theta = 0^\circ$  and  $\phi = 0^\circ, \theta = 45^\circ$ . The bandlimited impulse response was calculated for the two cases, these are shown

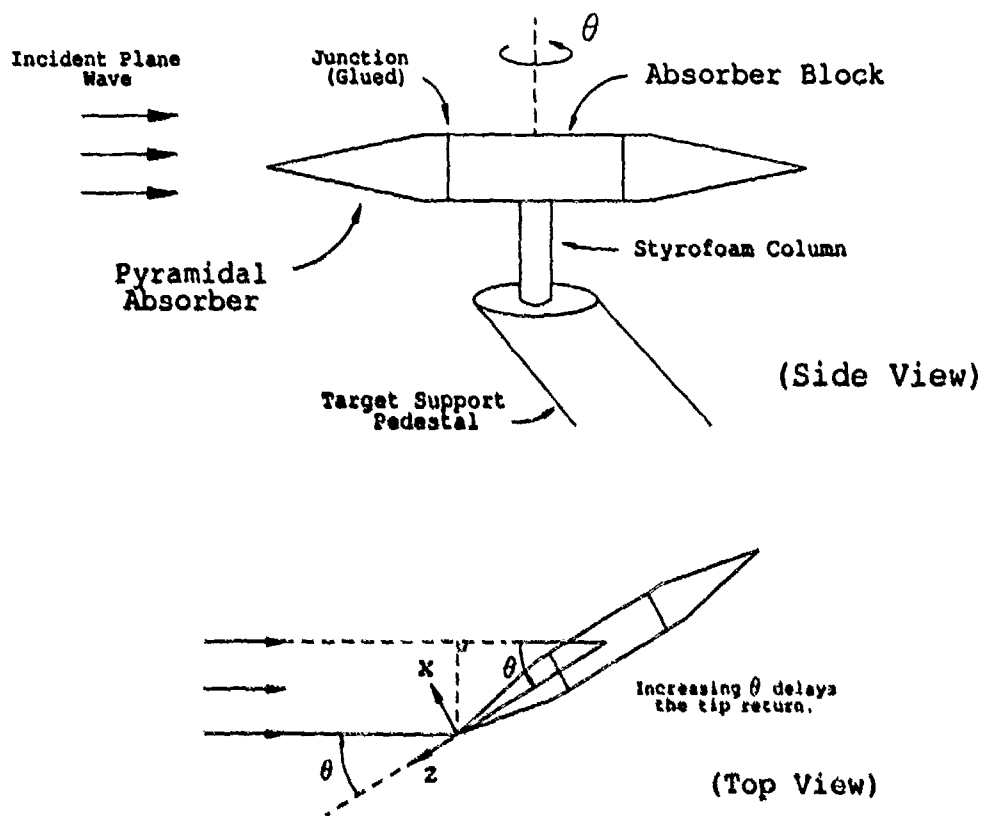


Figure 54: Absorber sample used for single pyramid backscatter measurements.

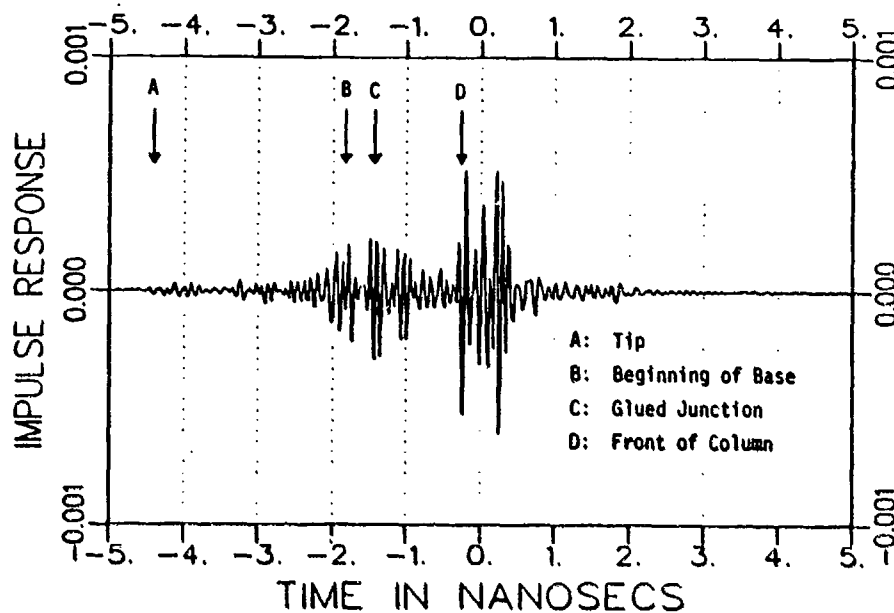


Figure 55: Bandlimited impulse response of single pyramid;  $\phi = 0^\circ$ ,  $\theta = 0^\circ$ .

in Figures 55 and 56, respectively. The expected arrival time of the tip return (-4.4 and -3.1 ns for  $\theta = 0^\circ$  and  $45^\circ$ , respectively) is indicated, along with other scattering centers. (Note that these measurements do not show the relative levels of the tip and base return from a wall of pyramidal absorber, since the geometry of a pyramid isolated in space is entirely different from that of a wall of pyramidal absorber.) The tip return is larger at  $\theta = 45^\circ$  than at  $\theta = 0^\circ$ , which was predicted in Figure 30.

While Figures 55 and 56 do show that the tip response begins at the expected time, it is difficult to tell when it ends. For this reason, the impulse response data was processed further. To emphasize signal and deemphasize noise, the data was squared and then smoothed with a moving Hanning window. The results are presented in Figures 57a and 58a, where the time scale is now from -5 to -2 ns. The expected time of the tip response is again indicated in the figures.

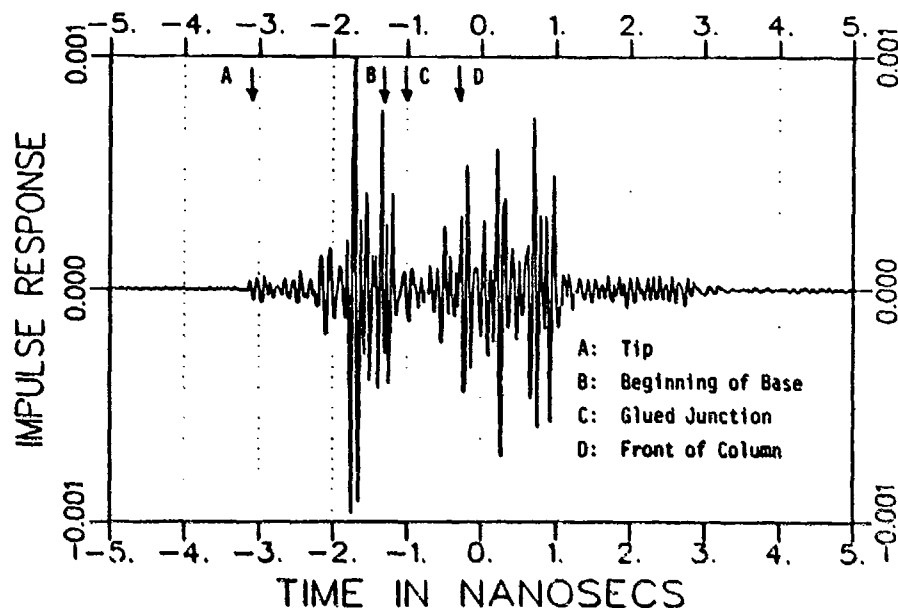
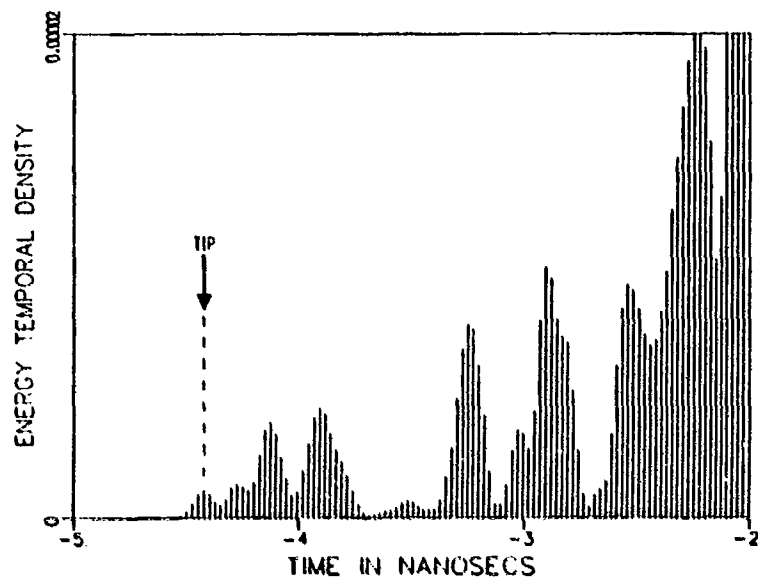


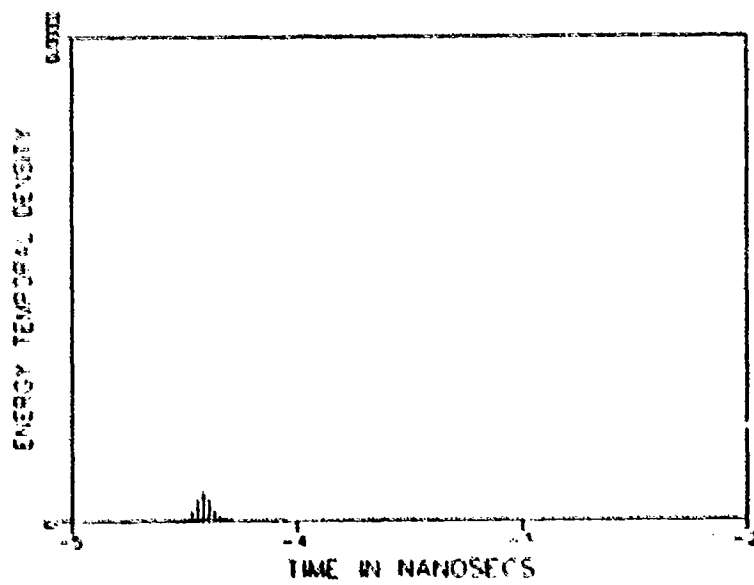
Figure 56: Bandlimited impulse response of single pyramid;  $\phi = 0^\circ$ ,  $\theta = 45^\circ$ .

(Note that in Figure 58a, the tip response appears centered at  $-2.9$  ns, which corresponds to  $\theta \cong 48^\circ$ . This deviation is assumed to be due to the method used for target alignment, which was believed accurate to within only a few degrees. Of course, a small angular error would noticeably affect the tip response time for  $\theta = 45^\circ$ , but not for  $\theta = 0^\circ$ .) Now, one can visually isolate the tip return and choose appropriate time gate parameters. This has been done using a Kaiser-Bessel window; Figures 57b and 58b show the gated waveforms.

These plots of energy temporal density were considered solely to find appropriate time gate parameters. Going back to our calibrated frequency domain measurements, one can perform an inverse Fourier transform (where, of course, the frequency domain data is *not* windowed before the IFT), and apply the proper time gate parameters to the two time domain signals. Finally, an FFT generates the tip response in the frequency domain which is plotted against calculations in

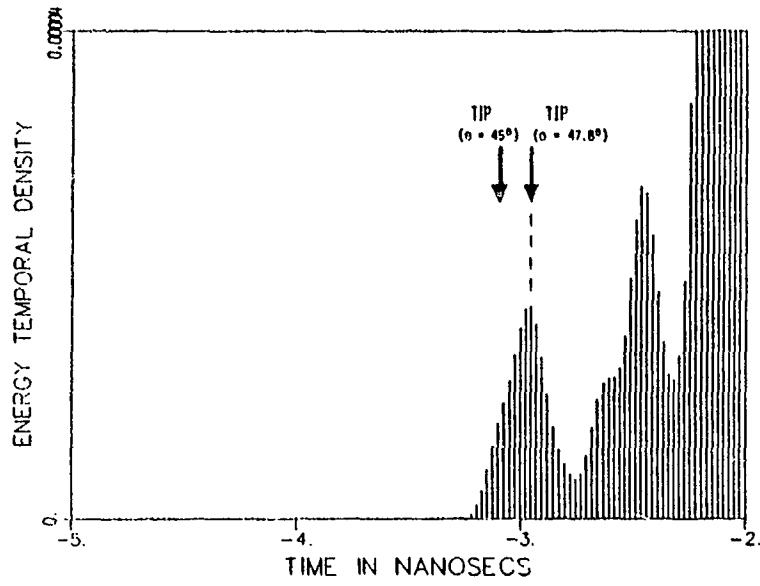


a) Total Response

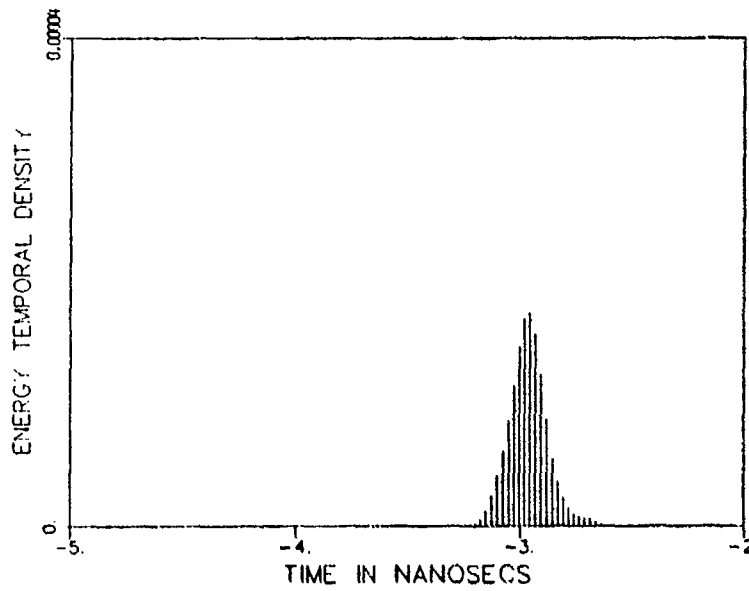


b) Gated Response

Figure 57: Energy temporal density of single pyramid;  $\phi = 0^\circ$ ,  $\theta = 0^\circ$ .



a) Total Response



b) Gated Response

Figure 58: Energy temporal density of single pyramid;  $\phi = 0^\circ$ ,  $\theta = 45^\circ$ .

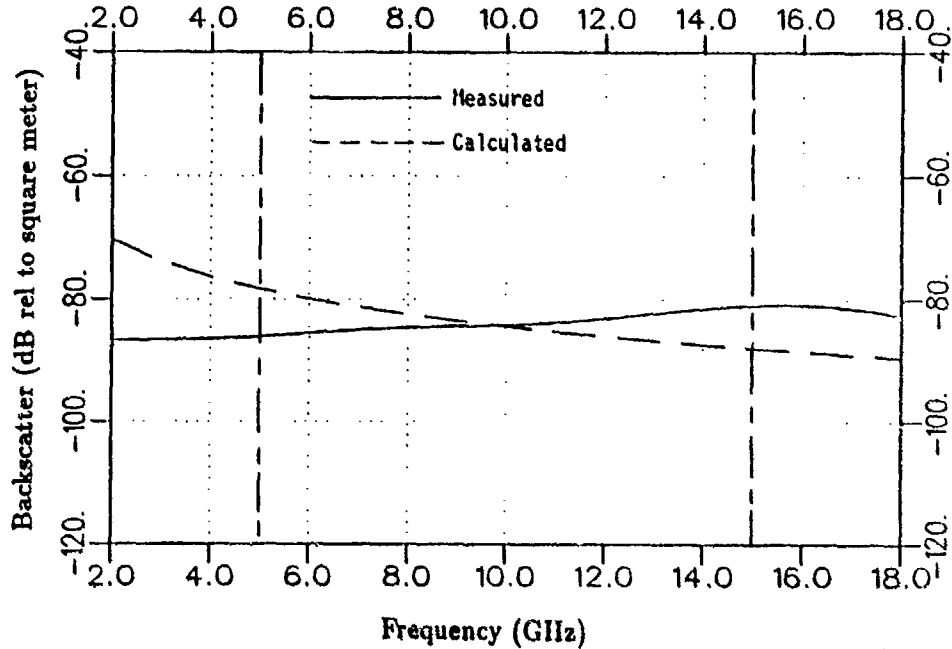


Figure 59: Calculated vs. measured backscatter from a single pyramid;  $\phi = 0^\circ$ ,  $\theta = 0^\circ$ .

Figures 59 and 60 for  $\theta = 0^\circ$  and  $\theta = 45^\circ$ , respectively. In each figure, vertical dashed lines indicate the range of valid experimental data, due to the processing performed. The measurements show that the scattered signal level of the tip is roughly that predicted by theory. Better agreement can not be expected, since the very narrow time gates used limit the frequency resolution; in addition, the tip return is a very weak signal being measured in the presence of much stronger signals.

### 6.3 Comments on Addition of Pyramidal Fields and Effective RCS

Up to this point, the questions of how the fields from a large number of pyramids add to produce a total field, or of how an "effective RCS" should be defined have not arisen. In Chapter V, it was decided to treat the pyramidal absorber in the

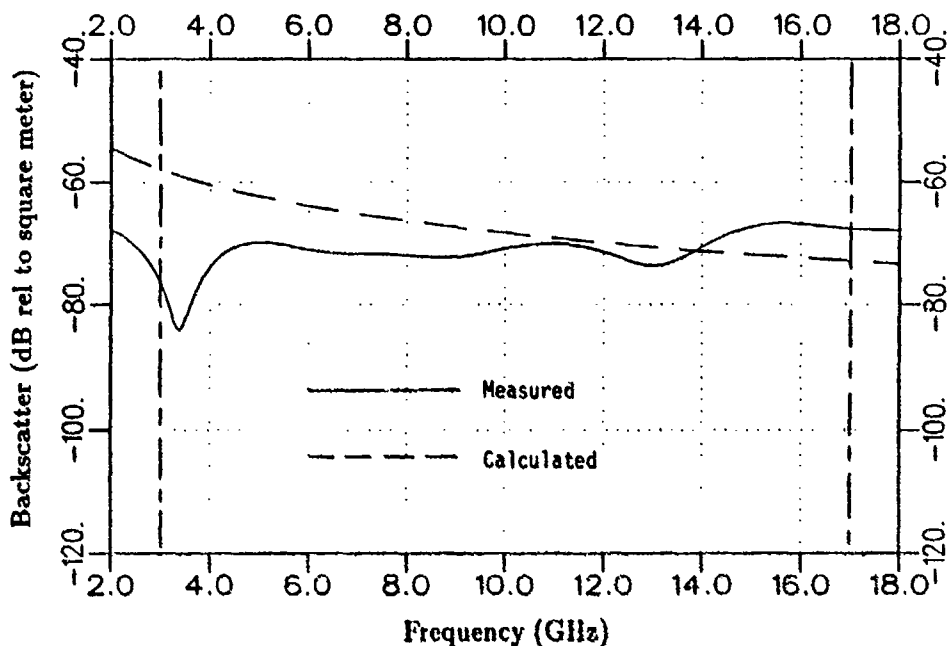


Figure 60: Calculated vs. measured backscatter from a single pyramid;  $\phi = 0^\circ$ ,  $\theta = 45^\circ$ .

chamber as an incoherent scatterer. Thus, the values of power found from various grid points were simply summed (and normalized) to produce the total scattered power. In the previous section, the true RCS of a single absorber pyramid was measured; thus, the corresponding calculations were straightforward. However, the experiments described in the following two sections involve the scattering from a large number of absorber pyramids. Neither is a true RCS measurement. Both involve the question of how the fields of individual pyramids add to produce the total field. For these reasons, the topics of pyramidal field addition and effective RCS will be discussed now.

First, let us consider a few cases in which  $N$  pyramids are each illuminated by the same field  $E^i$ , and each scatters the same field  $E^{tip\ scat}$ , to some observation point. Let the total scattered field be denoted by  $E^{total\ scat}$ . An "effective RCS",

$\sigma_{eff}$ , is then defined as

$$\sigma_{eff} = 10 \log \left( 4\pi r^2 \left| \frac{\mathbf{E}^{total\ scat}}{\mathbf{E}^i} \right|^2 \right) \quad (6.1)$$

where  $r$  is the distance from the tips to the observation point. If one assumes that the  $N$  fields  $\mathbf{E}^{tip\ scat}$  add in phase to produce  $\mathbf{E}^{total\ scat}$ , that is

$$\mathbf{E}^{total\ scat} = N \mathbf{E}^{tip\ scat} \quad (6.2)$$

then it follows that

$$\sigma_{eff} = 10 \log \left( 4\pi r^2 \left| \frac{\mathbf{E}^{tip\ scat}}{\mathbf{E}^i} \right|^2 \right) + 20 \log N \quad (6.3)$$

On the other hand, if one assumes that the  $N$  fields  $\mathbf{E}^{tip\ scat}$  add in power to produce  $\mathbf{E}^{total\ scat}$ , that is

$$|\mathbf{E}^{total\ scat}|^2 = N |\mathbf{E}^{tip\ scat}|^2 \quad (6.4)$$

then it follows that

$$\sigma_{eff} = 10 \log \left( 4\pi r^2 \left| \frac{\mathbf{E}^{tip\ scat}}{\mathbf{E}^i} \right|^2 \right) + 10 \log N \quad (6.5)$$

Note that the assumption of field addition affects only the  $\log N$  term. One may want to base the assumption of field addition on an actual measurement of pyramid tip position. In [7], the height of each pyramid on an absorber block of 36 pyramids was measured. Deviations as much as 1 cm were observed. Using these measurements, and assuming nose-on plane wave incidence, one can find the relative phase of the tip scattered fields. The magnitude of the sum field,  $S_r$ , was then computed as follows [7]

$$S_r = \sum_{i=1}^{36} e^{-j2k_0 d_i} \quad (6.6)$$

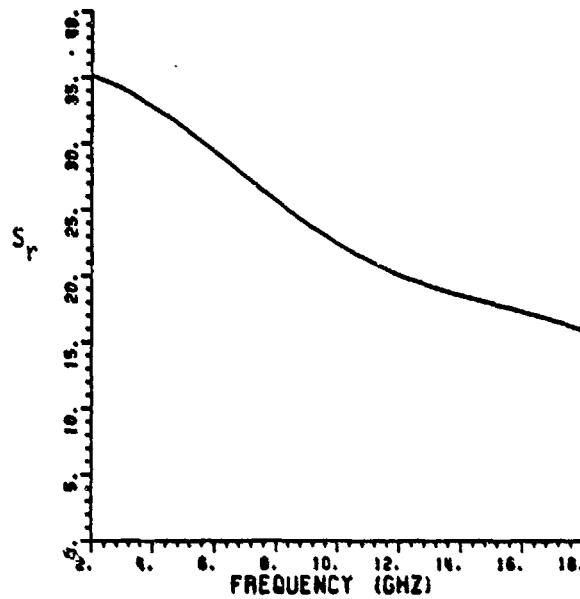


Figure 61: Magnitude ( $S_r$ ) of sum of fields from an absorber block vs. frequency [7].

where  $a_i$  is the height of the  $i^{th}$  pyramid,  $k_0$  is the wavenumber of free space, and each pyramidal scattered field has a magnitude of unity. The results (from one block) are shown in Figure 61, which plots the magnitude of the sum field,  $S_r$ , versus frequency. Phase addition corresponds to the total field being 36 times the field of a single pyramid ( $S_r = 36$ ), while power addition corresponds to the total field being 6 times the field of a single pyramid ( $S_r = 6$ ). At the lower frequencies, the curve approaches a value of 36, as tip height deviation becomes a negligible fraction of a wavelength. Now, this data will be used to appropriately modify the  $\log N$  term of Equation (6.3). A normalization constant is needed, since the data in Figure 61 was found for a block of 36 pyramids. The resulting expression for effective scattering is given by

$$\sigma_{eff} = 10 \log \left( 4\pi r^2 \left| \frac{\mathbf{E}^{tip\ scat}}{\mathbf{E}^i} \right|^2 \right) + 20 \left( \frac{\log S_r}{\log 36} \right) \log N . \quad (6.7)$$

(This discussion simply serves as an example. If one were to take this approach, tip position measurements of the material in question should be made.)

Now, let us consider several blocks of absorber. Again, assume that each pyramid is illuminated by the same field  $\mathbf{E}^i$ , and that each scatters the same field,  $\mathbf{E}^{tip\ scat}$ , to some observation point. The total scattered field produced by these pyramidal fields is again denoted by  $\mathbf{E}^{total\ scat}$ . Since absorber blocks tend to be misaligned relative to each other, it is assumed that the total fields of the absorber blocks add in power with each other. However, on the matter of the addition of pyramidal fields *within* each block, three assumptions are made:

1. Addition in power.
2. Addition in phase.
3. Addition according to tip height measurements.

Thus, consider  $M$  blocks of absorber, each with  $N$  pyramids. Under the first assumption, one finds that

$$\sigma_{eff} = 10 \log \left( 4\pi r^2 \left| \frac{\mathbf{E}^{tip\ scat}}{\mathbf{E}^i} \right|^2 \right) + 10 \log(MN) \quad (6.8)$$

while under the second assumption

$$\sigma_{eff} = 10 \log \left( 4\pi r^2 \left| \frac{\mathbf{E}^{tip\ scat}}{\mathbf{E}^i} \right|^2 \right) + 10 \log(MN^2) \quad (6.9)$$

and under the third assumption

$$\sigma_{eff} = 10 \log \left( 4\pi r^2 \left| \frac{\mathbf{E}^{tip\ scat}}{\mathbf{E}^i} \right|^2 \right) + 10 \log \left( MN \left\{ \frac{\log S_r}{\log 6} \right\} \right) . \quad (6.10)$$

Note that Equations (6.8) and (6.9) are special cases of Equation (6.10).

Before leaving this topic, Equation (6.10) will be rewritten for the more general case in which the number of pyramids may vary from block to block. Thus, for  $M$  blocks of absorber, each with  $N_i$  pyramids, the effective RCS (under our third assumption) is written as

$$\sigma_{eff} = 10 \log \left( 4\pi r^2 \left| \frac{\mathbf{E}^{tip\ scat}}{\mathbf{E}^i} \right|^2 \right) + 10 \log \left( \sum_{i=1}^M N_i \left\{ \frac{\log S_r}{\log 6} \right\} \right) . \quad (6.11)$$

This equation applies to the experiment in the next section.

Note that a major restriction to all of the cases considered in this section was that of the incident and scattered fields being the same for all pyramids. In an experiment which measures the absorber scattering in a compact range chamber, this will clearly not be the case. When one is interested in computing the absorber scatter to a specific test point (as was done in CHAMBER), the  $|\mathbf{E}^{total\ scat}|^2$  term in Equation (6.1) can be taken to represent the total scattered power. However, since each pyramid is illuminated differently, there is no obvious interpretation of the  $|\mathbf{E}^i|^2$  term. Fortunately, one does not encounter this difficulty in CHAMBER, since only the scattered power computations are examined. However, the calculations in Section 6.5 force one to consider again the notion of an effective RCS. This results from the nature of the experiment considered in that section, however, and is best explained there.

#### 6.4 Bistatic Scattering from a Wall of Pyramidal Absorber

In [7], an experiment is described in which two 3' diameter parabolic dish antennas were used to measure the bistatic scattering from a wall of pyramidal absorber. The wall absorber consisted of 8" tall pyramids. The two antennas had broadband TEM horn feeds at their focii. The transmitter produced a vertically-

polarized electric field. The experimental setup is depicted in Figure 62. The transmitting antenna was positioned at an angle of  $45^\circ$  relative to the wall, while the receiver was positioned at a variety of angles. It was assumed that the wall was in the near field of both antennas. Thus, an elliptical region (of about 10 sq ft) of the wall is assumed to be illuminated by a plane wave. The receiver location specified by  $\phi^s = 45^\circ$  is of most interest. At this angle, all illuminated pyramids have (ideally) identical incidence and scattering angles, and identical phase paths from the transmitting horn to the receiving horn. Thus, depending on how much variation exists in tip positions, one may expect the scattered fields of the pyramids within each absorber block to add in power, in phase, or somewhere in between. (Of course, the pyramid fields could interfere with one another and produce a total field less than that predicted by an adding in power calculation. This behavior would produce nulls at certain frequencies. However, the power addition is considered the lower limit in our calculations.)

Since each absorber block on the wall measures  $2' \times 2'$ , a different number of pyramids are illuminated on each of a few absorber blocks. The three assumptions of field addition from Section 6.3 will be used for pyramid fields within each absorber block, while the total scattered fields of the various blocks are assumed to add in power.

Figure 63 shows the bandlimited impulse response for the wall scatter. The location of the expected time of the tip and base returns is indicated. Next, Figure 64 shows the corresponding frequency domain data. The measured data is taken from [7], while the calculations were made using the Absorber code developed here. Equation (6.11) is used to find the three calculated curves; this is done by specifying  $S_r = 6$  for power addition,  $S_r = 36$  for phase addition, and using  $S_r(f)$  from Figure 61 for addition according to tip height deviation (assumption 3). The

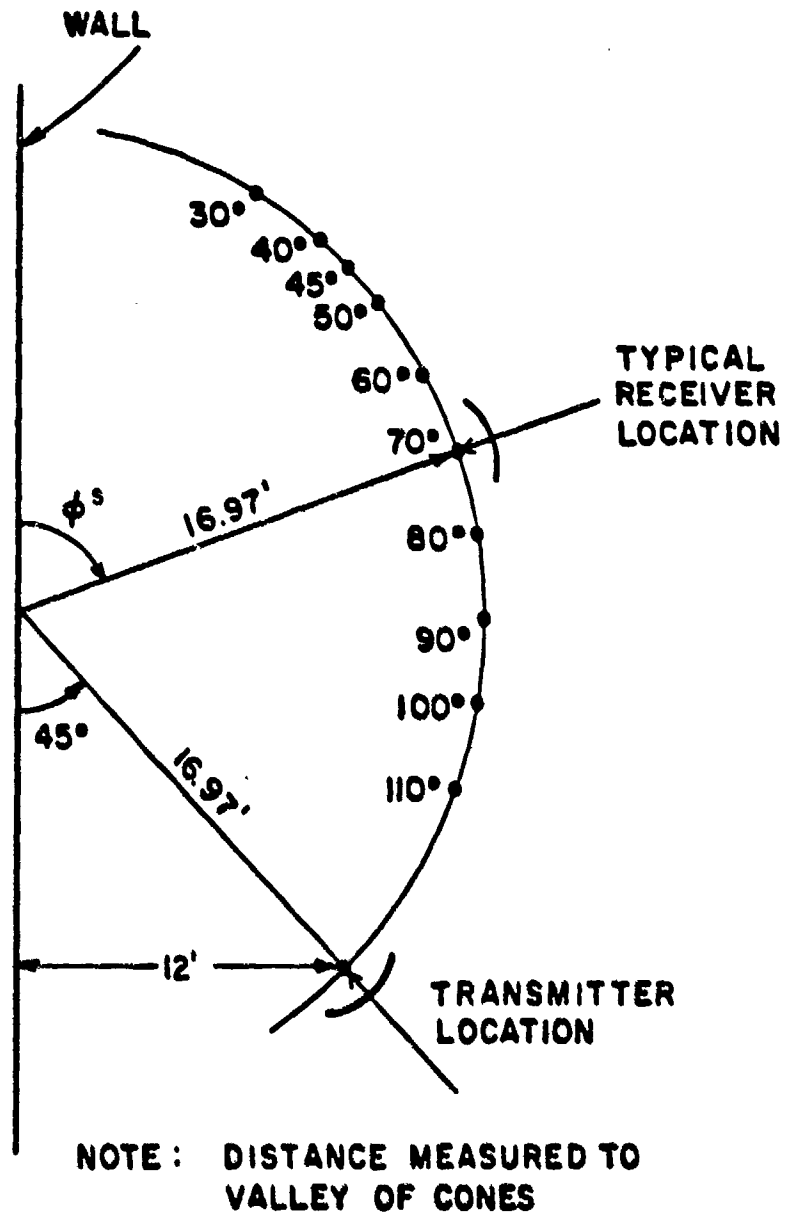


Figure 62: Experimental setup of bistatic absorber wall scatter measurement [7].

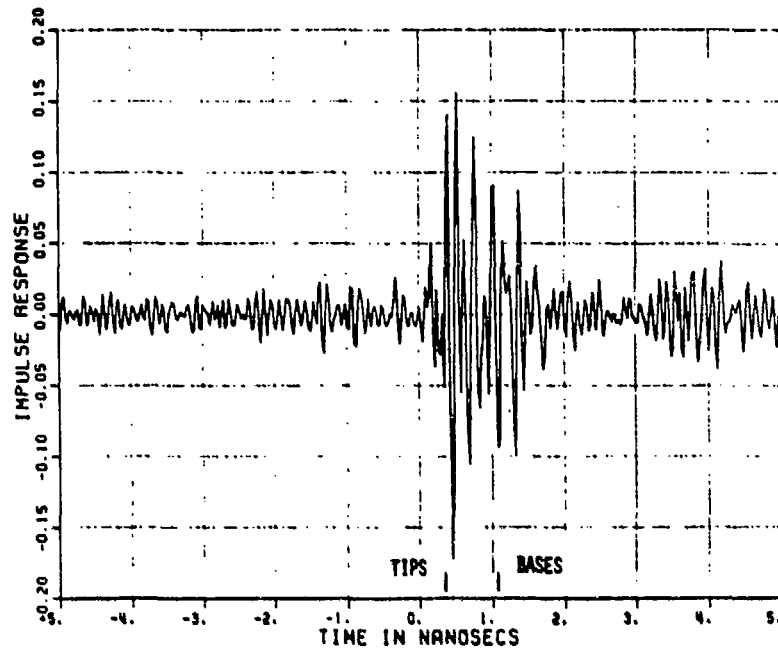


Figure 63: Bandlimited impulse response of wall scatter measurement [7].

third assumption agrees best with the measured data. Note that the measurements include both tip and base response. Although tip diffraction calculations are being plotted against measurements of both tip and base return, recall that the tip return is believed to be the dominant scatterer. Figure 63 supports this contention.

### 6.5 Ceiling Absorber Scattering in a Compact Range Chamber

The absorber scattering from a portion of the ceiling of the OSU compact range has been measured by means of a large flat plate placed in the target zone. This work was the effort of Young and Clerici and is described in [14]. The plate measures 6' x 6' and can be rotated in azimuth and elevation. The experimental setup is depicted in Figure 65. As indicated in the figure, the plate is assumed to optically reflect the incident plane wave up toward the ceiling. (This represents an extreme case of absorber illumination in that the ceiling absorber just above

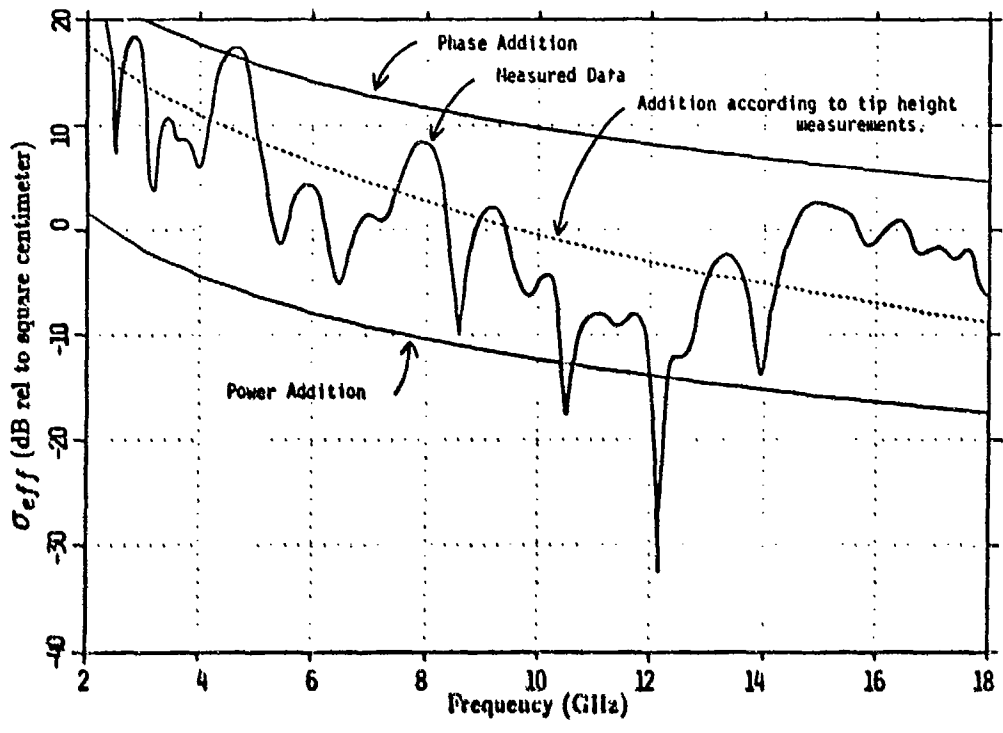


Figure 64: Comparison of frequency domain data versus calculations, wall scatter experiment (experimental data from [7]).

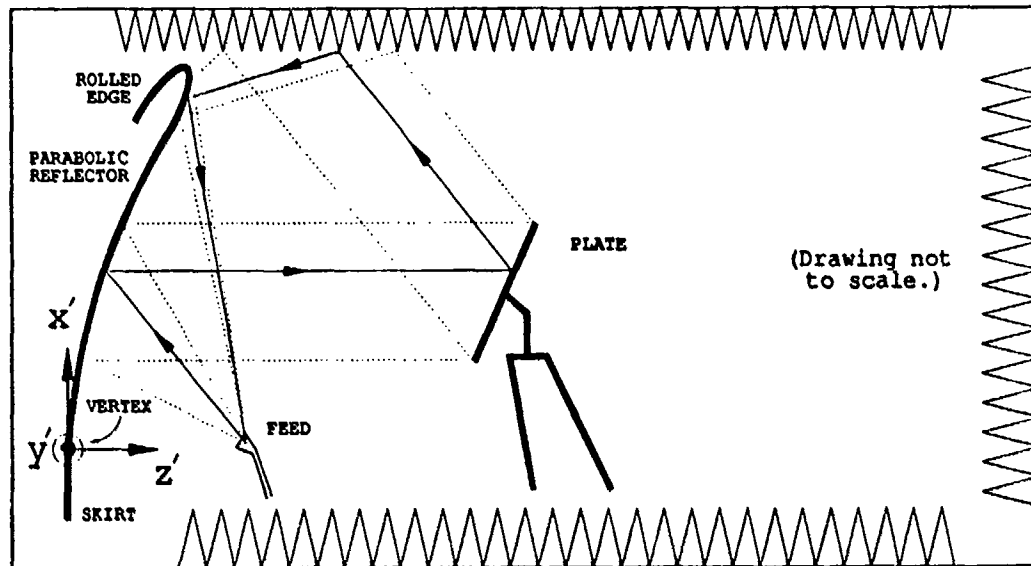


Figure 65: Experimental setup used for Plate measurements.

the reflector is illuminated by the incident plane wave.) The ceiling pyramids then scatter in all directions. Some of the scattered energy will strike the rolled edge and be reflected back to the feed. This is the absorber scatter signal under consideration.

The experiment considered here used a plate azimuth angle of  $0^\circ$ , and a plate elevation angle of  $73^\circ$ . This corresponds to a patch of ceiling 6 feet wide and 6.3 feet downrange. (The patch is actually 10.3 feet in extent downrange, but the last 4 feet are lined with wedge absorber material. The wedge material is not believed to scatter significantly in the direction that would affect this experiment.)

Note that during calibration, the range normally computes the following

$$\sigma = 10 \log \left( 4\pi r^2 \left| \frac{E^s}{E^i} \right|^2 \right) \quad (6.12)$$

where  $E^i$  represents the incident plane wave and  $E^s$  is the scattered field from

some target in the target zone. In this experiment, the range will receive and process our ceiling absorber signal as though it had originated from a target in the target zone. Thus, when the ceiling absorber signal is properly time-gated, the range computes

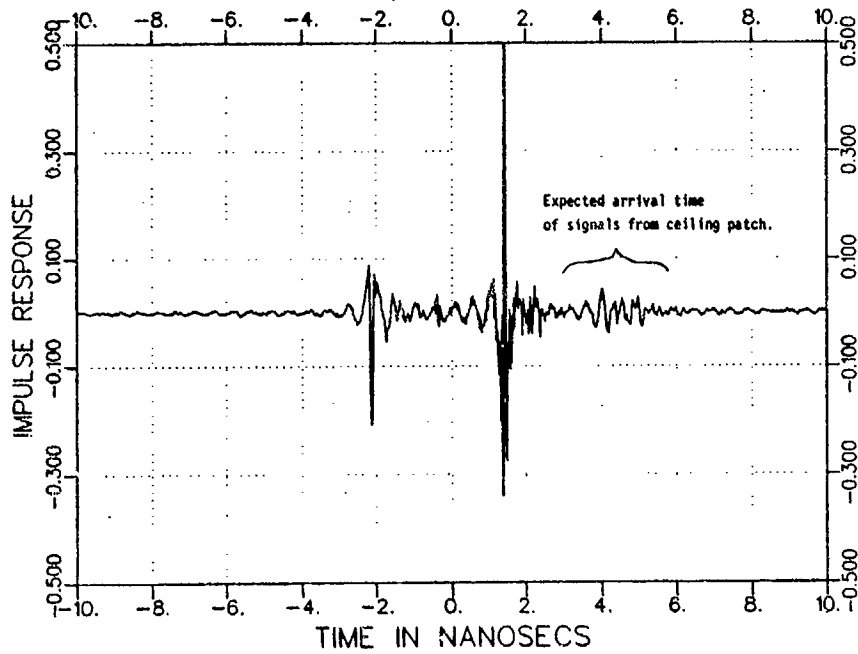
$$\sigma_{ceil} = 10 \log \left( 4\pi r^2 \left| \frac{\mathbf{E}^{ceil\ scat}}{\mathbf{E}^i} \right|^2 \right) \quad (6.13)$$

where  $\mathbf{E}^i$  again represents the incident plane wave, and  $|\mathbf{E}^{ceil\ scat}|^2$  represents the total scattered power of the ceiling absorber signal.

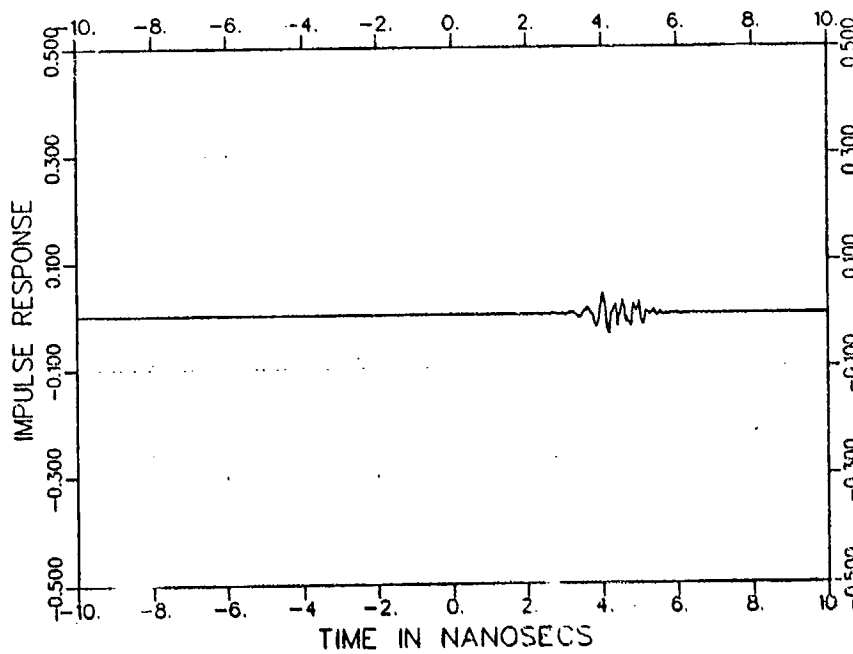
Figures 66a and 67a show the bandlimited impulse response for the cases of vertical and horizontal polarization, respectively. The absorber response, based on timing calculations, is indicated. A Kaiser-Bessel window was then applied in each case, Figures 66b and 67b show the gated impulse response for the two cases. Next, an FFT was performed. Figure 68 shows the resulting absorber response in the frequency domain, along with three calculated curves. In these three cases,  $\sigma_{ceil}$  is calculated via Equation (6.13), where  $|\mathbf{E}^{ceil\ scat}|^2$  is found under three assumptions of field addition. The lowest of the calculated curves was found assuming the fields from all tips added in power. The middle curve was calculated assuming the fields from tips within one square foot sections added in phase, while fields among sections added in power. The upper curve was calculated assuming the fields from tips within four square foot sections added in phase, while fields among sections added in power. The results are very satisfying, since they roughly predict the scattering level from the ceiling patch, and since they follow the frequency behavior of the measurements as well.

(Note that, by reciprocity, equivalent scattering paths exist which are the reverse of those shown in Figure 65. These were the paths actually considered

when the ceiling scatter calculations were made. This was done by a computer code similar to CHAMBER.)

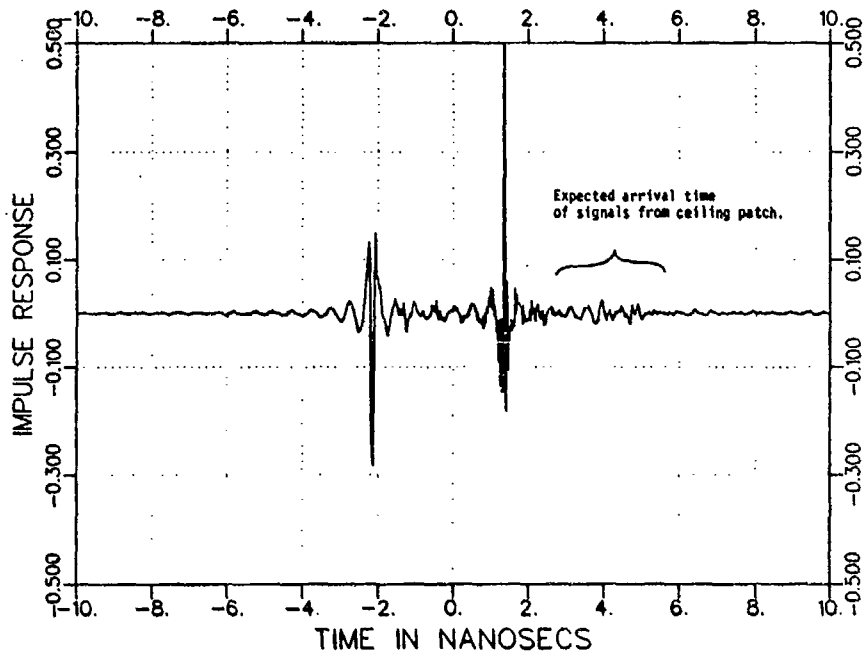


a) Total Response

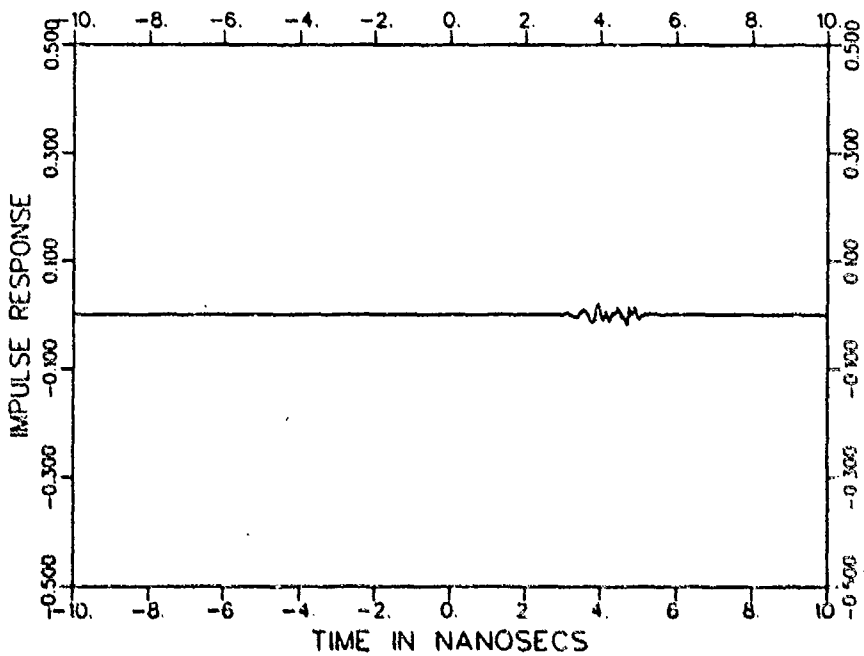


b) Gated Response

Figure 66: Bandlimited impulse response of Plate experiment, vertical polarization.

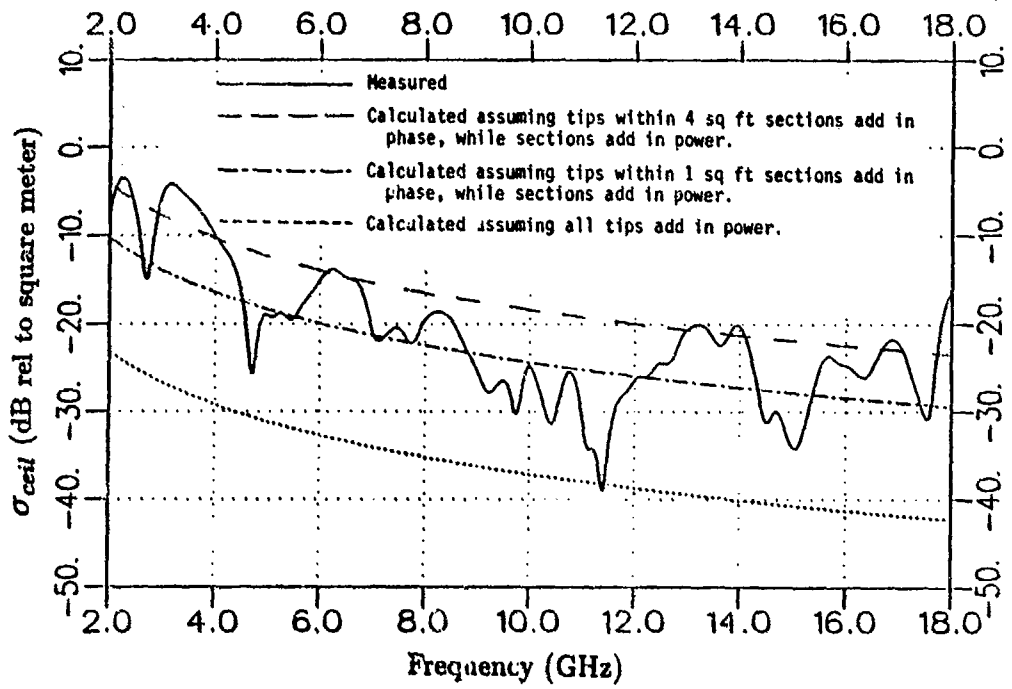


a) Total Response

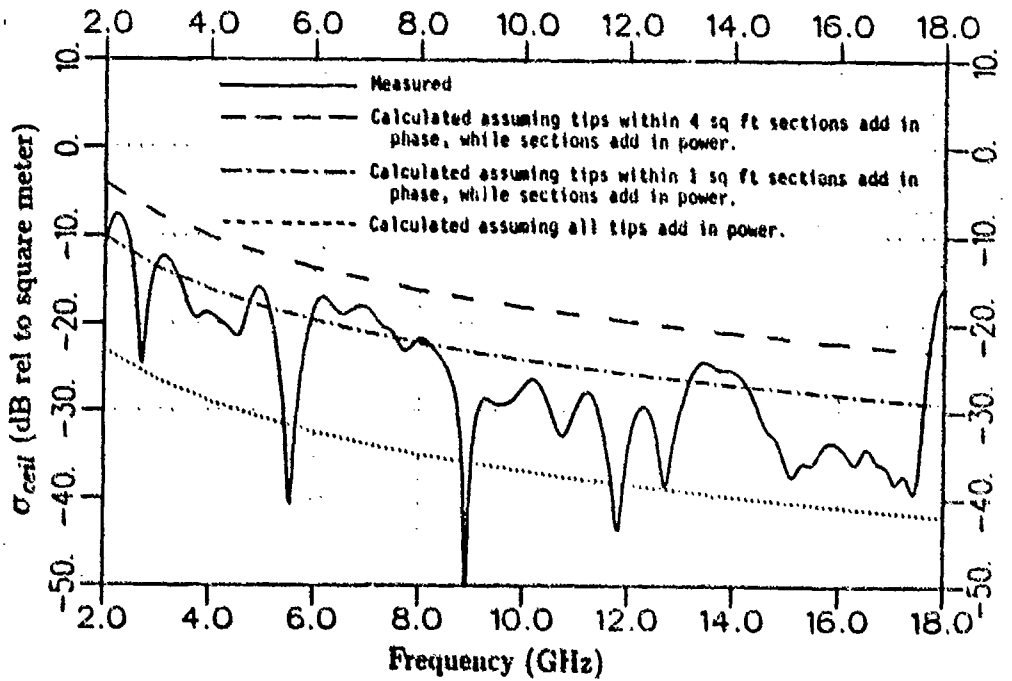


b) Gated Response

Figure 67: Bandlimited impulse response of Plate experiment, horizontal polarization.



a) Vertical Polarization.



b) Horizontal Polarization.

Figure 68: Calculations vs. measurements of ceiling absorber scatter ( $\sigma_{ceil}$ ).

## CHAPTER VII

### SUMMARY AND CONCLUSIONS

A high frequency diffraction solution for the scattered fields from a pyramidal absorber tip has been developed in this study. This solution is based on the perfectly-conducting UTD corner diffraction solution, which was modified to treat the case of a corner in a dielectric three-dimensional wedge. The modification is modeled after that done in [7] for the two-dimensional dielectric wedge. The resulting formulation was then used to generate a computer code for the calculation of bistatic scattering from an absorber pyramid. The validity of this result has been verified by comparisons with backscatter measurements of an isolated pyramidal absorber tip. Note that the tip term was extracted from the measured result by transforming the frequency domain data to the time domain and gating out the appropriate term. The calculated and measured results don't overlay, but have similar levels. One should not expect perfect agreement in that dielectric materials have many potential error terms, such as variation of dielectric properties with frequency and position. Also, the tip term is a very small signal which was measured in the presence of much larger signals. Nevertheless, the measured results do tend to verify the theoretical solution.

The validity of the absorber scattering code was also verified by comparisons with bistatic measurements of an absorber wall. This displayed excellent agreement between calculation and measurements. The calculations made under the assump-

tions of power and phase addition (of fields from individual pyramids) bounded the measured data well. The calculated curve which computed pyramidal field addition based on tip height measurements agreed with both the level and frequency dependence of the measured data.

The pyramidal absorber tip solution was then used to develop an anechoic chamber analysis for compact range applications. This computer code, CHAMBER, determines the total field scattered into the test zone by the absorber lining the chamber walls, ceiling, and floor. (Note that CHAMBER obtains the illumination of the absorber from a reflector analysis code which treats a semi-circular reflector with a rolled edge and a skirt.)

A specialized version of CHAMBER was used to compute absorber scatter from the ceiling of the Ohio State University compact range chamber. Comparisons of these calculations against measurements from the plate experiment of Chapter VI illustrate the accuracy of our predictions.

CHAMBER has been used to analyze the Ohio State University compact range chamber. The analysis showed that the dominant scattering came from the absorber on the floor, which was strongly illuminated by the skirt. The wall absorber scattering did not arrive within the specified receive window, for cases where the test point was along the room centerline. One should note that the fall time and isolation of the receive window deserve careful attention, since the scattered power (into the target zone) from the floor and ceiling absorber increases as the scatter point nears the back of the room. (This can be seen by running CHAMBER with the duration of the receive window extended.) Most significantly, though, the absorber scatter levels predicted here are much lower than typical levels of diffraction from the range reflector itself, which are about  $-30$  dB (relative to the incident plane wave) for present designs.

With this code, one can predict the pyramidal absorber performance of a compact range chamber before it is constructed. In fact, the various hot spots within the room can be identified so that appropriate action can be taken.

## APPENDIX A

### PROGRAM CHAMBER

#### A.1 Introduction

This appendix begins with a description of files required to compile, link, and run program CHAMBER. The reader is then stepped through the operation of CHAMBER, and the output generated is described. Finally, some possible error messages will be discussed.

#### A.2 Software Requirements

The FORTRAN code for program CHAMBER is separated into two files, CHAMBER.FOR and CH\_DECL.FOR. The former contains the bulk of the code; namely, the main program and subroutines. The latter simply maintains the variable declaration statements and common blocks. CHAMBER.FOR inserts CH\_DECL.FOR wherever necessary with the "include" command. Thus, the file CH\_DECL.FOR must be present when compiling CHAMBER.FOR.

CHAMBER also uses the following subroutines: GEOMETRY, BISTATIC, REFL.CODE, and PLOTTER. Subroutines GEOMETRY and BISTATIC make up what has previously been referred to as the Absorber code. Given a specified pyramid angle,  $\alpha$ , subroutine GEOMETRY computes the pyramid wedge angle, edge-fixed coordinate systems, and so on. It passes this information to subroutine BISTATIC, which can then make repeated scattering computations. Of course,

this is transparent to the user of CHAMBER. These subroutines are both in file TIPBIST.FOR. Next, subroutine REFL.CODE is the modified version of the Semi-Circular Compact Range Reflector Code [9] that has been mentioned earlier. The modifications primarily consist of conversion from a program to a subroutine, and the elimination of all but the GO field. Also, the coordinates of every observation point and corresponding reflection point on the reflector have been added to the output. Again, this is transparent to the user. File REF3DT.SUB contains subroutine REFL.CODE. Subroutine PLOTTER creates the plots output by CHAMBER, and is in a file by the same name.

Finally, when running CHAMBER, two data files must be present. These are CH\_INPUT.DAT and FOR017.DAT. The former holds the input data that will be used in the run of CHAMBER. To specify the input, one must edit this file. This is more convenient than entering the input interactively, especially for multiple runs where only a few variables change. File FOR017.DAT contains the cross-section information of the semi-circular reflector, which is used by subroutine REFL.CODE. File FOR017.DAT is created by program SURFACE, which in turn requires file FOR070.DAT as input. (Note that some data specified in file FOR070.DAT must later be input directly to the reflector code; thus, one must be careful to be consistent.) The reader is referred to [9] for a more complete discussion of this material; however, the FOR070.DAT file that created the FOR017.DAT file used in the sample calculations of Chapter V is as follows:

```
1.  
12.  
11.5  
0.  
1  
10.9765  
180.  
4,1  
0.05  
0  
16.
```

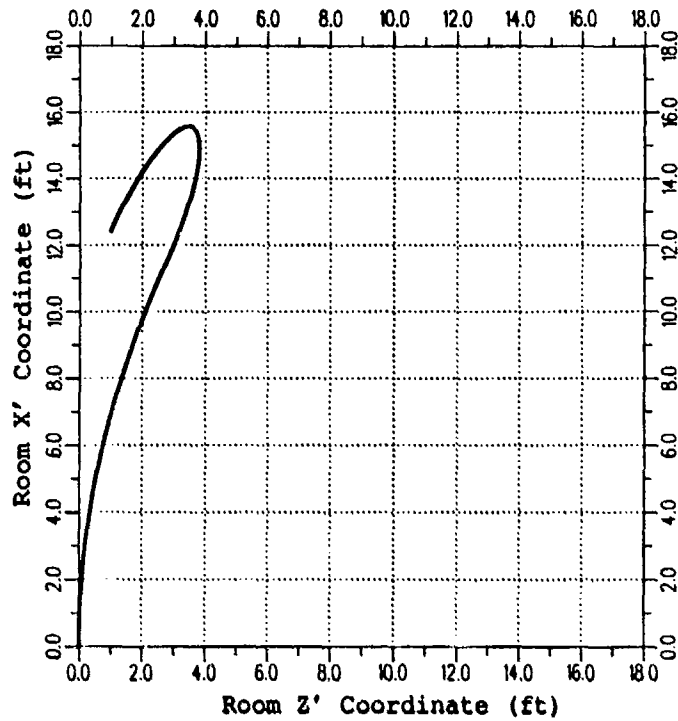


Figure 69: Range reflector cross-section ( $y' = 0$ ), skirt not shown.

179.5  
0.,0.

Figure 69 is a plot of the data in FOR017.DAT; note that this represents a parabolic reflector 11.5' high with a 4' x 1' elliptic rolled edge attached at the top.

In summary, the following steps are required to execute program CHAMBER:

1. Compilation of CHAMBER

Files required: chamber.for, ch.decl.for

(VAX) Command : fortran chamber

2. Linking of CHAMBER

Files required: chamber.obj, tipbiat.obj, ref3dt\_sub.obj, plotter.obj

(VAX) Command : link chamber, tipbist, ref3dt\_sub, plotter

### 3. Running of CHAMBER

Files required: chamber.exe, ch\_input.dat, for017.dat

(VAX) Command : run chamber

With the executable file, CHAMBER.EXE, one can begin with step 3.

Note that some options of CHAMBER automatically call PLOTTER to plot various output data. This output data is also saved in output files. One may not want CHAMBER to plot the results. Also, PLOTTER is likely to be incompatible with systems other than that which it was written on. In either case, the calls to subroutine PLOTTER can easily be removed from CHAMBER, and no results will be lost.

#### A.3 Operation of CHAMBER

In this section, the reader is brought step-by-step through a run of CHAMBER. The CH\_INPUT.DAT file that was used in this run, along with a description of each input variable, is as follows (note that all linear dimensions are in feet):

16.25	x' coordinate of tips of ceiling pyramids.
-3.5	x' coordinate of tips of floor pyramids.
20	y' coordinate of tips of side wall pyramids.
40	Maximum z' coordinate of interest in the room.
6	x' coordinate of target zone center.
24	z' coordinate of target zone center.
24.5	Pyramidal angle (alpha) - ceiling pyramids.
20.25	Number of pyramids per square foot (ceiling).
1.45	Real part of pyramid relative permittivity (ceiling).
-0.58	Imag part of pyramid relative permittivity (ceiling).
24.5	Pyramidal angle (alpha) - wall pyramids.
20.25	Number of pyramids per square foot (wall).
1.45	Real part of pyramid relative permittivity (wall).
-0.58	Imag part of pyramid relative permittivity (wall).
25.3	Pyramidal angle (alpha) - floor pyramids.

4           Number of pyramids per square foot (floor).  
 1.45       Real part of pyramid relative permittivity (floor).  
 -0.58     Imag part of pyramid relative permittivity (floor).  
 12         Focal length of reflector.  
 11.5       Radius of parabolic section of reflector.  
 1           Simulated (1) or Measured (0) Feed  
 0           Magnetic dipole, Xf direction.  
 1           Magnetic dipole, Yf direction.  
 1           Electric dipole, Xf direction.  
 0           Electric dipole, Yf direction.  
 25         Tilt angle of feed horn (above horizontal).  
 -10        Start of receive window (relative to time reference).  
 10         End of receive window (relative to time reference).

Most of these are self-explanatory, and have also been mentioned in Chapter V. Note that the reflector is specified as having a simulated feed. The following four parameters, described as magnetic and electric dipoles, are used to simulate the feed. Details on this are provided in [9]. The dipoles chosen here (0, 1, 1, 0) specify vertical polarization, while (1, 0, 0, -1) specify horizontal polarization.

The run begins with the command "run chamber". CHAMBER first reads the reflector cross-section data from FOR017.DAT, and finds the maximum  $x'$  and  $z'$  extent of the reflector. These two values are then displayed, along with resulting limitations on tip position coordinates, as follows:

Physical limits of reflector:

```

-----
Maximum x coordinate of reflector..... = 15.6 (ft)
Maximum z coordinate of reflector..... = 3.8 (ft)

Minimum allowable x coord of ceiling tips... = 15.7 (ft)
Minimum allowable y coord of side wall tips.. = 15.7 (ft)
  
```

Continue (t/f) ? T

Once this has been read, and appears correct, the user types 't' for the program to continue. CHAMBER then begins reading from file CH.INPUT.DAT. The room parameters are then displayed, along with information on the resulting ceiling, wall, and floor patches, as follows:

Room parameters:  
-----

X coordinate of tips of ceiling pyramids.... = 16.25 (ft)  
X coordinate of tips of floor pyramids..... = -3.50 (ft)  
Y coordinate of tips of side wall pyramids.. = 20.00 (ft)  
Maximum Z coordinate of interest..... = 40.00 (ft)

The patch considered along the ceiling is specified by:

Y ranging from 0.00 to 20.00 (ft)  
Z ranging from 4.00 to 40.00 (ft) and X = 16.25 (ft).

The patch considered along the wall is specified by:

X ranging from -3.50 to 16.00 (ft)  
Z ranging from 4.00 to 40.00 (ft) and Y = 20.00 (ft).

The patch considered along the floor is specified by:

Y ranging from 0.00 to 20.00 (ft)  
Z ranging from 4.00 to 40.00 (ft) and X = -3.50 (ft).

Continue (t/f) ? T

Again the user may verify the data and type 't' for CHAMBER to continue. The target zone center coordinates are then displayed:

Target Zone Center Coordinates:  
-----

x = 0.00 (ft)  
y = 0.00 (ft)  
z = 24.00 (ft)

Continue (t/f) ? T

Next, the absorber pyramid parameters are displayed:

Pyramidal absorber parameters (ceiling):  
-----

Pyramid angle (alpha)..... = 24.50 (degrees)  
Number of pyramids per sq ft..... = 20.25  
Relative permittivity of pyramid.. = 1.45 - j 0.58

Pyramidal absorber parameters (side wall):  
-----

Pyramid angle (alpha)..... = 24.50 (degrees)  
Number of pyramids per sq ft..... = 20.25  
Relative permittivity of pyramid.. = 1.45 - j 0.58

Pyramidal absorber parameters (floor):  
-----

Pyramid angle (alpha)..... = 25.30 (degrees)  
Number of pyramids per sq ft..... = 4.00  
Relative permittivity of pyramid.. = 1.45 - j 0.58

Continue (t/f) ? T

Note that pyramidal parameters may be specified separately for the ceiling, wall, and floor pyramids. The input data ends with the reflector/feed and time gate parameters, as shown below:

Reflector/Feed parameters:  
-----

Focal length of reflector..... = 12.00 (ft)  
Radius of parabolic section..... = 11.50 (ft)  
Simulated (1) or Measured (0) feed.. = 1  
Magnetic dipole (Xf)..... = 0.00  
Magnetic dipole (Yf)..... = 1.00  
Electric dipole (Xf)..... = 1.00  
Electric dipole (Yf)..... = 0.00  
Tilt angle of feed..... = 25.00 (degrees)

Time gate parameters:

-----  
Beginning of time gate.... = -10.0 (ns)  
End of time gate..... = 10.0 (ns)

Continue (t/f) ? T

Note that all of the above data has been written to an output file, CH-LOG.DAT, which serves as a log of the entire run.

CHAMBER now computes the plane wave power incident at the target zone center, which will later be used for normalization of all power computations. The round-trip time from feed to target zone center (via reflector) is also computed. As a small check, CHAMBER computes the plane wave power incident at a point 2 feet away from the target zone center, which should be close to the plane wave power at the target zone center. At this time, CHAMBER displays the following:

Computing power reference (plane wave power) and time  
reference (round trip time from feed to target zone center).

Note: Power at point 2 feet away from specified target zone center  
is down by 0.11 dB.

CHAMBER is now ready to compute the illumination of the ceiling, walls, and floor. An operating frequency has not been specified at this point, but is irrelevant since we do not consider phase. As these computations are made, the following messages are seen:

Computing illumination of ceiling...

Computing illumination of side wall...

Computing illumination of floor...

Computing input variables for all runs of subroutine BISTATIC...

The last message indicates that CHAMBER is converting the illumination data for each grid point from the room coordinate system to the pyramidal coordinate system at that grid point.

At this point, CHAMBER asks the user to specify one of three available output options, as shown below:

AVAILABLE OPTIONS:

- 1) Input:           - Frequency.  
                  - Test point in target region.  
   Output:           - Files of ceiling, wall and floor illumination.  
                  - Files of ceiling, wall and floor scattering  
                      TO the test point.  
                  - Power (totals) scattered to test point.
  
- 2) Input:           - Frequency range.  
                  - Test point in target region.  
   Output:           - Power (totals) scattered to test point  
                      versus frequency.
  
- 3) Input:           - Frequency.  
                  - Range of test points in target region.  
   Output:           - Power (totals) scattered to test point  
                      versus position.

ENTER the desired option number: 1

For purposes of illustration, option 1 has been chosen. CHAMBER then requests the user to specify the operating frequency and test point location (in the room coordinate system). These questions are shown (answered) below:

Enter the frequency of operation (GHz): 10

Enter the Test point X coordinate (ft): 6

Enter the Test point Y coordinate (ft): 0

Enter the Test point Z coordinate (ft): 24

Once the responses have been made, CHAMBER lists them and waits for verification before continuing, as shown below:

```
Frequency of operation = 10.00 (GHz)
Test point X coordinate = 6.00 (ft)
Test point Y coordinate = 0.00 (ft)
Test point Z coordinate = 24.00 (ft)
```

```
Input OK (t/f) ? T
```

Note that the following is added to CHLOG.DAT:

```
Option 1 was chosen, with these parameters:
```

```
-----
Frequency of operation = 10.00 (GHz)
Test point X coordinate = 6.00 (ft)
Test point Y coordinate = 0.00 (ft)
Test point Z coordinate = 24.00 (ft)
```

CHAMBER next computes the timing data, which determines whether each individual grid point is included in the scattered power calculations. The scattering from the appropriate grid points is then computed. As this is done, the following messages appear:

```
Computing timing data...
```

```
Computing scatter from (entire) ceiling to test point...
```

```
Computing scatter from (both) side walls to test point...
```

```
Computing scatter from (entire) floor to test point...
```

Since only option 1 provides the room illumination as output, the illumination data is now normalized:

```
Normalizing room illumination data...
```

The results of the scattered power computations are now displayed (and written to the log file). The contribution from the side walls is listed as -10,000 dB because none arrived during the specified receive window. CHAMBER also asks the user if data files of the illumination or scattering from ceiling, side wall, or floor are desired:

```
Scattered power from entire ceiling.. = -67.80 dB
Scattered power from side walls..... = -10000.00 dB
Scattered power from entire floor.... = -55.76 dB
Total scattered power..... = -55.49 dB
```

```
Enter 1 for data file of Ceiling Illumination... or
Enter 2 for data file of Ceiling Scatter..... or
Enter 3 for data file of Wall Illumination..... or
Enter 4 for data file of Wall Scatter..... or
Enter 5 for data file of Floor Illumination.... or
Enter 6 for data file of Floor Scatter..... or
Enter 7 if no data file is desired..... : 2
```

Another data file (t/f) ? F

To illustrate the format of these data files, the ceiling scatter file has been written, and the beginning of this file is shown here:

```
CEIL
SCAT
      72      40
  4.250000   39.75000
  0.250000   19.75000
 -119.8876  -119.8876
 -119.9263  -119.9263
 -120.0026  -120.0026
 -120.1156  -120.1156
 -120.2526  -120.2526
 -119.3572  -119.3572
 -119.3183  -119.3183
 -120.5702  -120.5702
 -119.9973  -119.9973
 -119.4919  -119.4919
 -119.0596  -119.0596
```

-118.6579	-118.6579
-119.9542	-119.9542
-119.8166	-119.8166
-119.6785	-119.6785
-119.5563	-119.5563
-119.4298	-119.4298
-119.3396	-119.3396
-119.2472	-119.2472
-119.1503	-119.1503
-119.0164	-119.0164
-10000.00	-10000.00
-10000.00	-10000.00
...	...

The labels CEIL and SCAT serve as identification of file type. The numbers 72 and 40 are the number of  $z'$  values and  $y'$  values considered, respectively. The next four quantities indicate that the first and last values used for  $z'$  are 4.25 and 39.75, respectively, while the first and last values used for  $y'$  are 0.25 and 19.75, respectively. The scattered power from each grid point is then written. In column 1, the scattered power from the grid point whose coordinates are specified by the first  $z'$  and  $y'$  values is first, followed by the grid point specified by the first  $z'$  value and the *second*  $y'$  value, and so on. When the last  $y'$  value is reached, the second  $z'$  value and first  $y'$  value is considered. The second column holds the scattered power contribution from the image of the corresponding grid point in the first column. In the case shown, the two columns are identical since the test point was along the room centerline. Other data files have the same format, except that illumination files will have only one column, since illumination is always symmetric. Also, for wall files, the coordinate  $y'$  is replaced by  $x'$ . These data files can be used to generate any type of plot desired. In Chapter V, a plotting program was written to generate the gray-scale plots shown there.

CHAMBER ends the run with this reminder:

YOU SHOULD PRINT THE CH\_LOG.DAT FILE !!!

Now, let us go back to the point at which the option was chosen, and select option 2. Again, CHAMBER requests user input at this point. The questions asked are shown (answered) below:

```
ENTER the desired option number: 2

Enter the starting frequency (GHz): 2
Enter the ending frequency (GHz): 18
Enter the frequency step (GHz): 1

Enter the Test point X coordinate (ft): 6
Enter the Test point Y coordinate (ft): 0
Enter the Test point Z coordinate (ft): 24
```

Once the responses have been made, CHAMBER lists them and waits for verification before continuing:

```
The start frequency..... = 2.00 (GHz)
The end frequency..... = 18.00 (GHz)
The frequency step..... = 1.00 (GHz)
The test point X coordinate.. = 6.00 (ft)
The test point Y coordinate.. = 0.00 (ft)
The test point Z coordinate.. = 24.00 (ft)

Input OK (t/f) ? T
```

Note that the following is added to CH\_LOG.DAT:

Option 2 was chosen, with these parameters:

```
-----
start frequency..... = 2.00 (GHz)
end frequency..... = 18.00 (GHz)
frequency step..... = 1.00 (GHz)
test point X coordinate.. = 6.00 (ft)
test point Y coordinate.. = 0.00 (ft)
test point Z coordinate.. = 24.00 (ft)
```

CHAMBER will first determine the frequency dependence of the absorber scatter of the ceiling, side walls, floor, and of the room as a whole. This is done through consideration of a pyramid with parameters identical to those of pyramids on the ceiling, on the wall, and on the floor. As it does so, this message is seen:

Computing frequency dependence of room scatter...

Next, CHAMBER computes the timing data (which is valid for all frequencies) and the absorber scatter at the starting frequency. As this is done, the following messages are displayed:

Computing timing data...

Computing scatter from (entire) ceiling to test point...

Computing scatter from (both) side walls to test point...

Computing scatter from (entire) floor to test point...

CHAMBER then uses the frequency dependence information to determine the absorber scatter at each frequency specified. This is much more efficient than computing the absorber scatter from every grid point at each frequency.

A plot of ceiling, wall, floor, and total absorber scatter versus frequency is now made by PLOTTER. The results are also written to an output file, OPTION.2.DAT. This file is shown here:

17				
2.000000	-41.51463	-53.82076	-10000.00	-41.77732
3.000000	-45.03645	-57.34258	-10000.00	-45.29964
4.000000	-47.53522	-59.84136	-10000.00	-47.79840
5.000000	-49.47342	-61.77956	-10000.00	-49.73661
6.000000	-51.05705	-63.36319	-10000.00	-51.32024
7.000000	-52.39597	-64.70213	-10000.00	-52.65916
8.000000	-53.65581	-65.86197	-10000.00	-53.81900
9.000000	-54.67887	-66.88503	-10000.00	-54.84206

10.00000	-55.49402	-67.80018	-10000.00	-55.75719
11.00000	-56.32187	-68.62801	-10000.00	-56.58506
12.00000	-57.07764	-69.38380	-10000.00	-57.34083
13.00000	-57.77288	-70.07903	-10000.00	-58.03607
14.00000	-58.41657	-70.72273	-10000.00	-58.67976
15.00000	-59.01585	-71.32198	-10000.00	-59.27904
16.00000	-59.57642	-71.88256	-10000.00	-59.83961
17.00000	-60.10300	-72.40914	-10000.00	-60.38618
18.00000	-60.59947	-72.90561	-10000.00	-60.86266

The first number in the file, 17, specifies the number of frequencies considered. Each row then lists frequency (GHz), total scattered power (dB), scattered power from the ceiling (dB), scattered power from the side walls (dB), and scattered power from the floor (dB). Again, a value of -10,000 dB indicates that no absorber scattered power arrived during the receive window. CHAMBER ends the run with these reminders:

The option 2 data file has been written.

YOU SHOULD PRINT THE CH\_LOG.DAT FILE !!!

Lastly, let us select option 3. Again, CHAMBER requests user input. The questions asked are shown (answered) below:

ENTER the desired option number: 3

Enter the frequency of operation (GHz): 10

Enter the test point coordinate to be varied (X=1,Y=2,Z=3): 3

Enter the starting Z value (ft): 20

Enter the ending Z value (ft): 28

Enter the step in Z (ft): 0.5

Enter the Test point X coordinate (ft): 6

Enter the Test point Y coordinate (ft): 0

Once the responses have been made, CHAMBER lists them and waits for verification before continuing:

The frequency of operation = 10.0 (GHz)

Z ranges from 20.00 to 28.00 in steps of 0.50 (ft)

X = 6.00 (ft)

Y = 0.00 (ft)

Input OK (t/f) ? T

Note that the following is added to CH\_LOG.DAT:

Option 3 was chosen, with these parameters:

-----  
The frequency of operation = 10.0 (GHz)

Z ranges from 20.00 to 28.00 in steps of 0.50 (ft)

X = 6.00 (ft)

Y = 0.00 (ft)

CHAMBER then computes the timing data and all absorber scattering for each test point location. When working with each individual test point, a message such as this is seen:

The current test point is: X = 6.00 (ft)  
Y = 0.00 (ft)  
Z = 20.00 (ft)

Computing timing data...

Computing scatter from (entire) ceiling to test point...

Computing scatter from (both) side walls to test point...

Computing scatter from (entire) floor to test point...

A plot of ceiling, wall, floor, and total absorber scatter versus test point location is now made by PLOTTER. The results are also written to an output file, OPTION\_3.DAT. This file is shown here:

```

17
20.00000 -53.85984 -66.50120 -86.54442 -54.10539
20.50000 -55.78167 -66.82880 -87.93372 -56.14011
21.00000 -55.91900 -67.16277 -90.61380 -56.25962
21.50000 -56.05049 -67.46210 -97.43762 -56.37653
22.00000 -55.87511 -67.64201 -10000.00 -56.17431
22.50000 -55.78619 -67.80883 -10000.00 -56.06770
23.00000 -55.73362 -67.92527 -10000.00 -56.00407
23.50000 -55.62059 -67.97193 -10000.00 -55.88097
24.00000 -55.49404 -67.80015 -10000.00 -55.75723
24.50000 -55.33838 -67.74698 -10000.00 -55.59525
25.00000 -55.37782 -67.80435 -10000.00 -55.63358
25.50000 -55.19563 -67.69741 -10000.00 -55.44688
26.00000 -55.08461 -67.58611 -10000.00 -55.33588
26.50000 -55.41229 -67.72816 -10000.00 -55.67487
27.00000 -56.29288 -71.97845 -10000.00 -56.41177
27.50000 -59.90308 -10000.00 -10000.00 -59.90308
28.00000 -10000.00 -10000.00 -10000.00 -10000.00

```

The first number in the file, 17, specifies the number of test point locations considered. Each row then lists the value (in feet) of the test point coordinate that was varied, total scattered power (dB), scattered power from the ceiling (dB), scattered power from the side walls (dB), and scattered power from the floor (dB). Again, a value of -10,000 dB indicates that no absorber scattered power arrived during the receive window. CHAMBER ends the run with these reminders:

```
The option 3 data file has been written.
```

```
YOU SHOULD PRINT THE CE_LOG.DAT FILE !!!
```

Before closing this section, it is noted that the views provided by the (option 1) gray-scale plots of Chapter V are depicted in Figure 70.

#### A.4 Error Messages

Program CHAMBER makes some simple checks on its input data, but does not attempt to detect all possible errors. However, with these few checks, and the

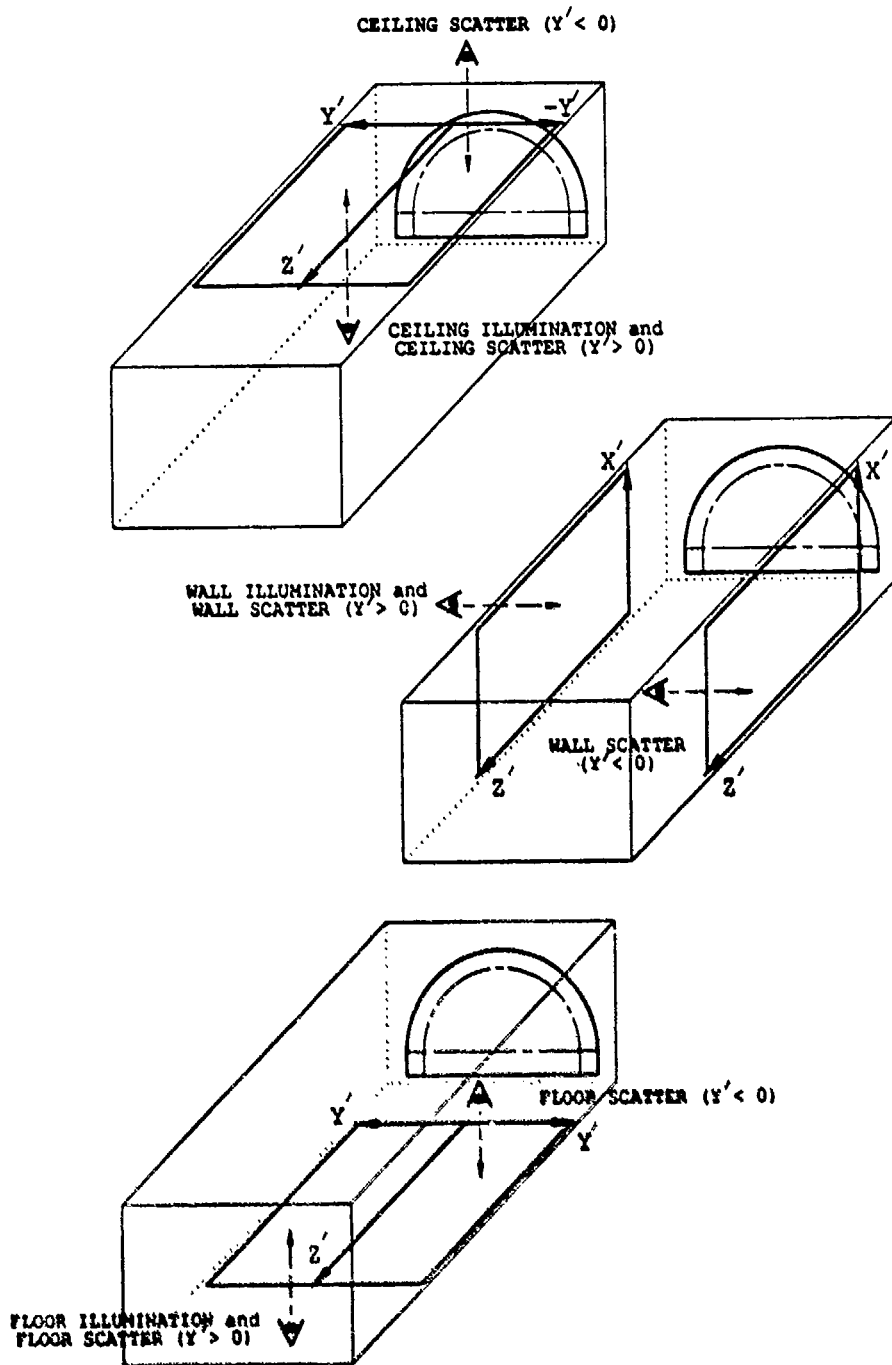


Figure 70: Views provided by gray-scale plots of Chapter V.

ample display of information provided by CHAMBER, it is unlikely that bad data would go unnoticed.

Let us now consider error messages that may occur while running program CHAMBER. If the  $x'$  coordinate of the tips of the ceiling pyramids is less than the maximum  $x'$  value of the reflector, the following error message is displayed:

X coordinate of tips of pyramids on ceiling is too small!

If the  $y'$  coordinate of the tips of the side wall pyramids is less than the maximum  $x'$  value of the reflector (which is also the maximum  $y'$  value of the reflector), then this error message is displayed:

Y coordinate of tips of pyramids on side wall is too small!

The  $x'$  coordinate of the tips of the floor pyramids should be less than zero. If this is not the case, the following error message occurs:

X coordinate of tips of floor pyramids is > than zero!

In file CH.INPUT.DAT, the user specifies the maximum  $z'$  coordinate of interest in the room, and the  $z'$  coordinate of the target zone center. Naturally, the target zone center should lie within the  $z'$  extent of the room. If not, the following error message occurs:

Maximum z coordinate of interest does not go beyond target zone center!

CHAMBER also checks that the test point is in the target region of the range; that is, that the reflection point corresponding to the test point lies along the parabolic section of the reflector. If this is not the case, the following is displayed:

Test point not in target region!!

If any of these occurs, the user will be instructed to modify the data in file CH.INPUT.DAT, or to input different data from the terminal, as appropriate.

There are other error messages which will not occur during a run of CHAMBER. However, they exist in the routines discussed, and thus are mentioned for the sake of completeness. Recall that subroutine REFL.CODE is a modified version of the reflector code in [9]. This code computed the illumination on the  $y' > 0$  side of the room only (since illumination is symmetric about the room centerline). The  $y'$  coordinate of field points must be positive. Thus, the following error message was included in the original reflector code, and carried over into subroutine REFL.CODE:

Negative value of y is not allowed.

CHAMBER will not commit this error.

To understand the next message, one must realize that the original reflector code asked the user to choose one of four types of field cuts. Program CHAMBER only requires two types of cuts. Thus, when subroutine REFL.CODE was written, it was ensured that these two field cuts would work properly. The same was not done for the other two cuts (1 and 4). However, they were not eliminated from the code, in the chance that someone may want to work with them in the future. For this reason, if these cuts are chosen, the following warning presently appears:

WARNING: Code has not been modified for IFCUT = 1,4.

Again, this will not occur while running CHAMBER.

Finally, the original reflector code displays an error message and executes a FORTRAN STOP if it comes across a field point for which it cannot find a corresponding reflection point (on the reflector). When subroutine REFL.CODE comes across a field point along some field cut for which no reflection point can be found, it will end its calculations, but will return to the main program with its partial results and with a flag set to indicate what has happened. The calling program should check this flag after each call of subroutine REFL.CODE, and take whatever action necessary. CHAMBER does check this flag, and if set will display:

No reflection point found - something is wrong!

## REFERENCES

- [1] J. B. Keller, "The Geometric Optics Theory of Diffraction," presented at the 1953 McGill Symp. Microwave Optics, A. F. Cambridge Res. Cent., Rep. TR-59-118 (II), pp. 207-210, 1959.
- [2] J. B. Keller, "A Geometrical Theory of Diffraction," in *Calculus of Variations and its Applications*, L. M. Graves, Ed. New York: McGraw-Hill, 1958, pp. 27-52.
- [3] J. B. Keller, "Geometrical Theory of Diffraction," *J. Opt. Soc. Amer.*, Vol. 52, pp. 116-130, 1962.
- [4] R. G. Kouyoumjian and P. H. Pathak, "A Uniform Geometrical Theory of Diffraction for an Edge in a Perfectly-Conducting Surface," *Proc. IEEE*, Vol 62, No 11, November 1974, pp. 1448-1461.
- [5] W. D. Burnside, N. Wang and E. L. Pelton, "Near-Field Pattern Analysis of Airborne Antennas," *IEEE Trans. on Antennas and Propagation*, Vol AP-28, No 3, pp. 318-327, 1980.
- [6] W. D. Burnside and K. W. Burgener, "High Frequency Scattering by a Thin Lossless Dielectric Slab," *IEEE Trans. on Antennas and Propagation*, Vol AP-31, No 1, pp. 104-111, 1983.
- [7] B. T. DeWitt, *Analysis and Measurement of Electromagnetic Scattering by Pyramidal and Wedge Absorber*, PhD Dissertation, The Ohio State University, 1986.
- [8] A. D. Rawlins, "Diffraction by a Dielectric Wedge," *J. Inst. Math. Appl.*, Vol 19, pp. 261-279, 1977.
- [9] I. J. Gupta and W. D. Burnside, "User Manual for Semi-Circular Compact Range Reflector Code - - Version II," Tech. Report 716148-18, The Ohio State University Electroscience Laboratory, January 1987.
- [10] F. A. Sikta, W. D. Burnside, T-T Chu, L. Peters, Jr, "First-Order Equivalent Current and Corner Diffraction Scattering from Flat Plate Structures," *IEEE Trans. on Antennas and Propagation*, Vol AP-31, No 4, pp. 584-589, 1983.
- [11] T. J. Brinkley, *Far Zone Bistatic Scattering from Flat Plates*, Master's Thesis, The Ohio State University, 1988.
- [12] J. A. Stratton, *Electromagnetic Theory*, McGraw-Hill, 1941.

The message indicates "something is wrong" since CHAMBER is specifically designed to consider only field points that *have* corresponding reflection points. This message should never appear.

One last point must be made on subroutine REFL.CODE. While the measured feed pattern option was carried over from the original reflector code, and while CHAMBER will not object to one specifying a measured feed pattern in file CH.INPUT.DAT, this option has not been exercised by the author.

- [13] W. D. Burnside, Personal communication, The Ohio State University Electroscience Laboratory.
- [14] G. Clerici and J. D. Young, "Analysis of Anechoic Room Scattering for Compact Range Performance Prediction," Tech. Report 719267-11, The Ohio State University Electroscience Laboratory, January 1988.